High precision mass-based assay to examine growth regulation of the cell cycle

by

Amneet Gulati

B.S., Rice University (2007)

Submitted to the Department of Biological Engineering in partial fulfillment of the requirements for the degree of

Doctor of Philosophy in Biological Engineering

at the

MASSACHUSETTS INSTITUTE OF TECHNOLOGY

March 2014

[JUNE 2014]

Author..... Signature redacted .....
Department of Biological Engineering
January 22, 2013

Certified by..... Signature redacted
Scott R. Manalis
Professor of Biological and Mechanical Engineering
Thesis Advisor

Accepted by..... Signature redacted
Forest M. White
Chair, Department Committee on Graduate Theses

List of Committee members in favor of thesis defense:

- Prof. Alan Grodzinsky
- Prof. Angelika Amon
- Prof. Scott Manalis

High precision mass-based assay to examine growth regulation of the cell cycle

by

Amneet Gulati

Submitted to the Department of Biological Engineering

on January 22, 2014 in partial fulfillment of the requirements

for the degree of Doctor of Philosophy in Biological Engineering

ABSTRACT

Studying biophysical properties of cells can provide insight into the metabolic mechanisms and regulation of cell cycle processes. Though size is considered to be a fundamental property of cell state, its measurement on a single-cell basis with high-resolution has been elusive primarily due to enormous experimental barriers. This thesis discusses the use of a cantilever based suspended microchannel resonator (SMR) to measure mass, and resistive pulse based Coulter counter to measure volume.

First, we discuss the implementation of several engineering principles that have enabled the SMR to measure size with a high precision and temporal resolution. As a result, growth rates can now be estimated at a single-cell basis with unprecedented precision of ~170 $fg.hr^{-1}$.

Second, we employ the SMR to investigate the coordination between the fundamental processes of cell growth and cell division cycle. Contrary to the reigning 60-yr old hypothesis of a deterministic size-control of the cell cycle, it is observed that cells display significant size variability at the Start checkpoint of the cell cycle. Furthermore, the measurements find only a weak size-control on the time spent in G1. Remarkably, it is observed that the cell's initial growth rate is a significantly better predictor of G1 duration than its initial size.

Third, we develop a method to enable continuous, long-term volume measurement. Based on a commercial Coulter counter device, it provides a complementary technique for high-throughput measurement and continuous sampling of cell volume, as well volumetric growth rate on a population-scale.

Thesis Supervisor: Scott Manalis
Title: Professor of Biological and Mechanical Engineering

Acknowledgements

I would first like to begin by thanking my graduate advisor, Scott Manalis. He has a remarkable understanding of research from a student's perspective, and has been instrumental in my development as a scientist. I found his approach to building precision engineering instruments to gain insight into fundamental biological phenomena extremely inspiring. He has a knack for identifying new applications for the unique SMR technology, and seeking out exceptional collaborators to expand into new fields of biology. I hope to be able to take what Scott has taught me about leadership, vision and communication to the next chapter in my life.

I am very grateful to have exceptional thesis committee members. Both Professors Angelika Amon and Al Grodzinsky have been powerful scientific role models for me. Angelika was also a key collaborator for my thesis project, and has been tremendously influential in delineating the framework for the biological problem that inspired the direction of my academic research. Her wealth of knowledge in the yeast biology field has greatly contributed to my academic development. Al, who since the beginning has been extremely supportive, and his valuable advice has helped shape my research.

I would like to thank my peers that I have had the privilege of working with. Alexi Goranov, from the Amon lab, has been an extremely valuable collaborator with his tremendous zeal and vast expertise in cell-cycle regulation. I have immensely enjoyed working with Manalis lab members. Will Grover, an expert microfluidicist and my office mate for a couple years, was my sounding board for raw ideas. Scott Knudsen has been a great mentor through the years, and we have become great friends along the way. Wesley Weng and Sungmin Son, who shared with me the invaluable knowledge of building a long-term cell growth measurement system. Selim Olcum and Steve Wasserman for their wealth of knowledge in electrical engineering that helped me achieve the mass precision necessary for yeast growth measurements. Nate Cermak for providing data

acquisition code and for his advice on data analysis and statistics. Andrea Bryan for her collaboration on the Coulter counter project; her attention to detail and knowledge of engineering made working with her a pleasure.

I have been very fortunate to be surrounded by great friends – Yvonne, Tiffany, Xiaosai and Karan – that have all been partners in my graduate experience here at MIT. We have spent some long nights working together on projects and problem sets, and other nights having serious fun! Finally, I would like to dedicate this thesis to my family who has been a source of constant support and encouragement. My brother, Jai has been my unconditional cheerleader, with a willing heart and listening ear. I am eternally grateful to my parents, Harmohinder and Jaspal, who sent me to the US, halfway around the earth, when I was eighteen so that I could have the best educational opportunities. This work truly would not have been possible if not for their unyielding faith and relentless support.

Table of Contents

List of Figures

List of Tables

1 Introduction

1.1 Background

1.1.1 Principles in cell growth and size homeostasis

Size is a fundamental attribute impacting cellular design, fitness and function. Size homeostasis, on average, requires doubling of cell mass with each division event. How cells convert steady increases in size into a switch-like decision to enter the mitotic cycle has been an intriguing question in biological engineering. Despite extensive study of cell proliferation in the field of oncology, little is known about how cells couple cell growth and cell division cycle. The postulated answers to it remain contentious at best, as there exist formidable experimental barriers that make studying this coupling very difficult.

Building upon the expertise that exists in our lab for real-time mass sensing, I have established a method to monitor the time-dependent changes in cell mass as a single yeast cell progresses through its cell cycle. This has allowed us insight into cellular growth and division that are distinct but coupled processes. Understanding the pathways that coordinate these two processes is essential to understanding the principles that underlie oncogenesis. In tumor cells, the coordination of cell growth and the cell division cycle frequently appears to be altered due to deregulation of pathways controlling the two processes. The far-reaching goal of this project is to deconvolve these two processes to understand the how cell proliferation is altered in cancer. Budding yeast is one of the premier model systems to study the basic principles of eukaryotic cell physiology. Cell growth and division machinery is highly conserved from yeast to humans.

Here we focus on the problem of how size homeostasis is achieved in proliferating cells, that is, the coordination of cell growth and division. This

coordination has to be an active process that integrates feedback from specific regulatory networks dedicated to converting the accrual of sufficient biomass into a stimulus for cell-cycle progression [1]. Early studies have presented a compelling case for the existence of critical size control in yeast [2-5].

Conceptually, imposing a critical size threshold is an effective and efficient way for a cell to coordinate growth and division [6]. It has been observed in many cell types that smaller cells delay cell-cycle progression until they have grown to a certain size. Conversely, size thresholds also help correct for overgrowth in the previous cell cycle by accelerating division relative to growth in the subsequent cell cycle. Oversized daughter cells often arise in proliferating populations owing to cell cycle delays (such as a checkpoint activation in the case of DNA damage, pheromonal arrests, etc.) and disproportionate segregation of mass upon cytokinesis. This especially holds true in the case of budding yeast cells that undergo asymmetrical division that yields larger mother cells and smaller daughter cells at the end of the mitotic cycle.

The coordination of the two processes of growth and division are thought to occur at Start, a short interval in late G1-phase of the cell cycle during which the yeast cell commits to division [7]. Passing Start requires that the cell first attain a critical size. This theory depends on the existence of a 'sizer' molecule(s) whose activity correlates with cell size. Nevertheless, the sizer is only one component that determines when the cell division occurs; in addition the extracellular environment influences the timing of the response to the changing activity of the sizer [8, 9].

Specifically, this size control mechanism has been observed to be dynamic in nature, such that larger-than-critical-size mother cells arrest prior to Start in response to nutrient starvation, mating pheromones or translation deficiencies. Following Start, the cell cycle progresses until the subsequent G1-phase is reached, even if cells are subjected to nutrient starvation, mating pheromones or signals that initiate meiosis [4, 10]. In addition to maintaining the average size over

generations, the size requirement at Start ensures that the cell possesses enough resources to complete the crucial processes of genome duplication and segregation.

In this thesis, I have examined the proposed models in literature that postulate the coordination of cell growth and division. High-resolution single-cell growth data will be collected using the SMR platform to assess which parameters are best predictive of the cell's decision to enter a division cycle.

1.1.2 Methods to measure cell growth

With the emergence of novel techniques that provide more precision and resolution, the interest in studying the fundamentals of cellular growth on a single-cell basis has been recently revived. Traditionally, cell growth has been studied on a population level by measuring the size distribution and doubling time of the culture that ensemble averages out individual growth rates. Single-cell studies, on the other hand, preserve the heterogeneity of the population, and yield cell-specific growth rates. Conventionally, cellular growth has been measured using various techniques that quantify the physical parameters of the cell such as length, surface area, volume, dry mass and buoyant mass.

Microscopy methods measure the surface area of cells and extrapolate to calculate volume, and phase microscopy has been employed to estimate the dry mass of the cell [11, 12]. Though tremendous efforts in image processing have enabled the study of cell size dynamics, these methods remain limited by optical resolution, prone to artifacts for non-spherical cells, and relatively low-throughput. On the other hand, Coulter counter and forward-scatter measurements offer high-throughput measurement of the volume distributions of cell populations [13, 14]. However, it is very difficult to monitor the size of a single cell as it progresses through the cell cycle using these techniques. In addition, these measurements are of often low in accuracy and are prone to osmotic swelling due to subtle changes in the ionic strength of the cell suspension. Mass measurement, on the other hand, is advantageous as it provides a measure of the biomass of the cell such as proteins, membrane lipids, nucleic acids and cytoskeletal elements.

In the most comprehensive single cell study yet to examine the interrelationship of cell growth and division, studied single yeast cells microscopically using a fluorescent reporter protein as a proxy for cell size [15]. By correlating cell size to specific cell cycle events, a size threshold for entry into the division cycle was observed. Though, protein content of a cell by account for a dominant portion of its mass, it does not guarantee a precise readout of a cell's biomass. By contrast, advanced forms of microscopy for measuring cell's dry mass have been applied to cell growth but they have generally suffered from limited precision [16].

Our lab has developed a microfluidic tool to measure the mass of single cells in real-time with unprecedented precision. Since the SMR has a volumetric capacity of ~50nL, it can handle rare and limited cell samples with relative ease compared to other flow cytometric methods that need either concentrated or large volumes of sample. The SMR is ideal in that it measures the mass of the cell directly, and the shape of the cells does not compromise the precision. Our aim is to measure biophysical growth characteristics at a single-cell level to determine the growth pattern, and understand how accumulation of biomass affects cell cycle progression in yeast.

1.2 SMR description and measurement

1.2.1 Device concept and basic operation

The suspended microchannel resonator (SMR) is a microfabricated cantilever-based mass sensor (Figure 1-1) developed in the Manalis laboratory [17, 18]. Label-free biological sensing with unprecedented mass resolution was recently enabled using the SMR [17]. The measurement principle is based on the determination of shifts in the resonant frequency of the resonating structure by the addition of a target mass. These resonators have opened up the possibility of achieving vacuum level precision for samples in the aqueous environment by

flowing samples through a hollowed cantilever beam maintained in a vacuum cavity. Such an advancement prevents significant energy losses from viscous damping, while improving the frequency resolution of the cantilever – typically indicated by its quality factor, Q. The quality factor is defined as $\omega_f/\Delta\omega$, where ω_f is the cantilever resonant frequency and $\Delta\omega$ is the bandwidth at FWHM. The SMR is capable of weighing sub-monolayers of adsorbed proteins [18], nanoparticles [19] as well as cells ranging from bacteria to yeast to mammalian cells [20] with sub-femtogram level resolution (in a 1 Hz bandwidth).

A cantilever with h height, w width and L length has a natural frequency or first mode frequency that is given by:

$$f = \frac{1}{2\pi}\sqrt{\frac{k}{m^*}} \propto \frac{h}{L^2}$$

where k is the spring constant of the cantilevered structure and m^* is the effective mass ($m^* = \frac{33}{140}m$), with m being the mass of the structure [17, 21]. The mass sensitivity for a small mass Δm is given by:

$$\frac{\Delta f}{\Delta m} = \frac{1}{2}\frac{f}{m} \propto \frac{1}{wL^3}$$

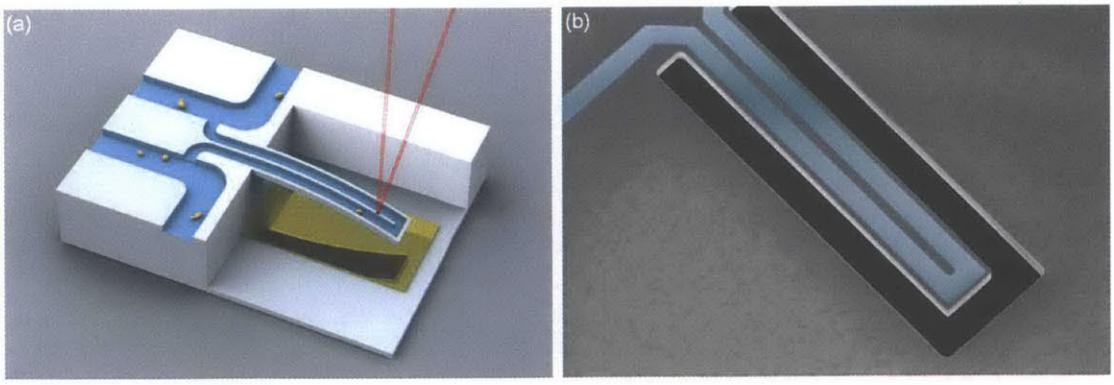

Figure 1-1: A planar view of the SMR. (a) A rendering depicting part of the suspended microchannel resonator (SMR) with its flanking bypasses. Electrostatic actuation (gold electrode) drives the cantilever, which is housed in an on-chip vacuum chamber, and its resonant frequency s measured with an optical lever using a red (632nm) laser beam (*image credit: F. Delgado*). (b) An SEM image of the buried channel of the cantilever during fabrication (*image credit: K. Payer*).

The SMRs are produced using a microfabrication process that was previously described [17]. The devices consist of buried channels in a silicon-on-insulator wafers, followed by wafer thinning and dry etching to form suspended microchannels with 2-3μm thin walls and a 15μm tall fluid layer. Nearly two hundred devices are fabricated and vacuum-packaged on a six-inch wafer, with yields exceeding 80%. A getter layer prevents slow degradation of the on-chip vacuum due to outgassing. Integrated under each cantilever is an electrostatic drive electrode, and the cantilever vibration is detected optically. There are four fluidic ports drilled on the top glass wafer to access the two bypass channels (30x70μm) on either side of the cantilever. Microfluidic access for sample delivery is achieved through a clamp that holds tubing in place with a gasket and o-rings at the interface (Figure 1-2). The cell sample is typically delivered from and drained to pressurized glass vials using computer-controlled pressure regulators. The temperature of the chip is regulated using a circulating water bath feeding into a hollowed copper piece that holds the SMR chip. Further detail on device operation is provided in Chapter 2.

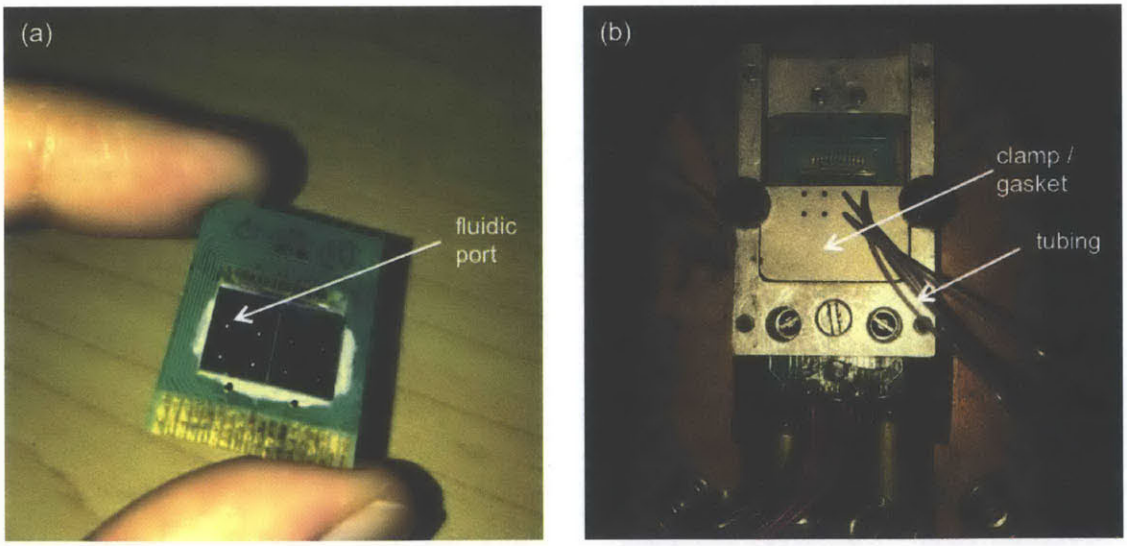

Figure 1-2: SMR interfaced with a fluidic system. (a) The SMR chip is affixed to a PCB to provide interfacing to the electrostatic drive circuit. An arrow indicates one of the eight microfluidic ports for sample delivery. (b) Tubing is interfaced with the SMR chip using a clamp and gasket. This clamp sits atop a hollowed copper piece that maintains temperature-controlled environment on-chip.

As an individual particle or cell transits the cantilever microchannel, a transient shift in the resonant frequency of the SMR is observed that corresponds to the mass change of the resonant structure. The cantilever can be operated in different vibrational modes. In the first mode, the apex of the beam offers the most sensitive measurement of the particle, while higher vibrational modes offer sensitivity various positions along the length of the cantilever (Figure 1-3). These higher modes have the advantage of making the detection insensitive to flow path, unlike in the first mode, where the frequency shift is dependent on whether the particle transits on the outer or inner edge of the cantilever. This can add a source of error to the measurement of particle mass – termed position-dependent error. To enable operation in higher modes of sensing a number of technical and engineering advances had to be made, as will be described in Section 2.3.

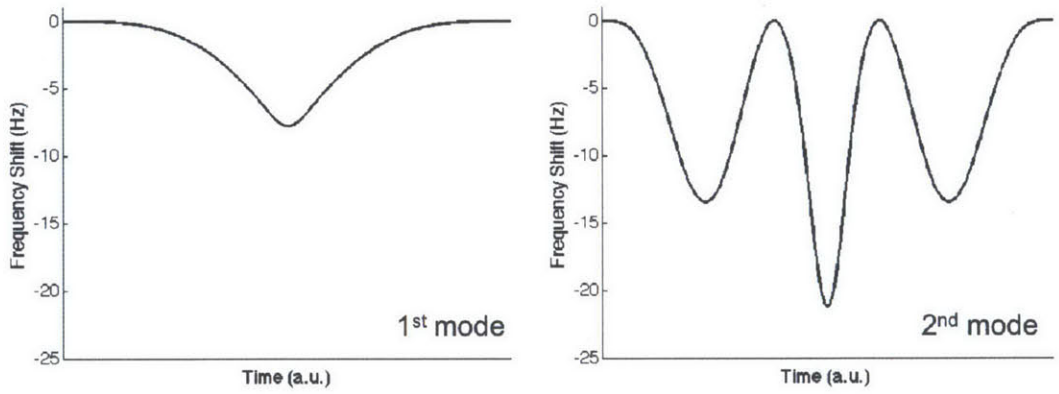

Figure 1-3: Resonant frequency shift as a function of time as a point mas transits through the SMR channel. First mode exhibits one antinode (left) and the second mode exhibits three antinodes (right).

1.2.2 Buoyant mass as a parameter to characterize cell growth

When a particle in suspension transits through the cantilever, the quantity measured by the SMR is its buoyant mass. If the particle were to have the same density as that of the surrounding fluid no additional shift in frequency would be detected. This is because buoyant mass is defined as the difference in the mass of the particle and mass of the displaced volume of fluid:

$$m_b = V_{particle}(\rho_{particle} - \rho_{fluid})$$

where $V_{particle}$ is the volume of the particle, and $\rho_{particle}$ and ρ_{fluid} are the densities of the particle and the suspension fluid, respectively (Figure 1-4).

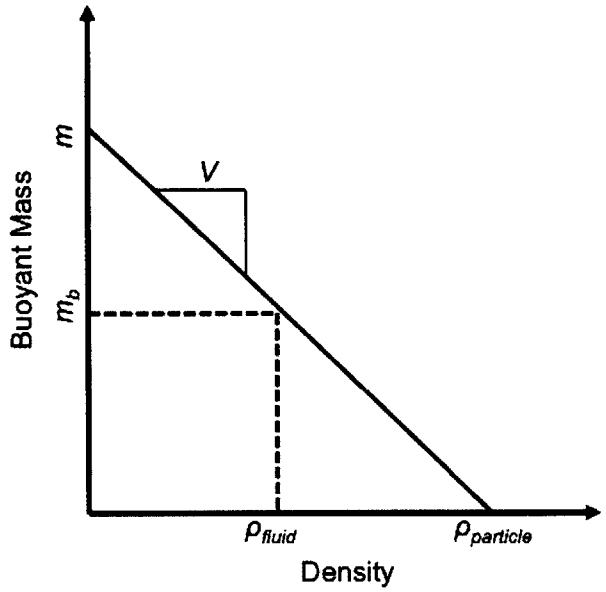

Figure 1-4: Buoyant mass (m_b) of the particle (mass, m and density, $\rho_{particle}$) as a function of the fluid density (ρ_{fluid}). The slope of the line is the volume of the particle (V).

It is important that we discuss the significance of buoyant mass with respect to biological samples, especially since we are interested in studying physical properties of single cells. Buoyant mass of a cell can be written in terms of the mass of the cell, m_{cell}, as follows:

$$m_{b,cell} = V_{cell}(\rho_{cell} - \rho_{fluid}) = m_{cell}(1 - \frac{\rho_{fluid}}{\rho_{cell}})$$

The cell is a bag of phospholipid membrane that encloses water-based organelles, proteins, nucleic acids and many other molecules that constitute its dry content (with a mass, m_{dry} and a bulk density, ρ_{dry}). Since the suspension for a cell is typically culture medium, or a buffer solution such as phosphate buffered saline (PBS), which have densities close to that of water ($\rho_{PBS} \approx 1.005$ g.cm^{-3}, $\rho_{water} \approx 1.000$ g.cm^{-3}, at room temperature), the aqueous part of the cell only contributes to ~5% of the buoyant mass. As such, the buoyant mass of the cell suspended in a

water-based solution is analogous to considering only the buoyant mass of the cell's non-aqueous content:

$$m_{b,cell} = m_{dry}(1 - \frac{\rho_{fluid}}{\rho_{dry}})$$

Therefore, buoyant mass can be taken to be a good measure for the biomass of cell, and is more directly related to anabolic processes such as protein synthesis than conventional methods that employ volume as metric.

The buoyant mass of a cell is measured by scaling the amplitude of the frequency shifts with respect to a calibration factor. The calibration factor is calculated based on the measurement of a monodisperse population of NIST size standard polystyrene beads with a known density ($\rho_{polystyrene}$ = 1.05 g.cm^{-3}). Additionally, the fact that a flowing particle causes a transient change in the resonant frequency allows for the determination of the baseline immediately prior to and after the measurement, and this differential measurement can be used to eliminate errors such as a drifting baseline often caused by temperature fluctuations.

2 Long-term measurement of single-cell yeast growth

Previously, the SMR has been demonstrated to measure buoyant mass with a precision of 0.01% [17]. By repeatedly measuring the buoyant mass of the same cell one can estimate its instantaneous growth rate. Here we describe the limitations of the current system as well as discuss the various technical advancements and engineering solutions that were implemented to enable high-precision, long-term growth measurements of single yeast cells.

2.1 Device optimization for yeast cell measurement

To accommodate yeast cells, the SMR was scaled up from cross-sectional dimensions of 3 x 8 μm^2 to 8 x 8 μm^2, and then subsequently to 15 x 20 μm^2 as is discussed in Section 2.2. Design of the device was constrained by the following considerations:

- maximizing mass sensitivity;
- minimizing detection noise;
- maximizing long-term trap stability.

Mass sensitivity of the cantilever is determined by:

$$\frac{\Delta f}{f} \approx -\frac{1}{2}\frac{\Delta m}{m}$$

where f is the resonant frequency and m is the mass of the cantilever, and Δf is the incremental frequency shift observed when an added target mass of Δm transits the apex of the cantilever. To maximize sensitivity, the mass of the cantilever needs to be minimized. Since the cross-section of the cantilever is set to accommodate yeast cells, the length is the only free parameter to optimize for. The resonant frequency gets higher as the cantilever gets shorter. However, the amplitude of the cantilever decreases proportional to length, leading to increased baseline frequency noise, as

is determined by the following relationship:

$$a_n \approx \frac{L^3 Q}{EI} f_n$$

where a_n is the amplitude of oscillation in the n^{th} vibrational mode of a cantilever of length L, quality factor Q, Young's modulus E, and second moment of inertia I that has a resonant frequency of f_n in the n^{th} vibrational mode. Based on the simulation of oscillation amplitude and the empirically determined baseline noise of existing cantilever, the length was optimized to be 204μm for 8 x 8 μm^2 devices and 320μm for 15 x 20 μm^2 devices to achieve maximal mass resolution.

2.2 Implementation of long-term dynamic trap

To measure the growth pattern of a given cell, one has to measure its mass repeatedly. In recent years, our lab introduced a snapshot mode of measuring cellular growth [20] for a variety of non-adherent cell samples that include mouse lymphocytes, yeast and bacteria. In the snapshot mode, a cell is trapped just long enough (typically a few minutes) to obtain its instantaneous growth rate. When snapshot mode is used on a population of cells, the growth rate can be measured as these cells progress through the cell cycle. This mode of trapping was not particularly stable and could not be sustained for prolonged periods to obtain long-term growth measurements on single cells.

To monitor the growth during the entirety of the cell-cycle of the budding yeast, there was a need to develop a continuous mode to measure growth rate of a cell over an extended period (of the order of a few hours), and potentially even over generations. The implementation of long-term dynamic trapping consists of a high-precision computer controlled fluidic system that is capable, through a feedback algorithm, of detecting a transient cell and subsequently reversing the fluid flow, to redirect the cell back into the cantilever. The periodic flow reversal creates a dynamic trap allowing for consecutive measurements of the buoyant mass of an individual cell. There are four major requirements to be able to

implement a long-term dynamic trap:

(i) Precise control of fluid flow;

(ii) Removal of extraneous cells to prevent trap interruption;

(iii) Replenishment of cell medium to maintain environmental equilibrium;

(iv) Reliable retrieval of the original cell

2.2.1 Precise control of fluid flow

Firstly, the current fluidic scheme for the SMR system suffered from a leakage flow, often large enough to cause the cell to drift and escape the dynamic trap. The drift against the flow direction was due to a mismatch in the fluid levels in the upstream and downstream sample vials – giving rise to a hydrostatic pressure-driven flow (Figure 2-1). To address this issue, the sample vials were mounted on a manually adjustable translation stage, and the heights of the fluid levels were closely matched until the flow in the bypass was completely stopped in the absence of externally applied pressure (further discussed in Section 2.4). This helped enhance the stability of the dynamic trap.

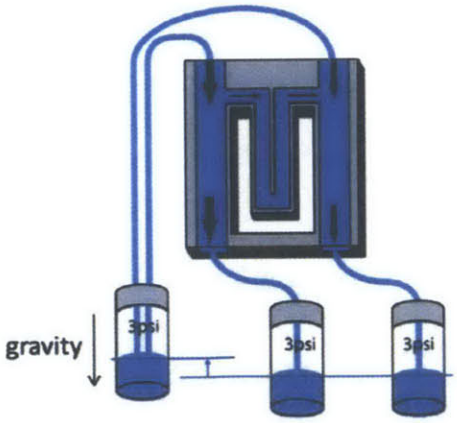

Figure 2-1: Leakage flow induced by the hydrostatic pressure (image credit: S. Son). Regardless of constant gauge pressure (3 psi) maintained on all three fluid vials, the difference in heights of the fluid across the vials induces a leakage flow in the SMR channels. Qualitatively, the nature of the flow is depicted with thick (high flow rate) and thin (low flow rate). As such, the leakage flow resulting from the mismatch of the net fluidic resistance along each of the two bypass channels and the connected tubing can be balanced.

2.2.2 Removal of extraneous cells to prevent trap interruption

Secondly, to prevent stray cells from interfering with the trap of the original cell, an innovative sample-loading scheme was implemented. The cell sample was loaded from the downstream port using a pinched-flow, such that the sample plug does not flow past the SMR device into the upstream bypass. This ensured that upon trapping when the flow direction was reversed that these extraneous cells didn't flow down into the vicinity of the SMR and interrupt the trap. Once the desired cell passed through the SMR, the rest of the sample plug was washed away while sequestering the desired cell in the opposite bypass (Figure 2-2).

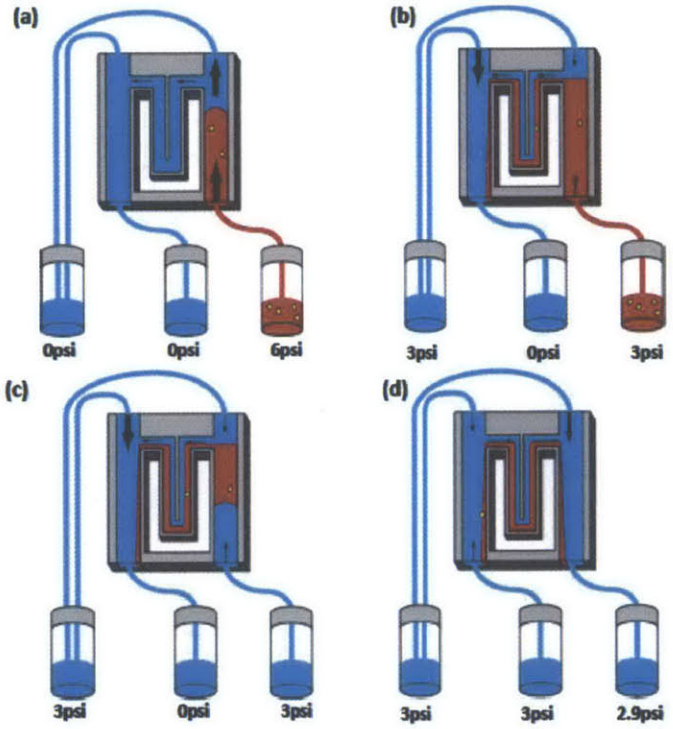

Figure 2-2: Single cell loading in the SMR for long-term growth measurement (image credit: S. Son). (A) One upstream and two downstream vials are pressurized by independent pressure regulators. The system is primed with medium (blue) before a cell is loaded. During cell loading, only the downstream vial on the right is pressurized (6 psi) and the sample plug (red) flows into the device channels. The flow rate is qualitatively indicated with thick (high) and thin (low) arrows. (B) As the sample plug moves towards the cantilever buried channel, an equal pressure (3 psi) is applied to both the upstream and downstream vials. By balancing the pressure applied across the bypass, fluid from both the upstream and downstream directions enter the SMR. As a result, the flow path of the cell is confined to either the inner or outer region of the channel, which minimizes the position dependent error. (C) After the sample has been completely loaded, all pressure

sources are turned off and the sample vial is exchanged for one containing fresh medium. The downstream vial is hten pressurized again to keep the cell in transit. (D) As soon as a cell of a desirable size transits the cantilever buried channel, the flow direction is reversed and the flow rate is reduced by setting the downstream pressure to 2.9 psi. The sample plug on the right bypass channels is rinsed away by incoming flow from upstream. The fluid level in all three vials is matched to eliminate any leakage flow.

2.2.3 Replenishment of cell medium to maintain environmental equilibrium

Thirdly, to grow the cell in the device over extended periods, one has to consider replenishing nutrients to be able to sustain steady-state growth conditions. Typically, microfluidic cell culture systems suffer from change in cell medium properties due to dehydration and acidification. This is largely attributable to the gas permeability of polydimethylsiloxane (PDMS) material that is often employed in the fabrication of these devices. The SMR, on the other hand, is not prone to such drawbacks since it is a silicon-glass device, making it impermeable to air. However, the SMR has a volumetric capacity of tens of nanoliters, and can be prone to acidification of the medium upon release of carbon dioxide during aerobic respiration. Incidentally, the flow configuration for the sample loading (described above) also ensures that medium is replenished on every passage of the cell through the SMR. The volume of the new medium introduced is dependent on how far out from the SMR the cell travels in the bypass, and the frequency of replenishment depends on how often the measurement is made and the cell transits the SMR. These two factors were optimized to minimize the shear stress on the cell (Figure 2-3).

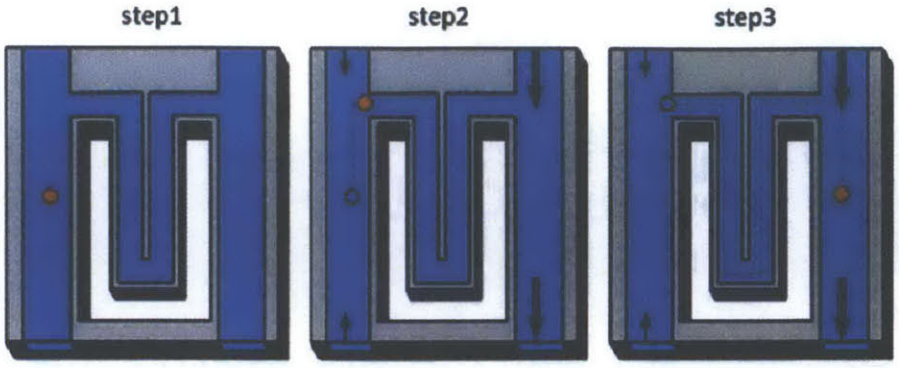

Figure 2-3: The schematic of dynamic trapping (image credit: S. Son). Depicted above is half of a full trap cycle that is composed of two reciprocal fluidic configurations. In step 1, the cell rests in the bypass channel for 5 seconds. IN step 2, the cell slowly travels towards the upstream direction at a speed of ~150μm/s. This step can take up to 2 seconds (varies based on the initial position of the cell in the bypass). Simultaneously, fresh medium is replenished in the opposite bypass channel at the flow rate of several nanoliters per second. In step 3, the cell transits through the buried channel and stops at a precisely controlled position in the bypass channel; this takes approximately 1 second.

2.2.4 Reliable retrieval of the original cell

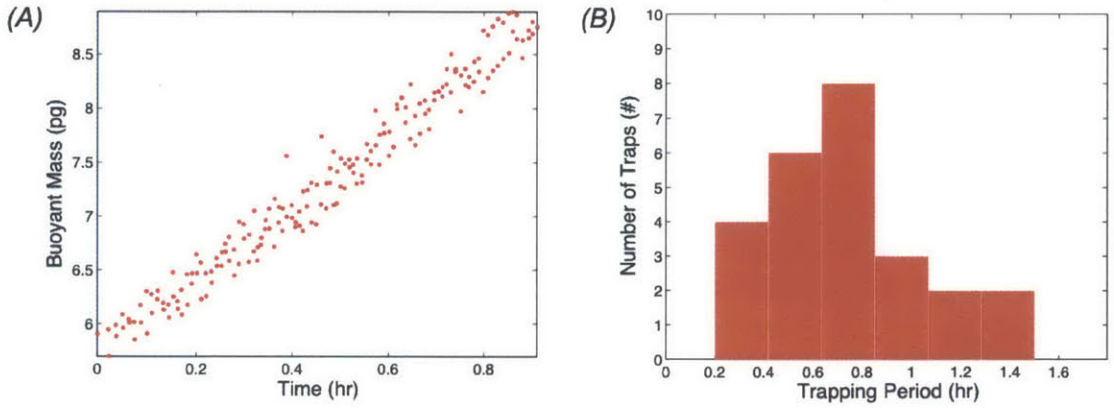

Figure 2-4: Dynamic trapping in an 8x8μm² SMR. (A) A representative mass trajectory for a haploid yeast cell at 30°C. (B) Histogram of the trapping events recorded using the 8x8μm² SMR, with an average trapping period of ~43 minutes.

The current design for the 8 x 8 μm² yeast devices only allows for shorter period traps due to instabilities in flow that are exacerbated due to the mismatch in the fluidic resistances of the cantilever channel and the sample bypass (Figure 2-4). As a comparison, the 15x20μm² mammalian device has a cross-sectional ratio of cantilever to bypass channels of 1:7, and that for a yeast device is 1:33 (Figure 2-5), as the bypass cross-sections were maintained across both these devices

(30x70μm²) while only modifying internal cantilever dimensions. This design choice was made due to the fact that the second-generation of SMR devices were designed in consideration of measuring population distributions, and not single-cell growth. As a result, for a given flow velocity in the driving bypass, the corresponding flow velocity through both the cantilever and the receiving bypass are about four times faster in the 8 x 8 μm² than for the 15 x 20 μm² device, as is demonstrated in the computational fluid dynamics (CFD) simulation (Figure 2-5). This leads to two issues: (i) the cell goes too far out into the receiving bypass and takes too long to return to allow for a reliable retrieval of the same cell; (ii) the flow through the cantilever is exceedingly fast, leading to suboptimal frequency response acquisition that leads to a much reduced mass resolution and impairs the pressure feedback required to maintain the cell in dynamic trap. Thus, the resulting dynamic trapping is unstable and prone to sporadic cell loss.

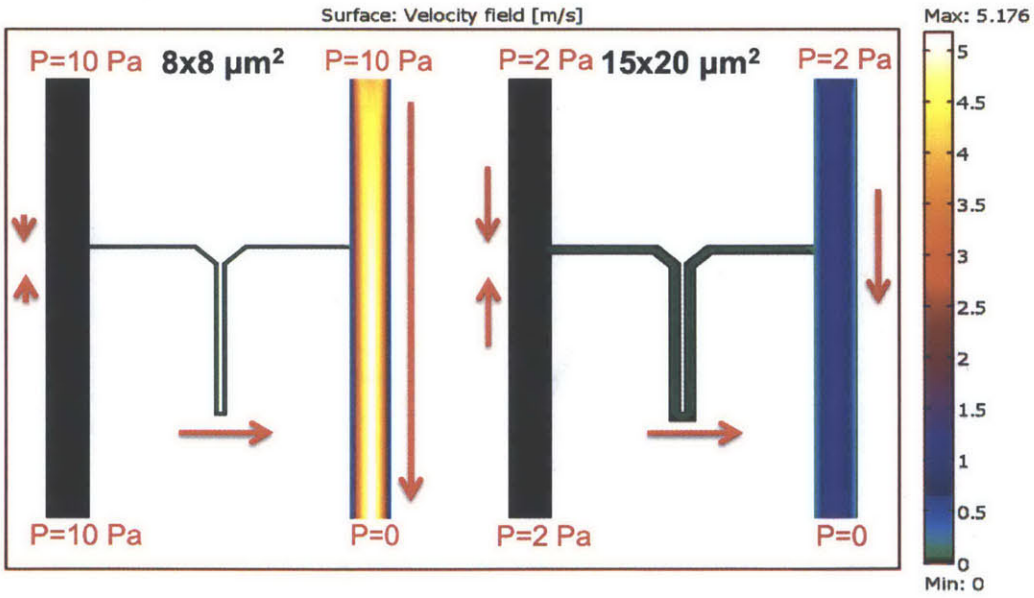

Figure 2-5: Computational fluid dynamics simulation of the 15x20 μm² and 8x8 μm² devices shows the flow velocity profile. In this simulation, the velocity in the driving bypass is set to be equal in the two devices, and the difference in the flow profiles in the cantilever and the receiving bypass for the two devices becomes apparent.

To prevent extremely fast transits, decreasing the pressure differential across the cantilever can slow down the flow in the driving bypass. However, there is a limit on how much the flow can be slowed down in the 8x8 μm^2 SMRs. Due to mismatched resistances, slow enough transit through the cantilever translates into extremely low flow rates (~3x slower than in the 15 x20 μm^2 devices) in the bypass that lead to a greater probability of the cell settling out and interacting with the floor of the bypass that often promote cell adhesion to the surface, thus hindering its retrieval for repeated measurement. Another major downside to slowing down the flow is that the resulting velocity in both bypasses is so small that excess cells that are remnants from the sample loading step do not get cleared out as quickly in the 8 x 8 μm^2 (of the order of an hour or so) as they do in 15 x 20 μm^2 (of the order of a few minutes). The consequence of this is that straggling cells are more likely to disrupt the trap to obtain prolonged growth measurements in the 8 x 8 μm^2 yeast devices.

Since the fabrication turnaround on these devices is of the order of a year, we opted to use the 15 x 20 μm^2 devices that offered extremely stable trapping conditions, and were capable of measuring growth across 100 hours (or several cell doublings). Since these devices have lower mass resolution when employed for yeast cell measurements, we chose to implement two solutions:

- Employed the use diploid yeast to explore cell growth regulation. These are nearly twice as heavy as the haploids – resulting in a ~2-fold increase in the signal-to-noise ratio;
- Operated cantilever in a higher vibrational mode – resulting in >3-fold increase in mass sensitivity (see Section 2.3).

2.3 Enhancement of measurement sensitivity with higher vibration mode

Yeast cells are significantly smaller than mammalian cells. Typical yeast cells weighs ~10pg (for a diploid), and a mammalian cell weighs ~75pg. Although the

current mass precision of the 15x20 μm^2 cantilevers is high (~200fg), the absolute mass resolution within a cell doubling is relatively low for yeast cell measurements. In addition to measuring the mass of a cell in real-time we were also interested in measuring its instantaneous growth rate. Instantaneous growth rate is essentially the time derivative of the mass curve, and consequently had higher noise than the mass measurement.

In order to derive meaningful growth rate information, smoothing the mass trajectories was necessary. However, since we were interested in calculating the growth rate of nascent cells, the first few minutes of the mass trajectory were essential, and also the most prone to edge artifacts from the smoothing filter. Since filtering was not a viable option to estimate nascent growth rates, the measurement precision needed to be increased.

Precision is defined as the mass equivalent of Allan deviation that characterizes the noise level of the system. The SMR's precision depends on a number of factors – the frequency noise, the sensitivity of the system, and position dependent noise based on particle flow path. By harnessing higher modes of sensing, one can increase the sensitivity of the cantilever, and overcome the position dependent error. The position dependent error arises from the cell transiting the cantilever following a range of possible streamlines – some closer to the inner and some to the outer wall at the tip of the cantilever. This results in a variation in frequency shift due to the difference in the distance of the particle away from the clamped end of the cantilever (Figure 2-6). When a particle transits a cantilever operating in the second vibrational mode it exhibits 3 antinodes – a global maximum in the frequency shift induced at the tip similar to the first mode, as well as two additional local maxima along the length of the cantilever. These secondary antinodes are nearly insensitive to the lateral position of the particle in the channel as seen in Figure 2-6, and therefore mass sensing in the second mode is largely limited by the system frequency resolution. Another benefit is enhanced sensitivity since for a given particle mass, both the primary antinode (~2.7 times

greater) and the secondary antinodes (~1.7 times greater) exhibit higher frequency shift than that for first mode detection.

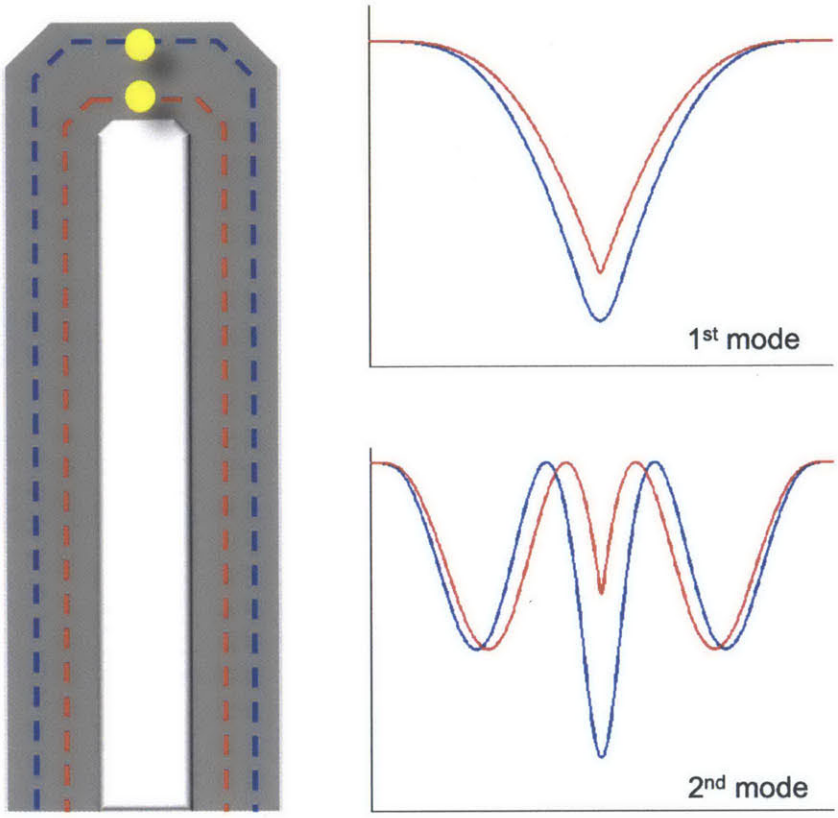

Figure 2-6: A particle in laminar flow can the transit the SMR in a streamline that lies anywhere between the inner and outer edge of the channel. The frequency shift measured is larger for a particle that travels close to the outer edge (blue line) than if the particle travels close to the inner edge (red line). The resulting frequency shift observed in first mode is sensitive to the lateral displacement along the channel resulting in position-dependent error, however the secondary antinodes in the second mode are relatively insensitive to the lateral displacement.

2.3.1 Piezoelectric Actuation

The 15x20 μm^2 devices that have relatively high stiffness (k = 348 N/m) compared to smaller bacterial SMR devices (k = 52 N/m, for a 3x8μm^2 device). Devices with low stiffness have higher Qs and signal-to-background ratios, and can be easily driven into second vibrational mode. However, the 15x20 μm^2 devices have a Q ~400 (at resonance frequency ~1.3MHz), that is about 4-fold lower than that for the first mode ~1300 (at resonance frequency ~220kHz) (Figure 2-7). It has been

previously demonstrated that these devices were not operable in the second mode using electrostatic actuation. The actuation amplitude was not high enough to generate self-sustaining oscillations in feedback at the instantaneous resonant frequency [19] , according to the Barkhausen criteria. To achieve higher actuation amplitudes and to simultaneously decrease oscillator frequency noise, we replaced the electrostatic actuation with an external piezoelectric crystal affixed under the SMR device. The frequency stability improves with increasing amplitude until Duffing type mechanical non-linearity is observed. The cantilever actuation amplitude is optimized to increase frequency stability and reduce the probability of inertial trapping of the particle at the tip (for more details see Section 2.3.3).

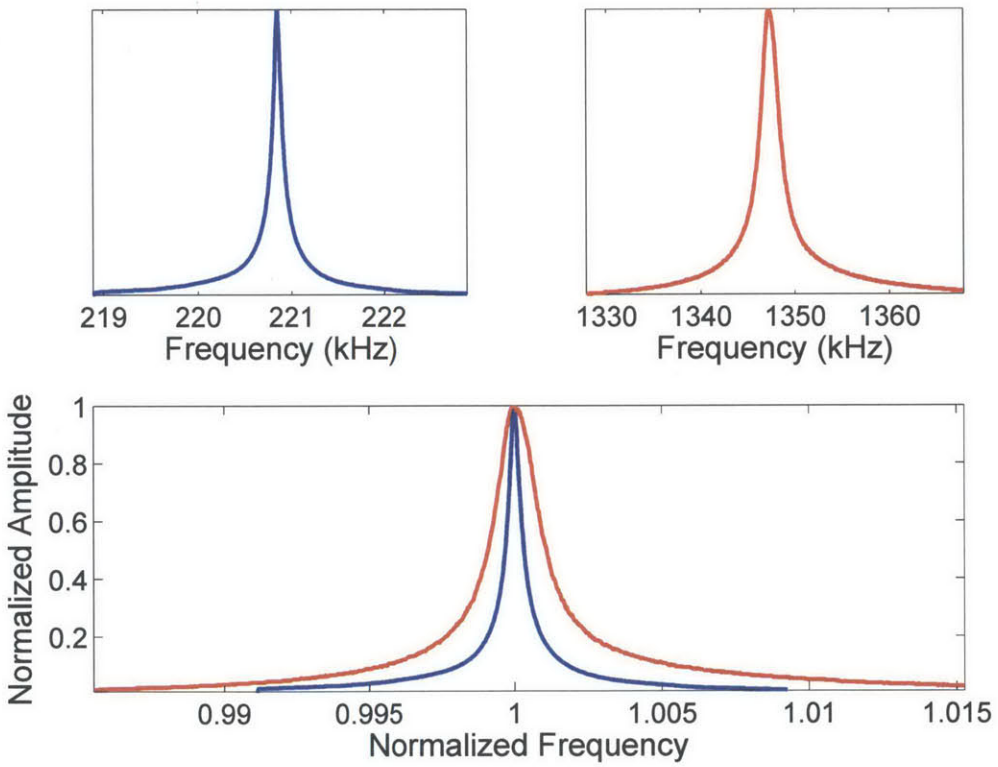

Figure 2-7: Q measurement of the 15x20um2 SMR device. (A) Measurements are made near the first vibrational mode (f1 = 220.89 kHz) in a device filled with water. (B) Measurements are made near the second vibrational mode (f2 = 1347.85 kHz). (C) Comparison of the Q-factor in the first two vibrational modes - 1st mode in blue (Q~400), and 2nd mode in red (Q ~1300). The Q curve in the 2nd mode widens due to the increased stiffness of the cantilever in higher modes.

2.3.2 Device operation

The SMR device is operated in a positive feedback loop. The cantilever motion is detected using an optical lever (Figure 2-8), phase-shifted using a user adjustable delay on a field programmable gate array (FPGA), amplified and then fed to a high-current amplifier driving the piezoelectric crystal. The frequency of oscillation of the cantilever is measured by the FPGA by digitally mixing down the cantilever deflection signal to a 1kHz, and period counting using a 100MHz clock [22].

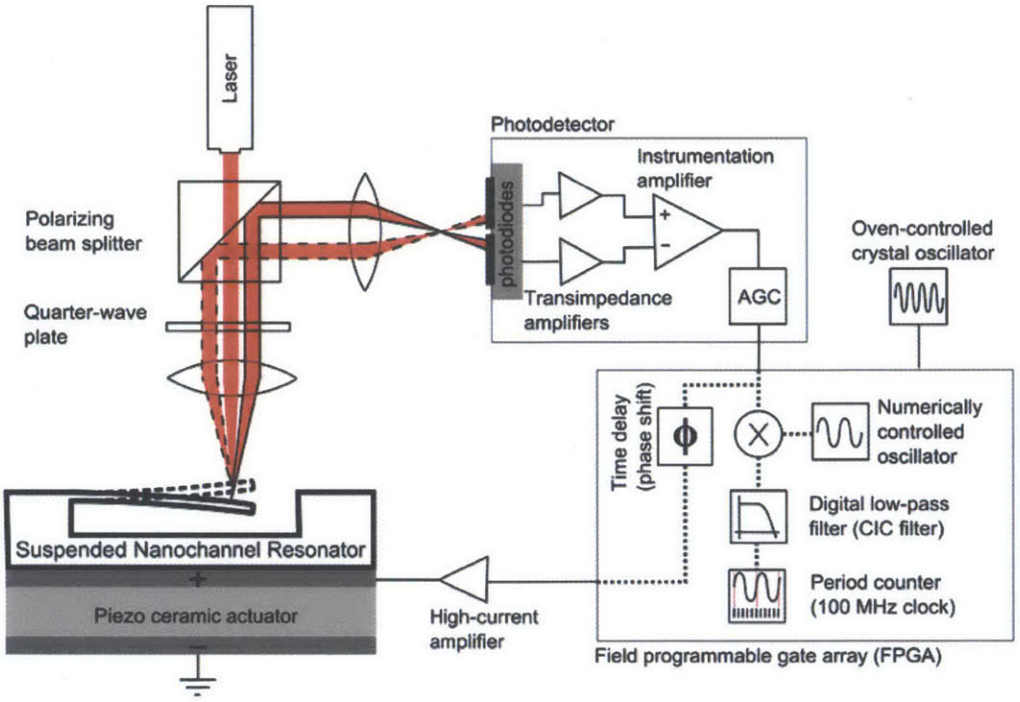

Figure 2-8: Schematic of the SMR oscillator system. The SMR measurement system consists of an optical lever to detect the cantilever position, a photodetector to convert the position to a voltage, an FPGA to phase-shift the photodetector signal and simultaneously measure the frequency, and a high-current amplifier to drive the piezo crystal actuator underneath the SMR.

2.3.3 Noise characterization

To estimate the stability of the system due to noise processes, the Allan deviation was calculated (Figure 2-9). First, we measured to see if the noise was limited by thermomechanical fluctuations of the cantilever, using the network analyzer. However, the noise spectrum did not exhibit the enhancement of any particular frequency – likely due to the high stiffness of the cantilever. Instead, we hypothesize that the frequency noise of our system is dominated by the Johnson noise of the detector that is much larger than the thermomechanical noise of a stiff cantilever. We see in Figure 2-9 that the optimal gate time lies around 10-100ms. The smoothing filter for data processing was conservatively chosen with respect to this gate time to be a 3rd order Savitsky-Golay with 15 points (3dB cutoff ~140 Hz).

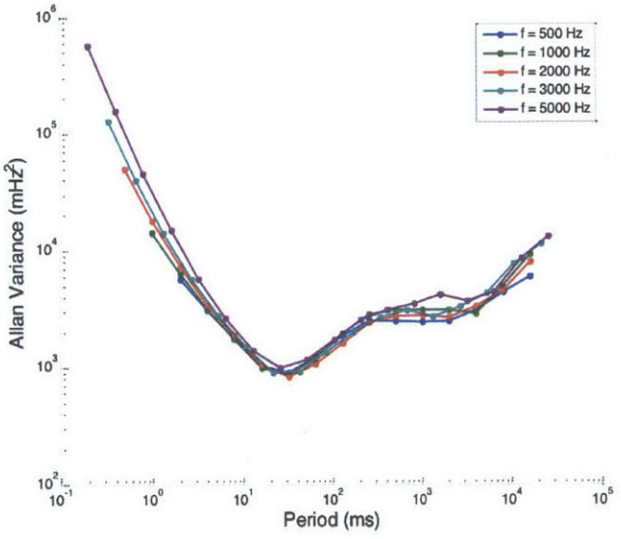

Figure 2-9: Frequency noise, quantified by the Allan variance. The noise spectrum is measured at different acquisition frequencies, as indicated by the legend. Noise is observed to be minimal around ~30ms gate time.

There is also a positive correlation between the acquisition and RMS frequency noise as is seen in (Figure 2-10A), and thus the acquisition rate for our system was set at 1000 kHz. Additionally, the frequency RMS noise rapidly decreases with increasing actuation amplitude as seen in (Figure 2-10B); however there is a tradeoff to be considered here. As the actuation amplitude of the crystal increases the inertial force exerted on the transiting particle, causing it to get

sequestered at the apex of the cantilever, unless the fluid convection rate is fast enough. Thus, there is a tradeoff between achieving low frequency noise, and preventing the particle from getting inertially sequestered.

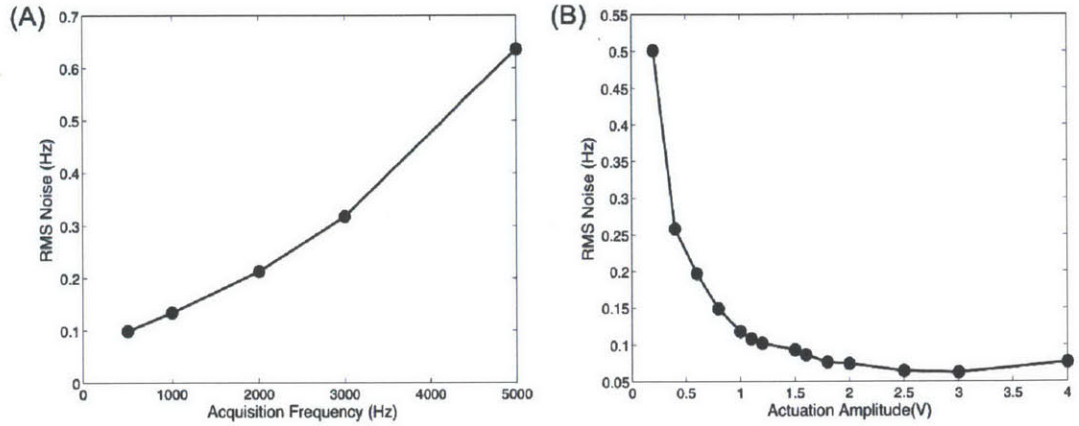

Figure 2-10: RMS frequency noise measurement. (A) RMS noise as a function of piezo crystal's actuation amplitude, with the acquisition frequency set at 1kHz. (B) RMS noise as a function of acquisition frequency with the actuation amplitude set to 1V.

To optimize these parameters, a fixed yeast cell (of buoyant mass in the 4th quartile) was dynamically trapped in the SMR, and the actuation amplitude was varied (Figure 2-11). For a given actuation amplitude, the minimum flow rate that prevents inertial sequestration was maintained. For higher actuation amplitudes faster flow rates are favorable, with the caveat that for a given acquisition frequency, there need to be an adequate number of data points in the frequency response to perform robust peak fitting for the estimation of the buoyant mass of the particle.

The precision of the system was estimated using a dynamically trapped NIST standard polystyrene bead, both in the first mode and the second mode. The precision of the second mode is four times higher than the first mode – 1st mode precision is ~200fg, and 2nd mode precision is ~45fg (Figure 2-12). Similarly, the sensitivity of the system is calculated by measuring the calibration factor from a mass distribution of a population of NIST standard polystyrene particles with a known density. It is seen that the 2nd mode sensitivity is about three times higher – 1st mode sensitivity is 0.6Hz/pg, whereas the 2nd mode's is 2Hz/pg.

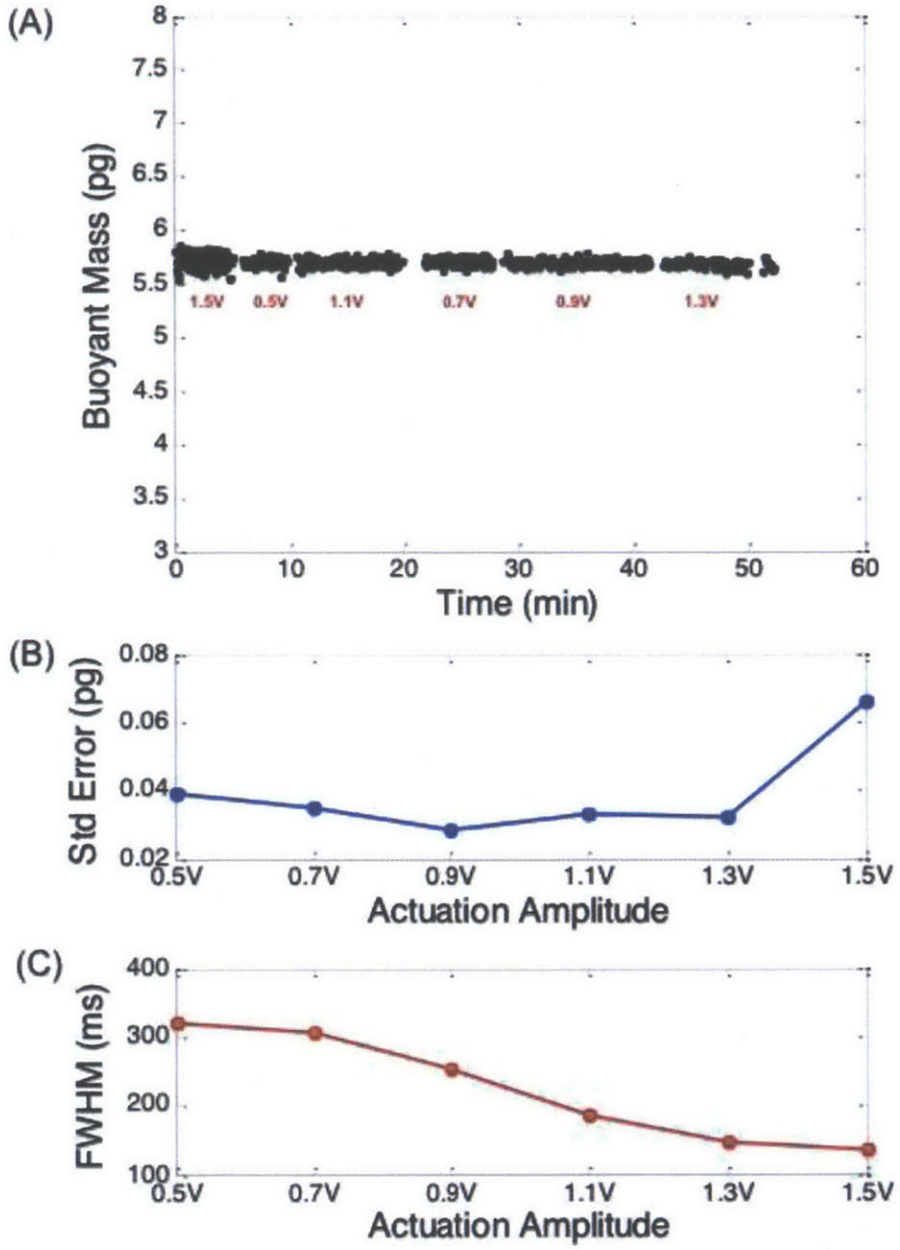

Figure 2-11: Optimization of actuation amplitude, flow rates and measurement noise. (A) A fixed cell was dynamically trapped and the actuation amplitude of the piezo crystal was varied; concurrently the pressure differential applied across the cantilever was set such that the flow rate was just enough to overcome the inertial trapping forces at the tip. (B) Observed relationship of measurement error – standard deviation of the mass of the fixed cell. (C) Observed relationship of the requisite flow rate, and consequently the FWHM of the frequency shift observed when the particle transits the cantilever.

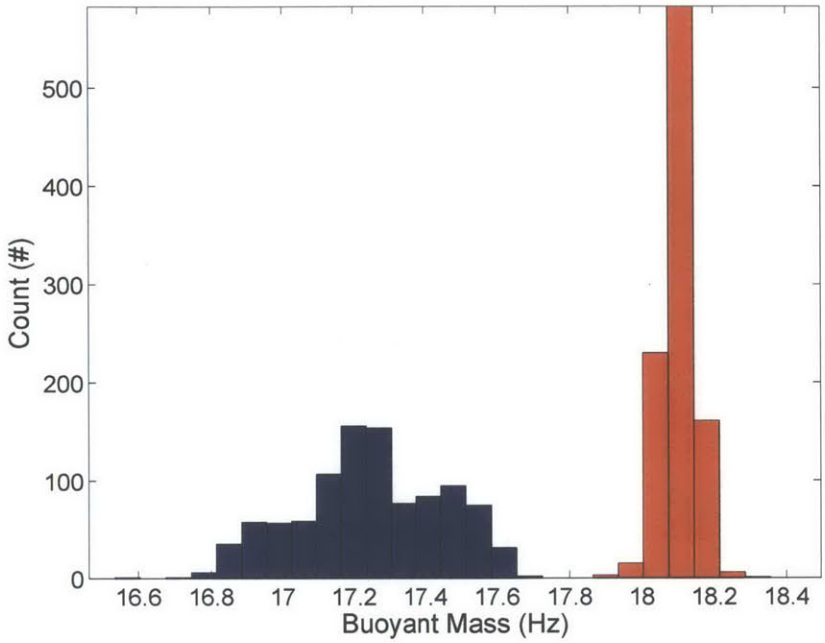

Figure 2-12: Measurement of a single polystyrene bead dynamically trapped and its buoyant mass measured in the 1st mode (blue) and 2nd mode (red). The precision of the system in each mode is estimated by the standard deviations of the distributions – 201.2 fg (N = 1000) and 44.7 fg (N = 1000), respectively for the 1st and 2nd mode. The shape of the 1st mode measurement histogram does not follow a normal distribution due to the technique of hydrodynamic focusing that allows for greater precision.

To measure the effect of improved device sensitivity and reduced frequency noise, the mass trajectory of a newly born diploid yeast cell was measured in the 2nd mode SMR system (Figure 2-13). An improvement of nearly 4-fold was observed in RMS frequency noise over the previous 1st mode system.

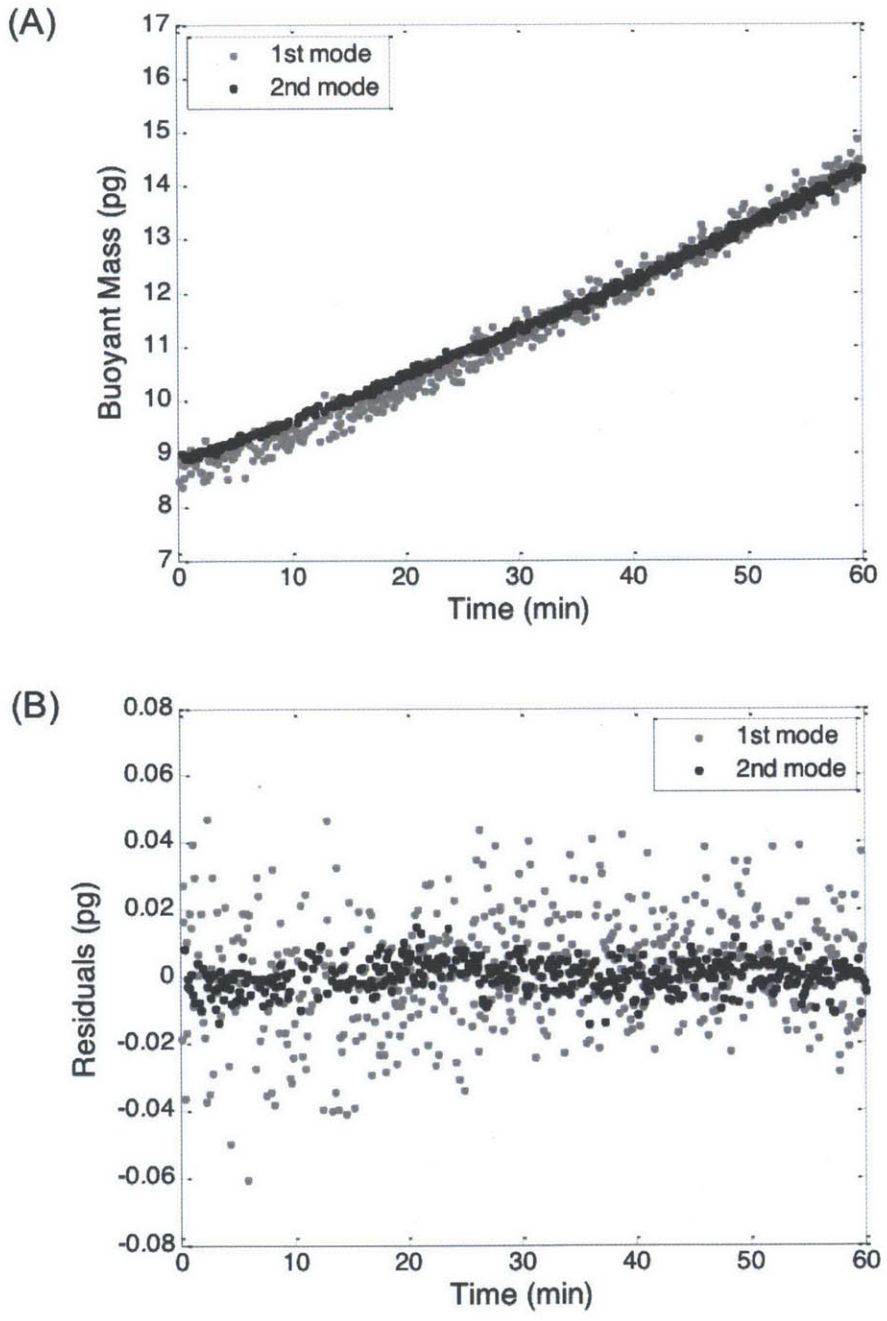

Figure 2-13: Improvement in measurement noise to measure single-cell mass trajectories. (A) Dynmically trapped measurement of a diploid yeast cell at 30oC in 1st mode (grey) and 2nd mode (black). (B) The residuals resulting from an exponential fit of these trajectories are shown. The standard deviation of the residuals resulting from a 2nd mode measurement (4.5 fg) is three times smaller than that resulting from a 1st mode measurement (17.2 fg).

2.4 Integration of Imaging

To approximate the cell cycle phase of a cell under dynamic trap, we need to optically monitor it to mark events such as budding and cytokinesis. For this purpose, it is necessary that imaging be integrated into the dynamic trapping scheme. In order to obtain high-resolution images, an upright modular Nikon microscope with a 20x objective lens (Nikon-CFI LU Plan ELWD N.A. 0.40, WD 13 mm) was integrated into the SMR system (Figure 2-14).

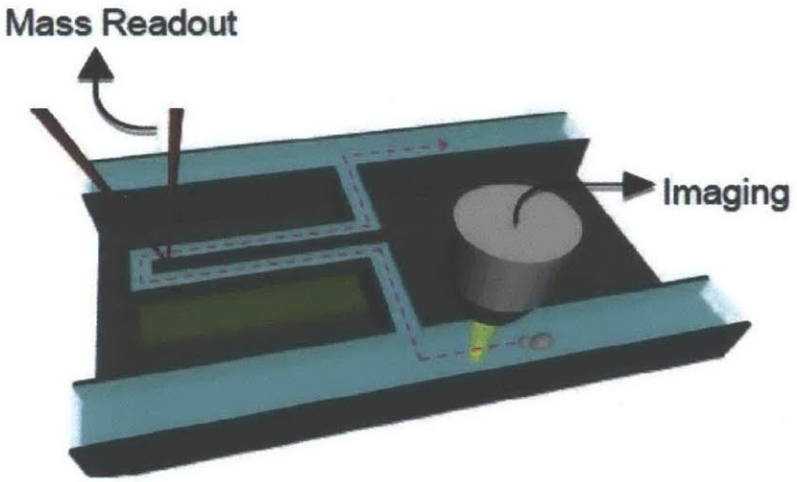

Figure 2-14: Integrated SMR system for single-cell growth studies. Schematic shows the simultaneous buoyant mass measurement and bright-field imaging of a single cell as it progresses through its cell cycle. Pressure-driven flow repeatedly shuttles the cell to cantilever and back to the bypass, where it is bathed in fresh medium and imaged to determine cell cycle stage. The dotted pink line shows the flow path a cell takes from one bypass channel through the cantilever to the opposite bypass, upon which the direction of flow is reversed and it traverses back through the cantilever. Every time a cell transits the cantilever, a transient downward shift in frequency of the SMR is observed, the minimum of which yields the cell's buoyant mass. This is repeated for an extended period of time to monitor single cell growth.

However, it was not sufficient to image the cell in flow especially since we are interested in observing the emergence of a diminutive bud at the beginning of S-phase. We have, therefore, implemented a stopped-flow condition for a fraction of the time the cell is in dynamic trap. This is achieved by hydrodynamic focusing, as discussed below. In addition, imaging the cell requires that we bring the cell out into the bypass during dynamic trapping, since the cantilever is not optically transparent.

Hydrodynamic focusing the cell into the cantilever involves achieving perfectly pinched-flow at the T-junction of the bypass and the buried channel. This can be realized by delicately balancing the flows at both the upstream and downstream ends of the driving bypass, such that the volumetric ratio of the flow entering the cantilever from the two ends is 1:1 (Figure 2-15). Despite the fact that the pressure differential applied at the upstream and downstream ports of the driving bypass is the same, the flows are not necessarily balanced. This is because there are differences in the resistances of both the channels and the tubing connecting the sample vials to the respective ports (often due to the difference in lengths and rarely because of minor occlusions from cell debris). These small yet significant differences in flow velocities can be balanced by taking advantage of the gravitationally driven component of the flow that is dependent on the difference in the height of the fluid column at the respective ports and the plane of the chip. The relationship of these variables to the effective flow-rate is described by the following equation: $Q = \frac{\Delta P + \rho g h}{R_{channel} + R_{tubing}}$. By finely adjusting the heights of the vials feeding the ports, one can implement perfectly pinched-flow.

2.5 Overcoming cellular adhesion and aggregation

In addition to the problem of yeast cells settling out of flow in low velocity fields and sticking to the surface of the channel as discussed previously, another challenge that yeast pose is the incomplete detachment of the mother and daughter cells post-cytokinesis. Therefore, at the end of the cell cycle the daughter remains adhered to the mother, and while the mother and daughter undergo consecutive budding events leading to the measurement of a cluster of cells rather an individual cell of interest. Additionally, this can lead to ambiguity of the growth rate measurement in early G1 and end of M phase in the cell cycle.

Cell adhesion can cause flow occlusions in microfluidic channels that comparable to the size of the cell, prevent recovery of the cell of interest and disrupt the dynamic trapping scheme. To reduce cell adhesion, PLL-g-PEG polymer

was used for surface passivation. PEG polymer chains are known to prevent surface biofouling and significantly reduce the non-specific interaction of cell-surface proteins; poly-L-lysine (PLL) electrostatically binds to glass, and helps tether the PLL-g-PEG molecule onto the channel surfaces. This helped considerably reduce, though not completely eliminate, the issues of cells sticking to the channels. Following PEG passivation, when the microchannels are incubated overnight with sterile cell culture medium to further block surfaces, it completely prevents cell adhesion.

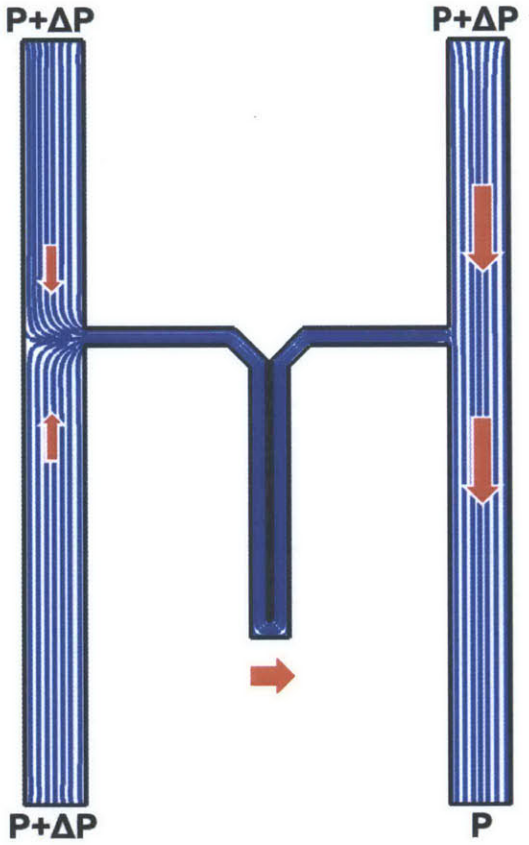

Figure 2-15: Schemicatic showing 1:1 pinched flow in the driving bypass (left). Streamlines are shown in blue, the red arrows qualitiatvely indicate flow rates.

Typically yeast form flocs during continued growth in log-phase culture. Since, cell aggregates are too large in size to enter the channel, they initially posed a problem in sample loading. To overcome this issue, an aliquot of flask-grown culture was ultrasonicated at low power, before loading the sample SMR. Ultrasonication resulted in singly suspended cells that allowed for the capture and measurement of

single cells, including newborns that we were especially interested in studying for the elucidation of size regulation in the G1-phase.

2.6 Contributions

Gulati, Amneet designed, conceived and built the system. Olcum, Selim and Cermak, Nathan assisted in development of 2nd mode actuation and detection. Son, Sungmin assisted in development of fluidic configuration for trapping. Manalis, Scott contributed materials, reagents and analysis tools.

3 Growth regulation of G1 in budding yeast

3.1 Cell growth principles

Determining cell fate is essential to understanding the molecular mechanisms that are responsible for various physiological cell phenotypes observed such as proliferation, differentiation, secretion and apoptosis among others. Although much is known about the cell cycle events that control proliferation, the processes that coordinate cell growth (as defined by increase in biomass) with cell cycle events and cell size homeostasis remain poorly understood. This is in part due to the obscurity of size metrics that cells use for gating cell cycle progression and maintaining size homeostasis, and in part due to the lack of techniques for measuring various size metrics with sufficient precision. For almost four decades, the deterministic critical size (or 'sizer') hypothesis has been widely used to explain how size homeostasis is maintained in yeast and other cell types despite variation in birth sizes [2-4, 10, 23-25]. The sizer hypothesis posits that in order to reach a critical size before they enter the cell cycle, smaller newborns spend longer in the growth (G1) phase than larger ones [4, 26, 27]. Under ideal deterministic size control, size increase during G1 could be perfectly predicted from newborn cell size.

However, the sizer model is unable to account for the large variation observed in G1 duration. A seminal single-cell study in *S. cerevisiae* by Cross and colleagues showed that the deterministic size control could account for less than one third of the variation observed in the mass accumulated during G1 [15]. We used a high precision, single cell mass sensor known as the suspended microchannel resonator (SMR) to determine: (i) whether a significant improvement in the precision of size measurements would reduce size-independent noise, such that birth size would be able to account for more variation in G1 duration; and (ii) whether cells directly

monitor their size or instead regulate G1 duration based on the rate at which newborn cells accumulate biomass.

3.2 Measurement of single-cell trajectories of nascent cells

The SMR is a micromechanical device that can measure the buoyant mass of cells in medium. Suspended cells pass through a microfluidic channel embedded inside a cantilever. A cell that is denser than the medium causes an increase in the total mass of the cantilever by an amount equal to the cell's buoyant mass. The mass increase causes the cantilever's resonant frequency to drop [17, 20]. To measure growth, the SMR in concert with a fluidic control system periodically reverses the flow direction. Cells can be repeatedly passed through the sensor, providing a direct measure of growth [28].

Newly born cells were selected from an asynchronous culture passing through the SMR. Each cell transiting the SMR with a mass below a threshold value triggered a reversal in the direction of fluid flow, confining the selected cell in the vicinity of the mass sensor. The cell's mass at capture is a close approximation of the newborn mass (Figure 3-1). After capturing a cell, a fluid control system periodically alternated the direction of flow to cause the cell to pass through the cantilever at 10 sec intervals. Between measurements, the cell rested in an adjacent bypass channel. The bypass channel was replenished with fresh medium after each transit to ensure that constant nutrient conditions were maintained. The process continued through the G1/S transition, providing a growth trajectory for the cell. To detect the emergence of a bud as a marker for the G1/S transition, a bright-field microscope integrated with the SMR imaged the cell in the bypass channel. Representative mass and image data is shown in Figure 3-2.

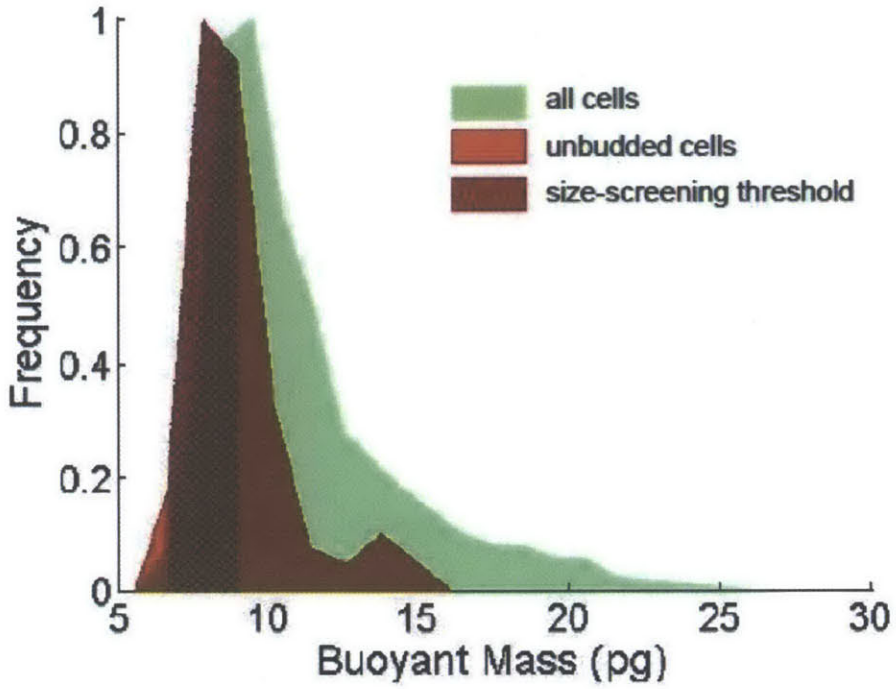

Figure 3-1: Distribution of cells captured by size-screening based on buoyant mass. The green curve represents the distribution of all cells in the population (N = 1666); the red curve represents unbudded cells (N = 106); and the black crosshatch region represents the cutoff for unbudded cells captured as a result of size-screening for newborns.

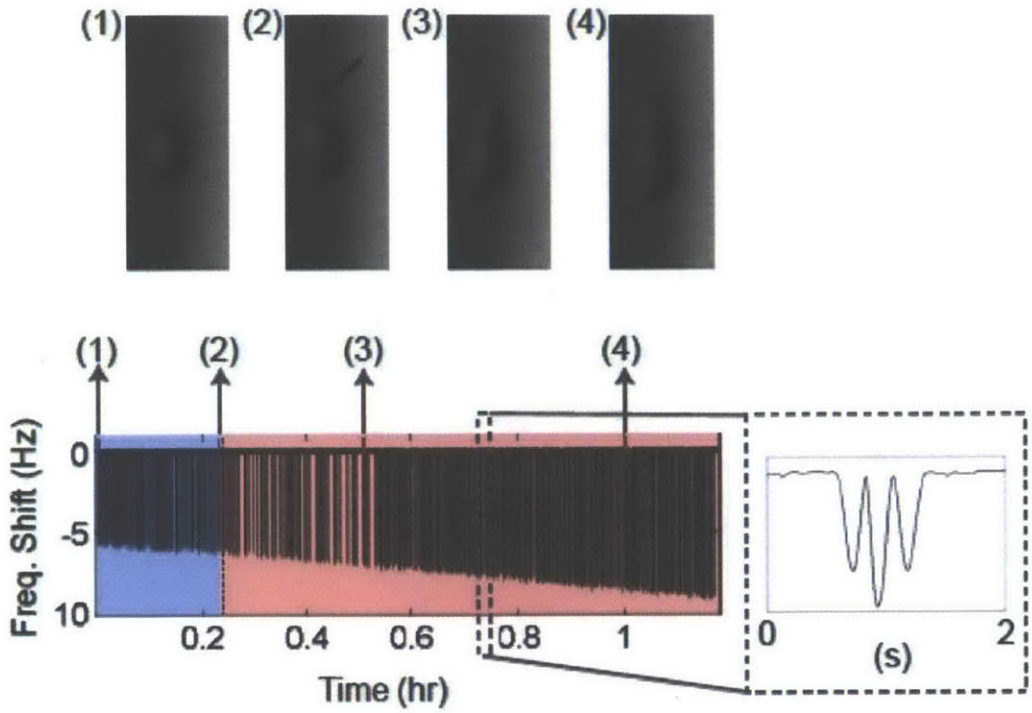

Figure 3-2: Analyzing brightfield images (scale bar: 10μm) acquired every 2s reveals the time of budding that is also annotated (black dotted line) on the real-time mass trajectory. Blue represents the unbudded stage of the cell (G1); red represents the budded phase. Frequency readout (in black) of the resonance of the SMR as the cell grows. Buoyant mass of the cell is proportional to the frequency shift, and is measured every 10s. The dashed gray box (on right) shows an enlarged view of the mass measurement recorded in a representative 2s period of the measurement of a single cell. The frequency response to a cell transiting the cantilever operated in the second vibrational mode results in three peaks, and the outer two are used to estimate the buoyant mass of the cell as described in Lee et al. [19].

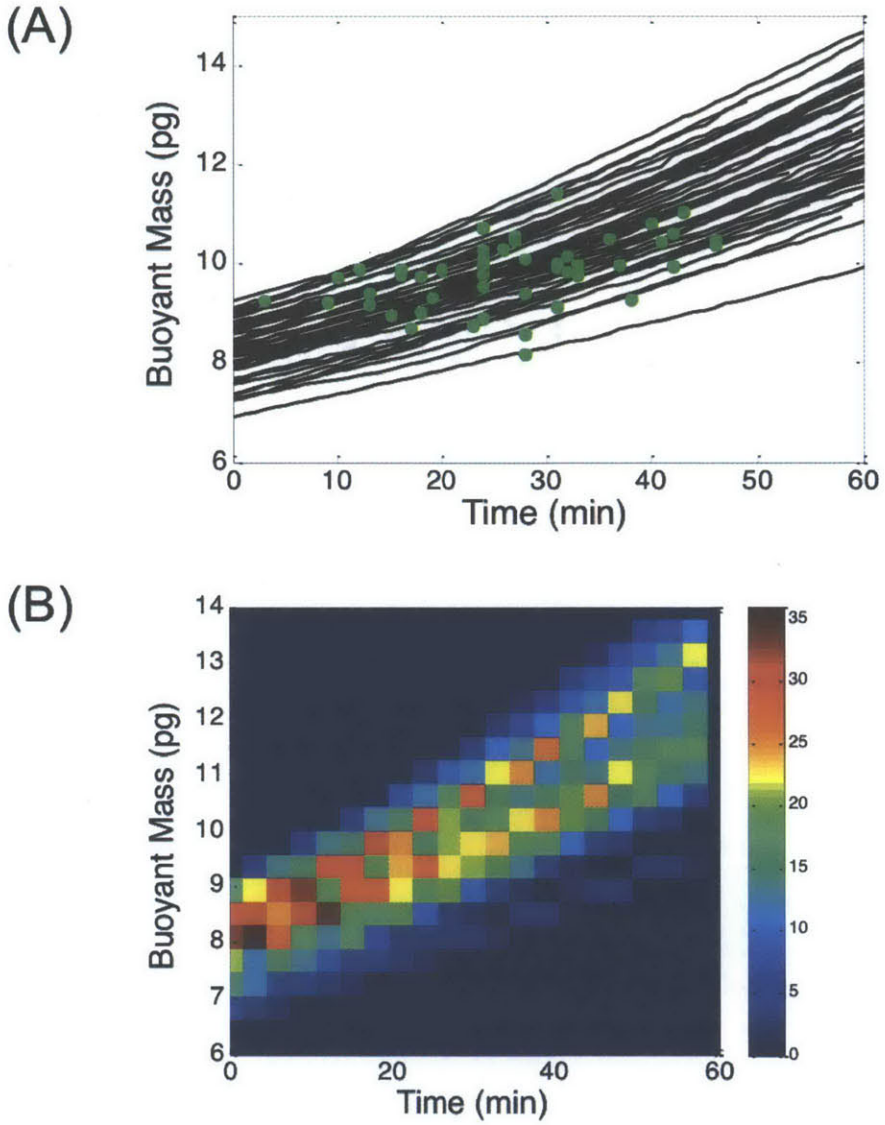

Figure 3-3: Single-cell growth measured by the SMR. (A) Mass accumulation trajectories (black lines) annotated with their respective times of bud emergence (green circles) for 50 individual cells. Budding is monitored by simultaneous bright-field microscopy. (B) Heatmap representation of buoyant mass as a function of time. The colorbar represents frequency of the population of cells traversing the mass-time matrix.

Using this technique, approximately 3-4 trajectories could be measured per day. 50 single cell trajectories were measured for this study as shown in Figure 3-3. Buoyant mass measurements were averaged over a three-minute time window, and the corresponding root-mean-square (RMS) instrument error is determined to be 16 fg of buoyant mass, or about 1.5% of the average cell size at budding. The corresponding error in growth rate measurement is 0.18 pg/hr, which is less than 4% of the average growth rate at budding (Figure 3-4).

Since we are interested in studying G1 regulation, it is necessary to follow a given cell's growth trajectory from birth to division. Commonly employed techniques to acquire newborn cells include chemical (e.g. inhibition of DNA synthesis, Mg exhaustion), biochemical (e.g. pheromone arrests, cdc mutants) or physical (e.g. elutriation fractionation, chemostatic growth) synchronization. Albeit, cells treated by these methods are largely prone to biological perturbations, such as being oversized or quiescent upon release from synchrony, and undergo reacclimatization from the induced stress of the method. As such cell's growth characteristics can potentially be masked by artifacts and can cause the very processes of interest - cell division and cell growth - to be uncoupled. The SMR size screening approach is equivalent to a synchronized culture by elutriation, but with two significant advantages. Centrifugal separation requires culturing cells in a carbon-poor medium and maintaining cultures on ice prior to and during processing. These factors typically lead to much longer doubling times than asynchronous cultures [29]. Using SMR size screening, cells remain in normal culture conditions throughout. The doubling time of the cells grown in the microfluidic channels of the SMR

There are various models proposed in literature to elucidate eukaryotic cell growth and its regulation at the G1/S transition [23, 30]. These models can be fit to the cell growth data obtained as described above, to uncover biologically relevant mechanisms that coordinate cell growth and cell division cycle. The following are some of the commonly proposed mathematical models in literature that the SMR data was queried against:

(A)

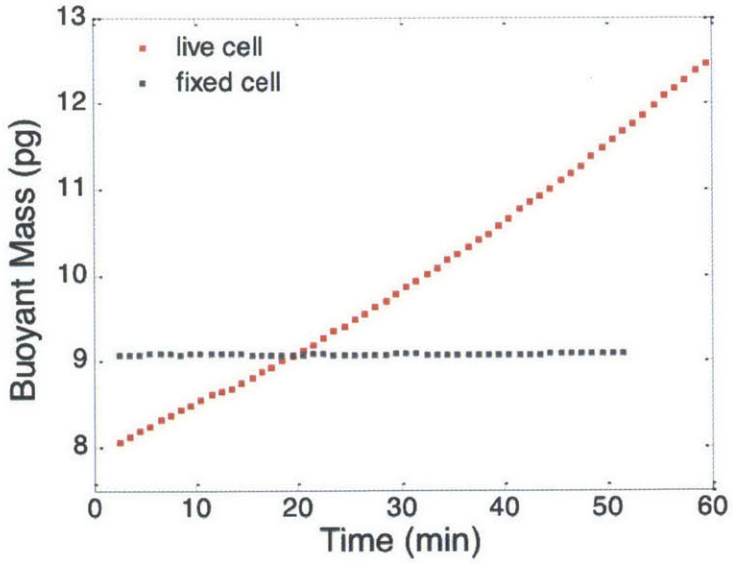

(B)

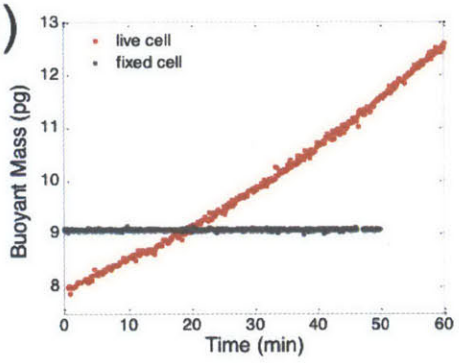

(C)

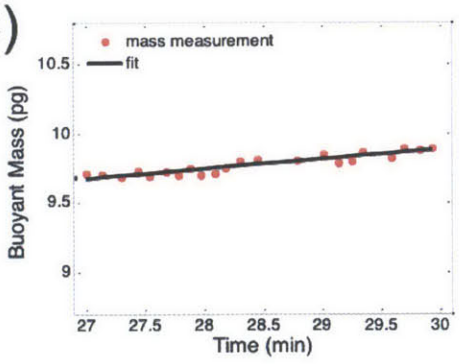

(D)

Size Metrics	Standard Error	% Error
Mass	15 fg	<1.5%
Growth Rate	0.17 pg/hr	<6%

Figure 3-4: Measurement error analysis. (A) Live cell's mass accumulation trajectory is shown in red. Fixed (4% paraformaldehyde) cell measurement is shown in gray. Data is smoothed using a boxcar filter with a 3-min span. (B) Raw data from the measurement of both the live and fixed cell is shown. (C) To extract size metrics, piece-wise linear fits are performed on 3-min sliding window of raw data in (B), with one minute intervals (e.g. 0-3min, 1-4min, 2-5min…). The fit mean yields instantaneous mass and its slope yields the instantaneous growth rate. (D) Quantification of errors in the measurement based on fixed cell control (N = 45).

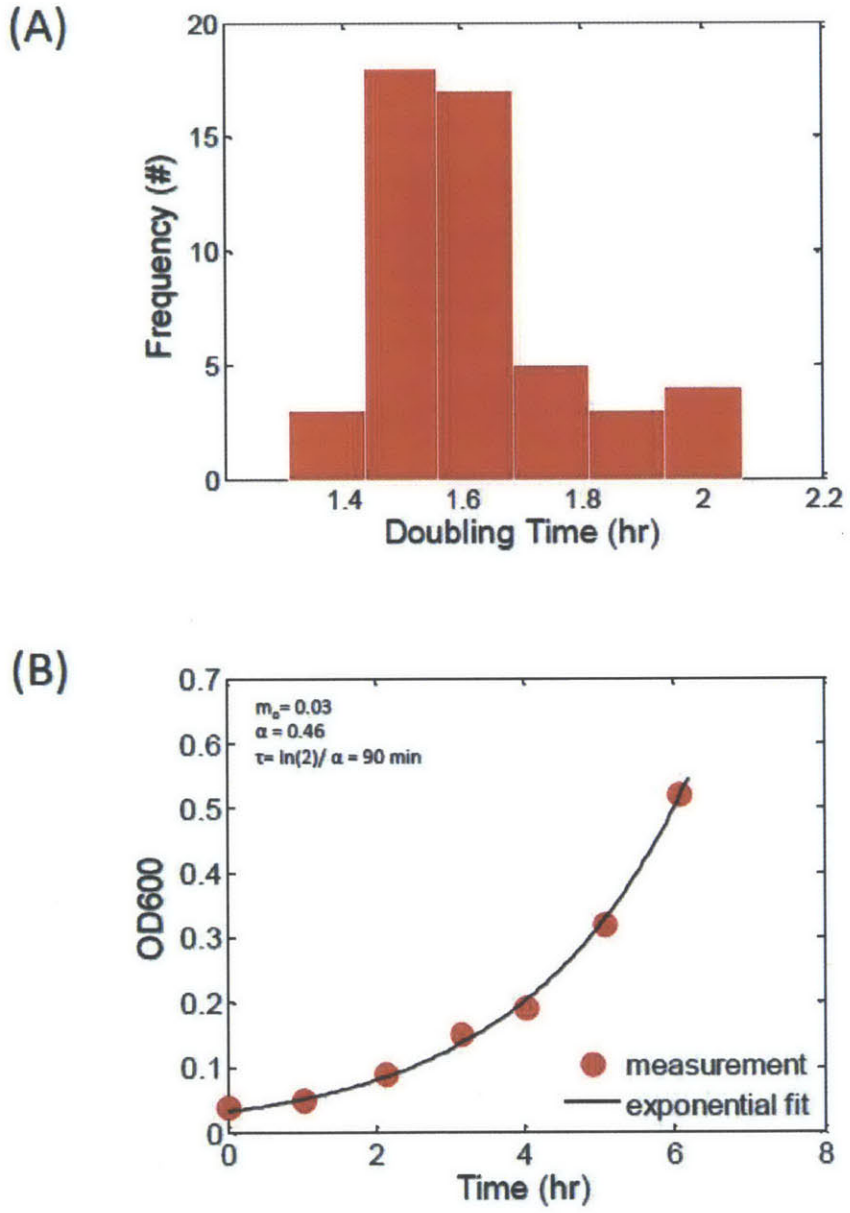

Figure 3-5: Comparison of doubling time for cells grown in bulk culture with those grown in the SMR. (A) Growth of the bulk culture as measured by the optical density at 600nm. The growth follows an exponential trend with a doubling time of 1.5 hr (fit: m_o = .003; α = 0.46). (B) Distribution of doubling rates of single cells grown in the SMR (N = 50, Mean = 1.6 hr).

(i) The cell growth is linear i.e., smaller cells will grow proportionately more than large cells over a cell cycle. This model does not require strict mechanisms that couple growth and division, and attributes cellular concentration of growth factors as limiting rather than the biosynthetic capacity of the cell [31, 32].

(ii) The cell growth is exponential, i.e., growth rate is proportional to cell size. This model requires mechanisms that correct for cell size; otherwise cell size would become heritable. In addition, it provides for the dependence of growth on ribosomal biogenesis [1, 31, 33, 34].

(iii) The cell growth is bilinear, i.e. the cells accumulate mass with a certain rate in G1, and then increases its rate of accumulation post the budding event [13, 35, 36]. This is an intermediate model between a linear and exponential model and does not necessitate a size control in G1.

With the unprecedented high precision and high-temporal resolution growth data accessible with the SMR long-term single cell measurements, we wanted to discern the difference between the linear, bilinear and exponential models of growth. Over the two-fold size range that most proliferating cells exhibit, linear and exponential curves differ only by at most 6% [37].

Upon performing a detailed curve fitting analysis on these high-precision growth trajectories we learned that the exponential model and bilinear models performed similarly well – 54% of the trajectories most favored a simple exponential model and 46% most favored a bilinear model. Our findings are in agreement with Cross and colleagues' that also observed that the bilinear and exponential models performed similarly well {Di Talia, 2007 #187}. An instance of curve fitting is shown in Figure 3-6. However, when the residuals from the exponential fit and bilinear fits were examined, systematic deviations were revealed (Appendix). Adding a constant offset to the simple exponential model served to remove any systematic deviations and the resulting residuals exhibited a normal distribution. It was found that 90% of the trajectories favored with exponential offset model over both simple exponential and bilinear. The resulting BIC from the exponential offset was on average significantly

lower than the BICs resulting from simple exponential ($\Delta BIC = 177$) and bilinear models ($\Delta BIC = 60$).

Growth trajectory pattern for a single diploid *S. cerevisiae* cell (Figure 3-7), G1 time (Figure 3-8), and doubling time (Figure 3-5A) agreed with measurements made by Di Talia et al using time-lapse microscopy and a fluorescent reporter of protein content as a proxy for cell mass [15, 38]. As seen in Figure 3-9, the mean deviation of the mass trajectory from the simple exponential model measured by the SMR was <0.3% (average absolute deviation from the exponential fit with respect to newborn size). The deviation was about 20 times lower than the time-lapse fluorescence microscopy technique (<6%, [15]), and about 44 times lower than microscopic measurements of cell surface area or volume [39].

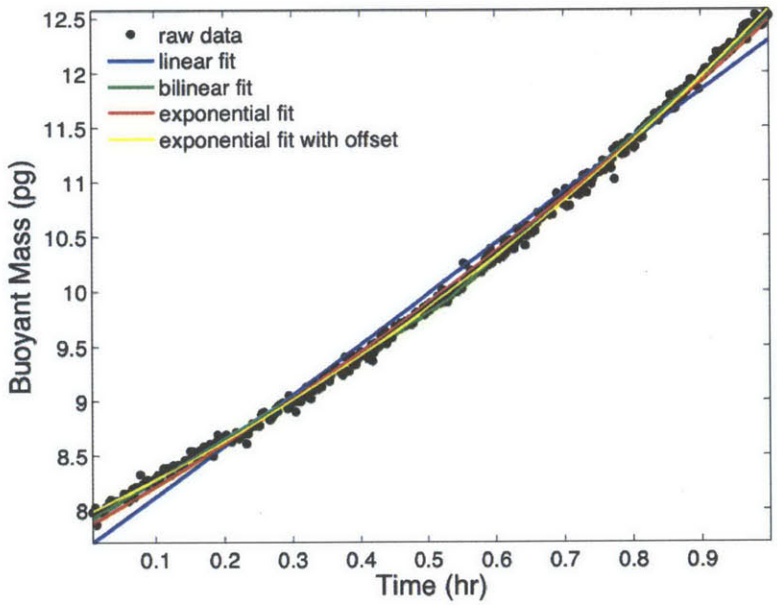

Figure 3-7: Fit analysis on single-cell mass trajectory. Raw data of mass accumulation with respect to time of a single diploid *S. cerevisiae* cell (acquired with sampling frequency of ~10s) is fit to various models; three of the best models are shown in the figure above: linear, bilinear, simple exponential and exponential with an offset. To determine the goodness of fit, Bayesian information criteria (BIC) and $\chi^2$is calculated as shown in Table 3-1.

3.3 Growth parameters predict the regulation of G1 time

For exponential growth, the critical size hypothesis suggests that fractional growth during G1 depends on newborn cell size. Fractional growth in G1 is equal to the ratio of size at budding to size at birth:

$M(t) = M_{birth} \cdot e^{\alpha t}$

At the G1/S transition, $t = T_{G1}$ and $M(t) = M_{bud}$. Therefore,

$M_{bud} = M_{birth} \cdot e^{\alpha T_{G1}}$

$\ln\left(\frac{M_{bud}}{M_{birth}}\right) = \alpha T_{G1}$, or $\quad ln(M_{bud}) - ln(M_{birth}) = \alpha T_{G1}$.

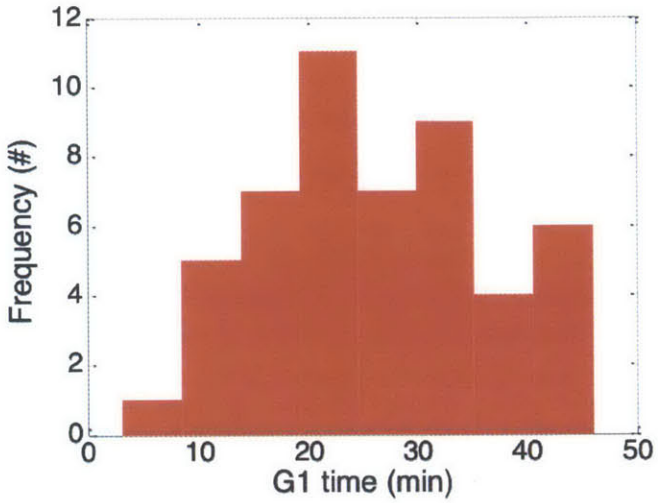

Figure 3-8: G1 times estimated from the emergence of budding. Histogram of G1 duration (Mean = 26.5 min, C.V. = 0.38).

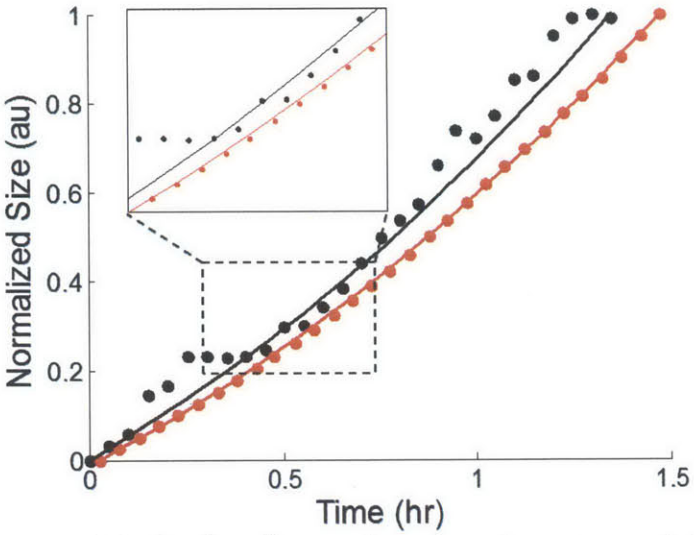

Figure 3-9: Single-cell growth trajectories measured by the SMR. In red, a growth trajectory measured with the SMR. In black, an instance of a growth trajectory measured with fluorescence microscopy (quantifying total GFP protein content); data reprinted from Di Talia S, Nature, 2007. The SMR system yields <0.3% deviation from an exponential fit (average absolute deviation from the exponential fit with respect to newborn size), versus <6% deviation for that of the fluorescence-based system [15]. Since the fluorescence data is collected with a 3-min sampling frequency, the SMR data (collected with 10s sampling frequency) is averaged and downsampled to match this sampling frequency.

A plot of fractional growth versus newborn size for a population of ideal sizers would have a slope of -1. This is because the mass of small newborn cells must increase by a proportionally greater fraction than the mass of larger newborns in order to reach the posited critical size threshold. At the other extreme, the plot would have a slope of 0 for ideal timers, in which G1 size increase depends on time alone [25, 40]. Measurement of 50 cells gave a slope of -0.59 ± 0.13, p = 1.5e-5 (Figure 3-10), implying that G1 growth follows neither of the ideal models. This finding is in agreement with the imperfect size control observed by Di Talia et al. [15]. As expected, smaller newborns tended to spend longer in G1 than larger ones (Figure 3-11A). The strength of the correlation as given by the coefficient of determination (R^2) is 0.35 ± 0.11, which implies that the birth size only accounts for about 35% of the variability observed in G1 size increase. This is also consistent with the findings of Di Talia et al. that newborn cell size contributed to 30–40% of overall G1 variability [15]. Although mass measurement with the SMR is 20 times more precise than the microscopy system used by Di Talia et al., the ability to

predict G1 duration from newborn cell size is not improved. This suggests that the variation in G1 time is attributable to intrinsic biological variation rather than noise in cell size measurement.

Because neither the newborn size nor the fractional mass increase in G1 correlate strongly with G1 duration, we investigated whether newborn growth rate is a significant predictor. Newborn growth rate is difficult to measure by microscopy since measurements generally must be separated by a few minutes to limit phototoxicity [41]. The SMR weighs cells every 10 seconds from the time a cell is captured, which facilitates precise measurement of the instantaneous growth rate. Piecewise linear fits of mass versus time (Figure 3-11B) demonstrate a negative correlation between G1 duration and the newborn growth rate. Newborn growth rate was calculated over a 3-minute window immediately following cell capture. The correlation strength was considerably higher than newborn size or fractional mass increase (R^2=0.60 ± 0.08). The covariance between newborn growth rate and newborn mass was weak (σ = 0.13), with a similarly weak correlation (slope = 0.40 ± 0.18, p = 0.032, R^2 = 0.09) as shown in Figure 3-12. Multiple linear regression with both newborn mass and newborn growth rate explained 74% of the variation in G1 duration (Figure 3-13).

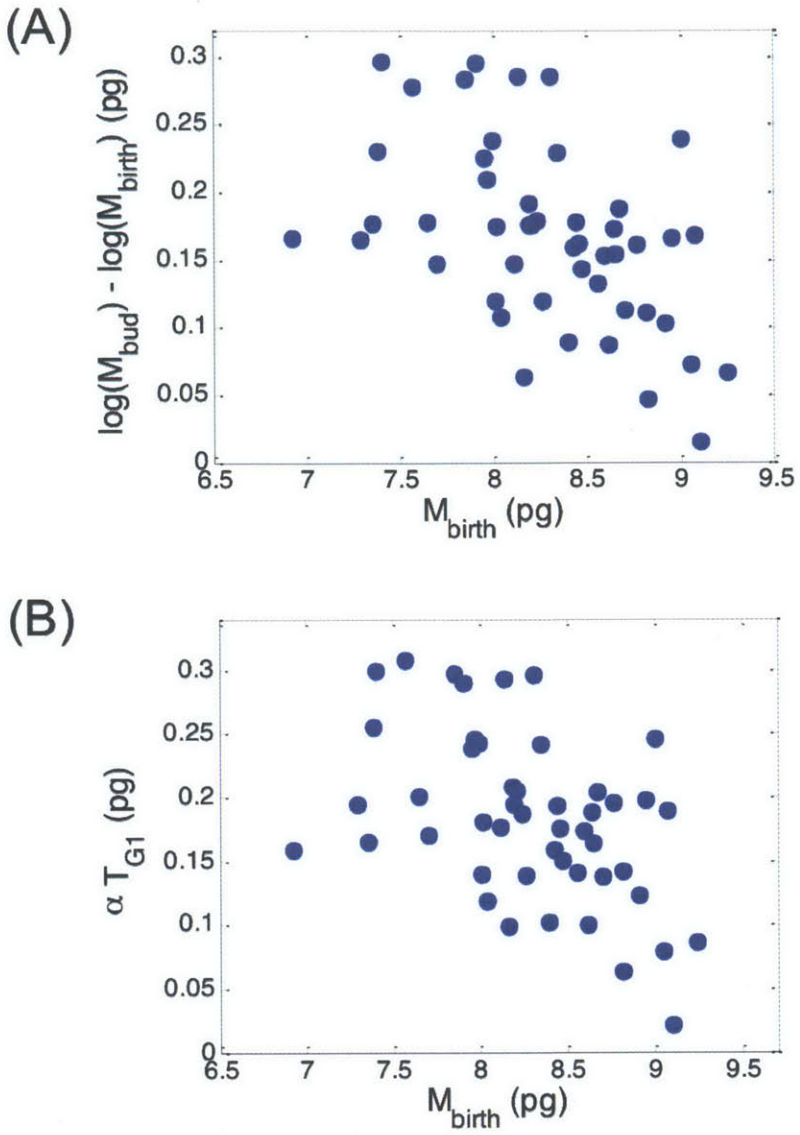

Figure 3-10: Fractional growth in G1 as function of birth mass, calculated two ways. (A) The fractional growth here was obtained by estimating the log of the ratio of budding and birth size (N = 50, slope = -0.59 ± 0.016, p = 1.28e-4, R^2 = 0.31). (B) Alternatively, the fractional growth can be estimated by performing exponential fits on individual trajectories and extracting the growth constant (α), to calculate alpha αT_{G1} (equivalent to $\ln(M_{bud}) - \ln(M_{birth})$ or $\ln(M_{bud}/M_{birth})$, as shown in the plot above), used in Di Talia et al. [15]. Fitting mass curves obtained from the SMR to an exponential model yields similar results as well (N = 50, slope = -0.63 ± 0.016, p = 2.64e-4, R^2 = 0.33).

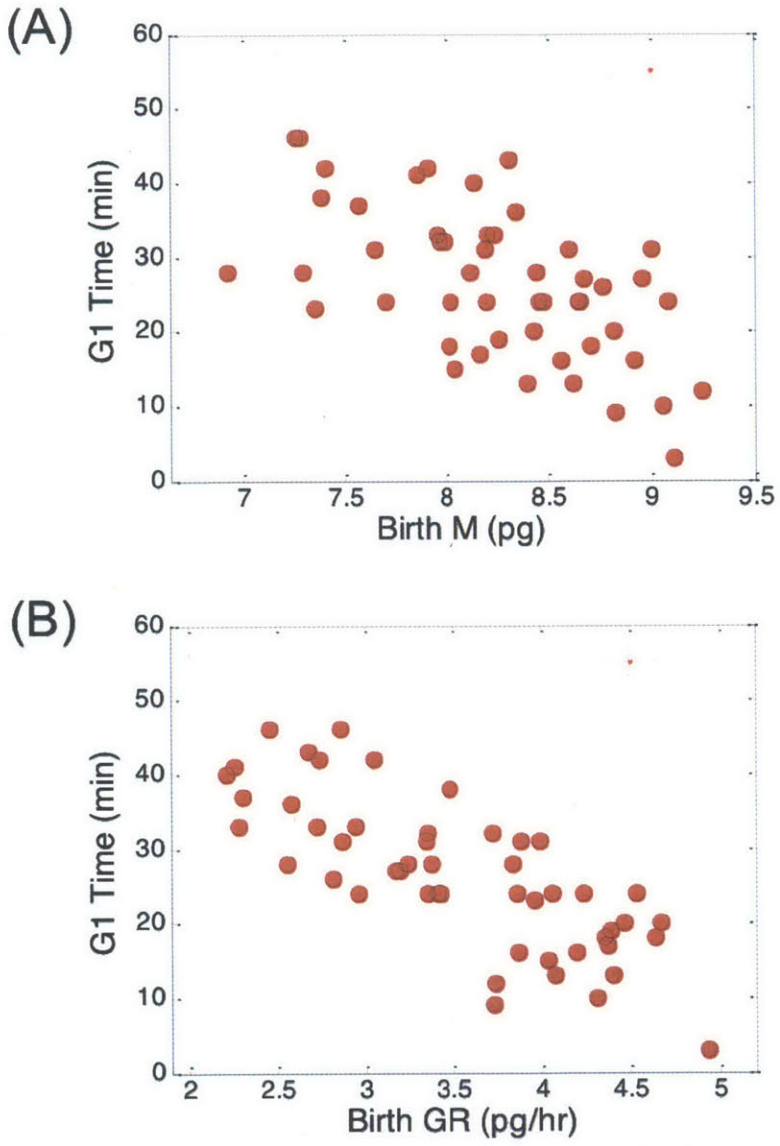

Figure 3-11: Correlation of G1 time with respect to birth mass and birth growth rate. (A) Duration of G1-phase as a function of birth mass (N=50, slope = -10.6 ± 2.1 p = 6.8e-6, R^2 = 0.35 ± 0.11). (B) Duration of G1-phase as a function of birth growth rate (N=50, slope = -10.6 ± 1.3, p = 4.9e-11, R^2 = 0.60 ± 0.08). Errors in measurement are shown in the top right corner of the plot. X error bars are determined by the measurement of a fixed cell, and its mass and growth rate error are determined to be 1 S.D. from the average mass and zero growth rate, respectively, for details refer to supplementary information (Fig. S2); Y error bars are determined based on the uncertainty (typically ~2 minutes or 50 frames) to determine an emerging bud.

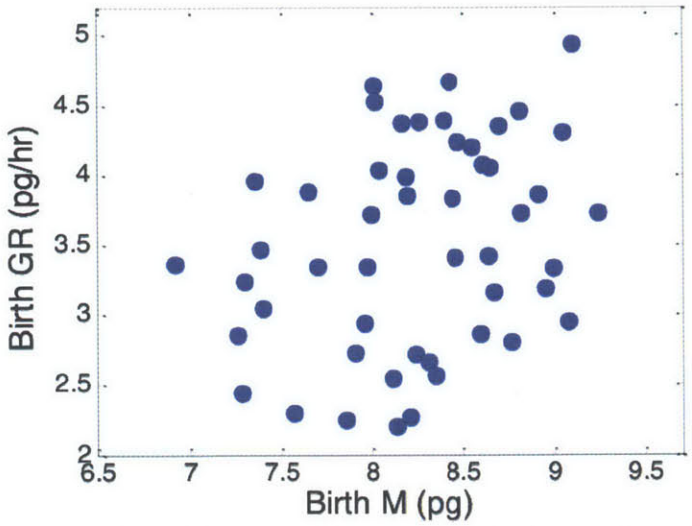

Figure 3-12: Relationship between the birth size-dependent metrics. Correlation between birth growth rate and birth mass (N = 50, slope = 0.40 ± 0.18, p = 0.032, R^2 = 0.09 ± 0.07).

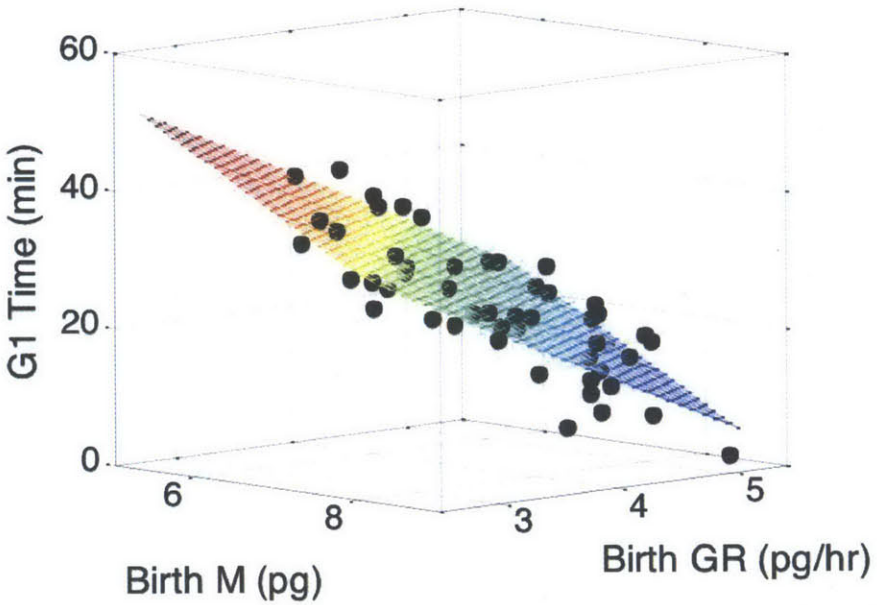

Figure 3-13: Two predictors of the G1 duration. The plane described by birth mass and birth growth rate accounts for 74% (R^2 = 0.74 +/- 0.08) of the variance in the duration of the G1 period. This model yields an F-statistic (2, 47) = 65.2 with a p-value = 2.7e-14 (N = 50).

Analysis of variance demonstrated that although newborn mass has a lower coefficient of determination than newborn growth rate in predicting G1 duration, newborn mass is not redundant, and is indeed a highly significant contributor to the model (see Table 3-2 and Section 3.6.7). Bayesian Information Criterion (BIC) values calculated for the mass only, growth-rate only, and combined mass and growth rate models indicate that the combined model is favored (Table 3-2C).

The strong correlation between nascent growth rate and G1 time is seen to rapidly decline, as the cell approaches the G1/S transition for subsequent three-minute windows (Figure 3-14). We hypothesize that this phenomenon is observed for two major reasons. Firstly, G1 phase can be decomposed into two temporally uncorrelated and functionally distinct steps, according to Cross and colleagues [15]. The first step, which depends on the G1 cyclin gene CLN3, corresponds to noisy size control that extends G1 in small daughters, but is of negligible duration in mothers. The second step, whose variability decreases with increasing CLN2 gene dosage, is similar in mothers and daughters and is not size-dependent. Since we have exclusively constrained our measurements to daughter cells, we are likely observing the exit from T1 and onset of the T2 after a few minutes of capture that leads to the correlation weakening significantly. Secondly, the cells are generally captured a few minutes following their birth, which causes lack of perfect synchrony in the cell-cycle time among the population. As such the correlation between growth rate and G1 time weakens rapidly following time of capture.

G1 phase is the most variable of the cell cycle stages. Prevailing models of cell cycle control invoke a critical size threshold to explain G1 variation [4, 42, 43]. Our results demonstrate that initial cell mass is a weak predictor of both fractional growth in G1 and time spent in G1. The growth rate at the beginning of G1 was more highly correlated with the length of G1 than birth size. Cells in unfavorable conditions are known to extend their G1 phase and delay the initiation of DNA synthesis [4, 43]. One possibility is that biosynthetic capacity at the end of the cell cycle determines how long the cell will spend in G1. Though we do not yet

understand the mechanistic basis for this observation, a previous study has found TORC1 activity to regulate the exit from mitosis in yeast [44].

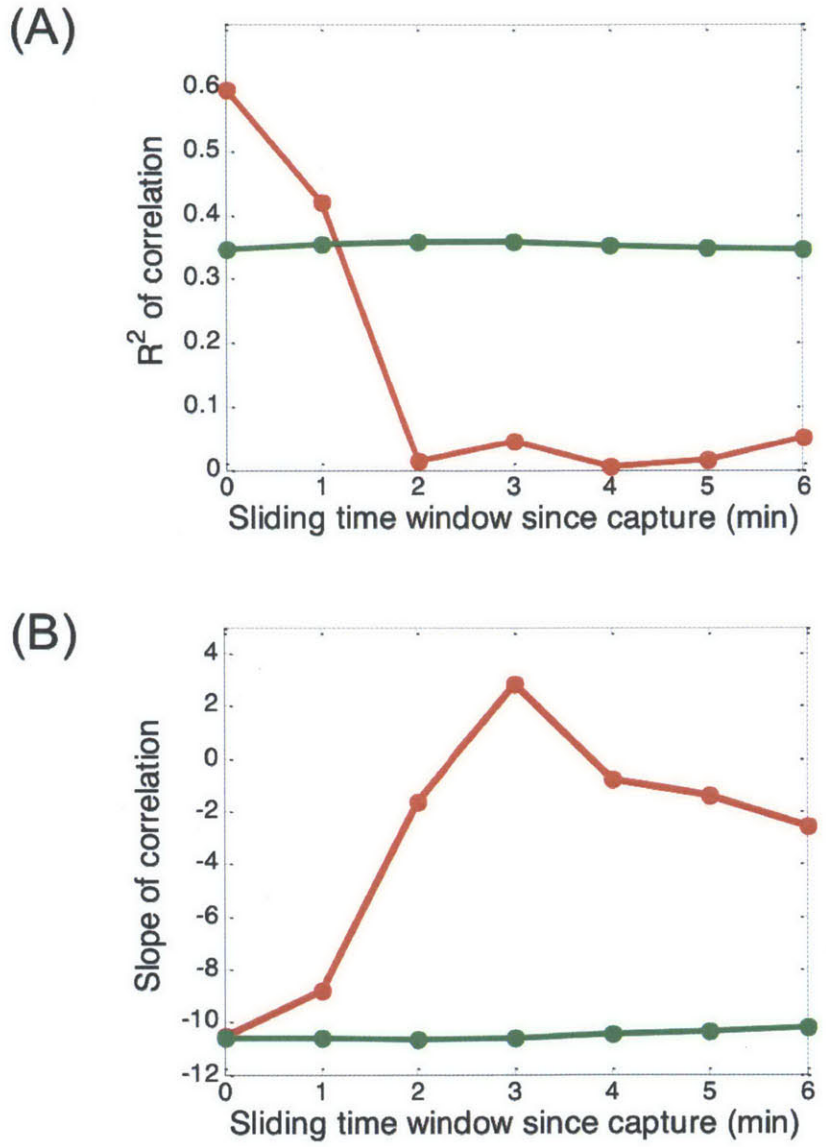

Figure 3-14: Correlation of instantaneous mass and growth rate evaluated with respect to G1 duration. The instantaneous parameters are calculated by a piecewise linear regression performed on a sliding 3-min window since the time of capture. The correlations for mass are indicated in green and that for growth rate are indicated in red. The slope and the coefficient of determination (R^2) of the resulting correlation are shown in (A) and (B), respectively.

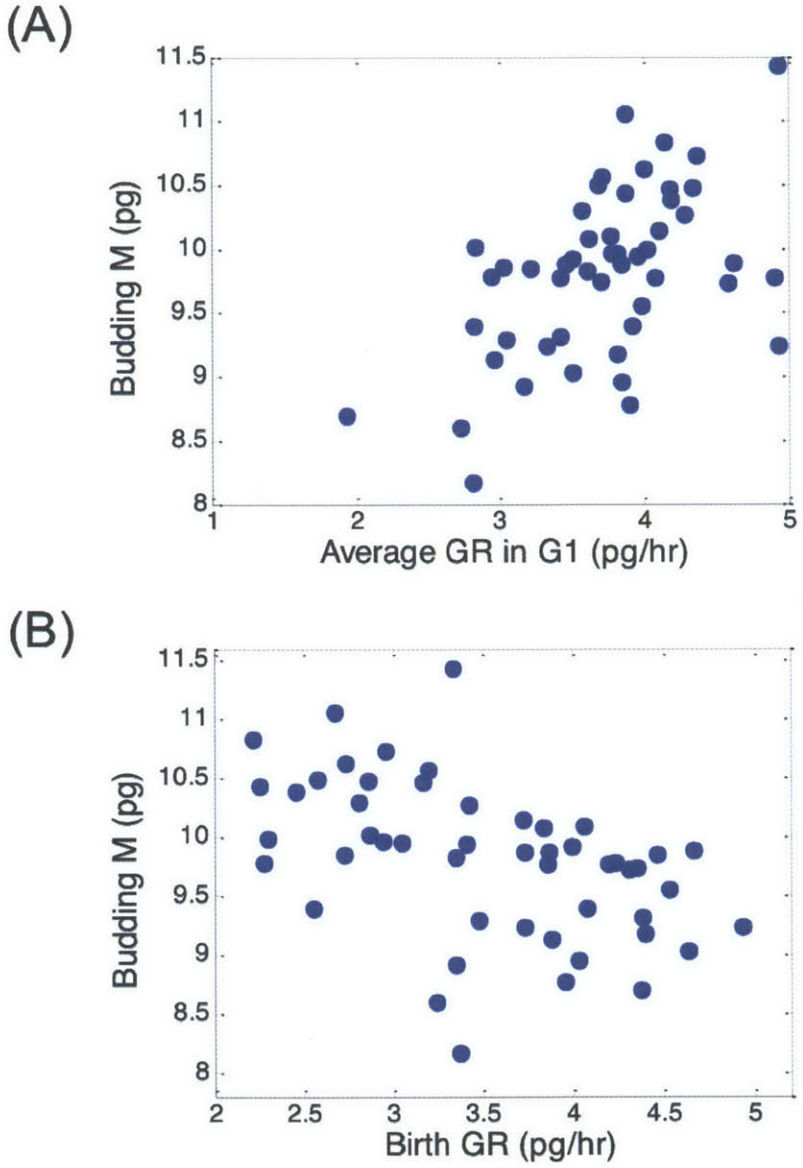

Figure 3-15: Relationship between budding size and growth rate. For the purpose of comparison, we calculate growth rate two ways – the average growth rate in G1 and the growth rate upon capture of newly born cells. (A) Correlation of mass at budding and average growth rate in G1 (N = 50, slope = 0.57, R^2 = 0.27); analogous to correlation reported in Ferrezuelo et al., 2012. (B) Correlation of mass at budding and newborn growth rate (N = 50, slope = -0.43, R^2 = 0.24).

A recent study by Ferrezuelo et al. reported that G1 growth rate sets a critical size in yeast cells [35]. There are important distinctions between our observations and the aforementioned study. First, Ferrezuelo et al. observe a strong positive correlation between size at START and average growth rate in G1. Our data does not support this finding (Figure 3-15). The second difference is that our data exhibits a correlation between newborn growth rate and G1 duration (Figure 3-11B). The data reported by Ferrezuelo et al. shows no correlation [35]. One possible explanation for these two discrepancies is that the fundamental measure of size is different. Ferrezuelo, et. al. measured volume by segmentation of DIC images. Our study measured buoyant mass, which is equal to the product of cell volume times the density difference between the cell and surrounding medium. It is known that density of budding yeast cells does not remain constant throughout the cell cycle and has been observed to increase around the time of budding [11, 45].

3.4 Maintenance of size homeostasis

The mechanism by which cells measure their size is not known. Cells could possibly measure their size directly or derive it from other inputs such as growth rate. This distinction is important because existing models for size control postulate a size checkpoint. If a size control mechanism exists, there would likely be a decrease in size variance around the time of budding relative to other points in the cell cycle, such as birth. We did not find evidence that mass variation decreases at budding (Levene's test, $p = 0.65$; Figure 3-16A). Growth rate at budding showed significantly less variation than newborn growth rate (Levene's test, $p = 0.0002$; Figure 3-16B). It is conceivable that regulation of homeostatic size distribution occurs through the modulation of growth rates, which in turn could govern the length of the G1 phase of the cell.

The corollary to the size control hypothesis is that given an exponential growth, the variance in sizes at budding (and consequently at division) should increase with every cell cycle, in the absence of a perfect sizer model. This becomes

especially important in light of asymmetric division in yeast. Say the cells spent a given period of time in G1 regardless of their birth size, smaller cells would on average give rise to even smaller cells, and their larger counterparts would become bigger with every subsequent division. However, we find that the coefficient of variance of the cells at budding does not show any significant increase (Figure 3-17), despite the imperfect sizer at play (Figure 3-10). As seen in Figure 3-17 that in the absence of growth regulation, theoretically the cell size at budding would exhibit a significant increase in the coefficient of variance.

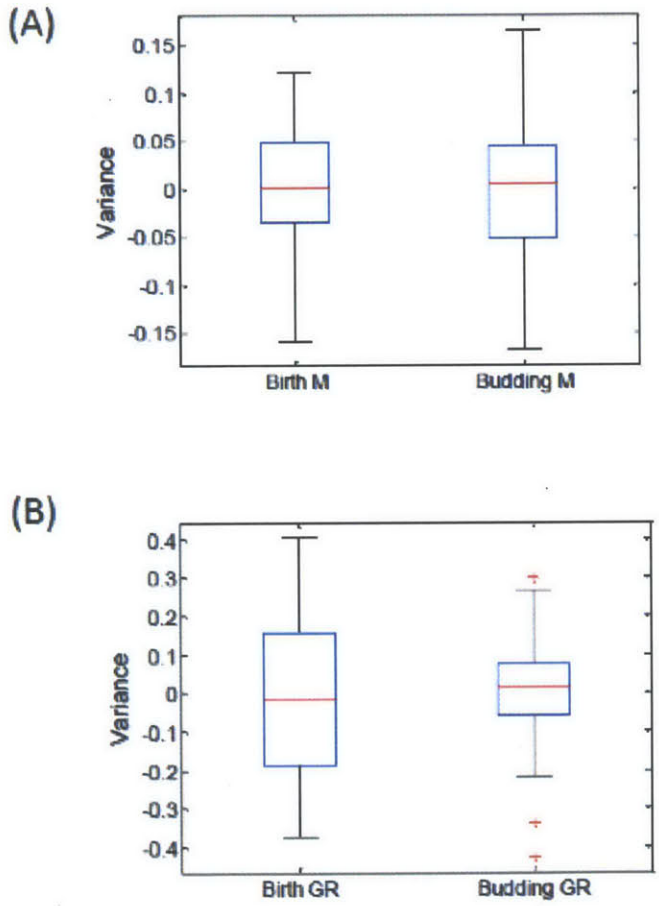

Figure 3-16: Examining the difference in the variance of mass and growth rate at two distinct points in the cell-cycle. The values in the mass and growth rates are normalized relative to their means and Levene's test is performed to assess the equality of the variances. Shown here are the median (red line), interquartile range (blue box and whiskers) and the outliers (red cross hairs). (A) Variances in mass are not significantly different; $p = 0.65$. (B) Variances in growth rate are significantly different; $p = 2.0e\text{-}4$.

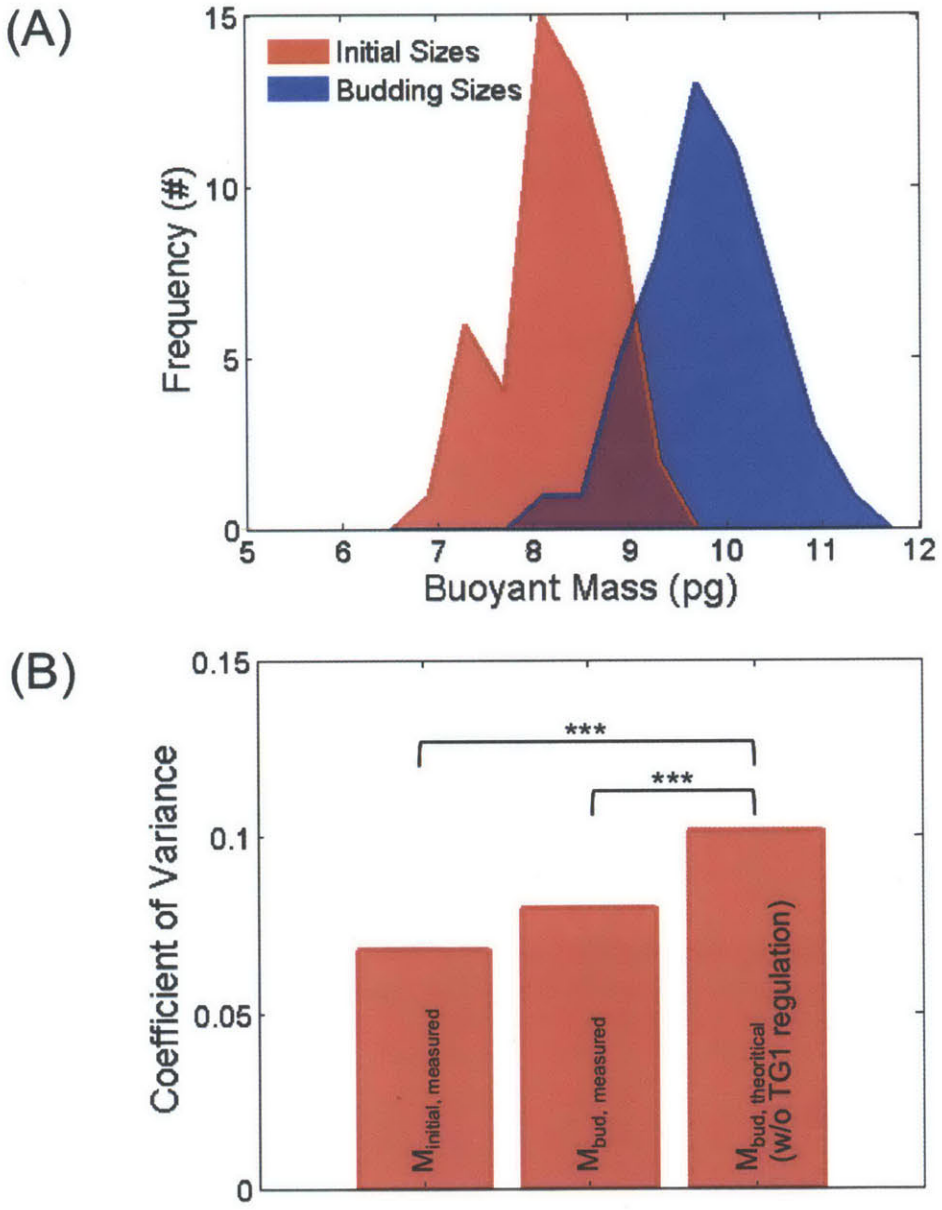

Figure 3-17: Maintenance of size homeostasis. (A) Distribution of the cell's buoyant mass both at initial capture (Mean = 8.24 pg, C.V. = 0.068, N = 50) in red, and at budding (Mean = 9.82 pg, C.V. = 0.080, N = 50) in blue. (B) Examining the coefficient of variance of measured initial masses, measured budding masses and theoretically calculated budding masses. The theoretical mass is calculated using a model that assumes exponential growth without regulation of G1 time. The difference in the C.V.s of measured values compared to the theoretical budding mass value is significant ($p<0.001$).

Size homeostasis is essentially the result of the coordination of cell growth and cell division processes. This coordination has to be an active process that integrates feedback from specific regulatory networks dedicated to converting the accrual of sufficient biomass or sufficient concentration of key transcription factors into a stimulus for cell cycle progression. One of the more popular models for size threshold is based on one of the G1 cyclins- Cln3. Cln3 lies upstream of the pathway that regulates the transcription of G1/S genes, and is thought to be a 'sizer' molecule. This model is based on the assumption that the cell needs to attain a certain translational rate to pass Start. Since Cln3 is an unstable protein, its relative nuclear abundance can be a proxy for the translation rate. Therefore the abundance of Cln3 can be indicative of not only the translation rate per ribosome but also the number of ribosomes, and a proxy for the cell instantaneous growth rate [5, 46]. As such, the variability in G1 that Cross and colleagues attribute to transcription noise of cycling expression [15], may very well be a result of the difference in nascent growth rates that we observe.

3.5 Conclusion

Five decades ago, a relationship between cell size and G1 duration was described based on the finding that daughter cells that are smaller than mother cells spent longer in the G1 phase [10], leading to the hypothesis that differences in G1 duration are attributable to differences in birth sizes, perhaps because cell size is an easy biophysical parameter to measure. In this study, we revisited the deterministic size model of cell cycle regulation. Our results support the existence of only a sloppy size control. When we closely examined the variability among the newly born cells, we found that growth rate in early G1 was a more significant contributor to variability in G1 duration.

Our data supports the hypothesis that growth rate is a closer proxy to the pathway that controls the onset of START. These findings are in agreement with a recent genetic screening study by Hoose et al. who reported that most of the gene

deletions that altered the G1 length did not significantly change cell size, but were instead strongly linked to ribosomal biogenesis and protein synthesis [47]. Additionally, a number of qualitative biochemical studies that altered growth rates using cycloheximide or titrating *Cln* levels, have similarly alluded to the hypothesis that biosynthetic capacity modulates the onset of the cell-cycle [48, 49]. There is strong evidence in literature that supports the role of Cln3-CDK to trigger transcription of Cln1/2 that in turn activates the transcription of START genes [7, 50-55]. Since Cln3 is an unstable protein molecule, its steady state concentration is dependent on the translation rate [5, 46]. Furthermore, translational capacity is dependent on ribosome biogenesis. Sfp1 and Sch9 were recently discovered in a genetic screen for small mutants [56]. These proteins are intimately tied to ribosome biogenesis and are downstream of the TOR and PKA pathways [56-60], linking growth rate and size regulation at the G1/S transition. In mammalian cells, S6K1 and Akt/PKB (Sch9 homolog) are downstream of mTOR and have been similarly found to be important regulators of cell growth and cell size [61].

3.6 Materials and Methods

3.6.1 Strain and growth conditions

Diploid *S. cerevisiae* strain (W303, MATa/MATalpha) was used in this study. Cells were grown and maintained at OD_{600} <0.7 in YEPD supplemented with 2% glucose at 30°C. For fixed cell measurements, cells were spun down, washed with PBS, treated with 4% paraformaldehyde for 24h, and resuspended in PBS.

3.6.2 Single-cell mass trajectories

Experimental Setup for SMR Measurement

Prior to loading the cell sample into the SMR system for growth measurement, an aliquot of the cell culture was sonicated for 15s to separate clumped cells. Cell sample is introduced into the SMR channels using pressure-driven flow, and the population of cells is screened until a cell within a predetermined newborn

buoyant mass range (7pg to 9.5pg) is encountered. Once the cell is weighed, the flow is reversed the remaining cells downstream are flushed out and fresh medium is introduced into the channels. The target cell is now dynamically trapped and its buoyant mass is measured every 10-15s using the procedure described in [28]. The cell is also imaged as it transits back into the cantilevered channel as shown in Fig. 1A with a frame rate of 2s in order to determine its budding time point. All measurements were performed at 30°C. We find that the shear stress on cells transiting the SMR channels is minimal since cells maintain growth rates in the SMR that agree well with those in bulk culture (Figure 3-5).

SMR Device Operation

The mass measurements were performed in a SMR device with a 315μm-long cantilever of with internal cross-sectional area of 15x20μm (channel height x width). The device was operated in the second vibrational mode as described in [19]. Frequency is measured by tracking the motion of the cantilever in feedback with a laser beam, mixing down the signal to 1KHz and period counting. Buoyant mass measurements were calibrated using 8μm polystyrene particles (NIST Traceable Particle Size Standards, NT25N).

3.6.3 Time-lapse microscopy

A modular microscope (Nikon) mounted on the SMR, and a 20x objective lens (Nikon-CFI LU Plan ELWD N.A. 0.40, WD 13 mm) was used to image the cells during their transit through the bypass. Images were acquired every 2s with a cooled CCD (Roper Scientific, Photometric CoolSNAP HQ). ImageJ was used for both image acquisition and analysis, with custom software integrated to automate camera operation. Resulting time-lapse movies were visually scored for budding to determine G1 time, with an accuracy of about two minutes (or 50 frames).

3.6.4 Determination of cell growth parameters

Mass and growth rate are determined from the raw mass versus time trajectories by performing a piece-wise linear fit with a 3-min window sliding at 1-min intervals (Figure 3-4). The fit's average value yields the instantaneous mass and its

slope yields the instantaneous growth rate. The 3-min window was chosen to maximize the confidence of the piece-wise fits as well to be congruent with optimal imaging frequency of 3 min in several recent studies [15, 35]. The system's error in the measurement of mass and growth is estimated from a fixed cell control, as shown in Figure 3-4. The errors in estimating newborn mass and growth rate for each individual trajectory is shown in Figure 3-18 below, unless the error in an individual cell's parameter is less than that of the system, then the error of the system is used instead.

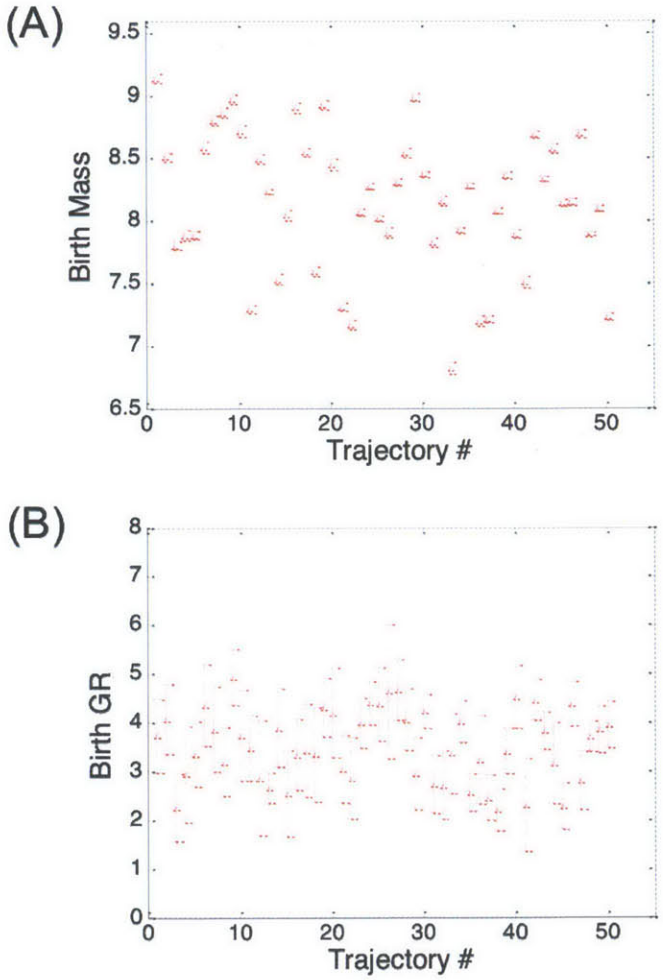

Figure 3-18: Error in the estimation of size metrics for individual trajectories. (A) Standard error in the determination of initial mass for each trajectory. (B) Standard error in the determination of initial growth rate for each trajectory. In the case that the standard error of the system (calculated from a fixed cell measurement) is greater than that of the individual cell measurement, the standard error of the system (calculated from measurement of a fixed cell) prevails.

3.6.5 Approximation of error in the coefficient of determination

The following formulae were employed to calculate standard error and confidence intervals for the coefficient of determination (or R^2) values [62, 63]:

(i) $$SE_{R^2} \approx \left(\frac{4R^2\left(1-R^2\right)^2(n-k-1)^2}{(n^2-1)(3+n)}\right)^{\frac{1}{2}}$$

where k is the number of predictors in the model and n is the total sample size.

(ii) $$CI = R^2 \pm t_{\left(\frac{1-\alpha}{2},n-k-1\right)} SE_{R^2}$$

where α is the desired confidence interval percentage, SE_{R^2} is the standard error for R^2, t is the value of the t-distribution, k is the number of predictors in the model and n is the total sample size.

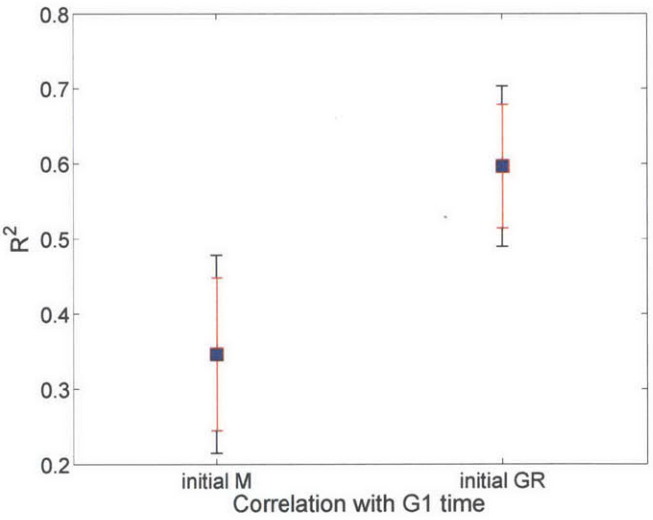

Figure 3-19: Approximation of the standard error (in red) and 90% confidence intervals for the coefficient of determination for the correlation of G1 time vs. initial mass (0.347+/-0.105) and of G1 time vs. initial growth rate (0.597+/-0.082), using the formulae from [62, 63].

3.6.6 Curve fitting and model selection criteria

The mass trajectories were fit using non-linear leas squares curve fitting function in MATLAB called *lsqcurvefit*. To analyze the growth pattern of the single budding yeast cells, the following models were applied:

Linear:

$$m = at + b$$

Bilinear:

$$m = \begin{cases} a_1 t + b_1, \text{for } t < t^* \\ a_2 t + b_2, \text{for } t \geq t^* \end{cases}$$, where t* is the rate change point.

Simple exponential:

$$m = ae^{bt}$$

Exponential with an offset:

$$m = ae^{bt} + c$$

These models have 2, 4, 2 and 3 parameters, respectively. As such we need a model selection criteria that takes into account the model complexity as well as the goodness-of-fit. The selection criteria employed to evaluate the best model that describes the mass versus time trajectory are shown below. The comparison of different curve fits for a representative trajectory shown in Table 3-1.

Coefficient of determination:

$$R^2 = 1 - \frac{RSS}{\sum_i (y_i - \overline{y})}$$

Reduced Chi squared:

$$\chi^2 = 1 - \frac{1}{n-p} RSS$$

Bayesian information criterion:

$$BIC = n \ln\left(\frac{RSS}{n}\right) + p \ln n$$

where $RSS = \sum_i (y_i - f_i)$ is the residual sum of squares, y_i is the i^{th} data point, fi is the i^{th} point predicted by the fit function, $\overline{y}$ the mean of the data, n the number of data points and p the number of parameters in the model. Perfectly fit data will have R^2 =1, and the lower the χ^2 and BIC values are the better the model describes the data.

3.6.7 Note: Model selection for the multiple linear regression

For the multiple regression of G1 time over nascent mass and nascent growth rate (Figure 3-13), we sought to determine the significance and the strength of the two predictors (Table 3-2). Though birth mass has a lower coefficient of determination than birth growth rate in describing G1 duration, it is not redundant, and is a highly significant contributor to the model as evaluated by the F-statistic in the analysis of variance (ANOVA).

Next, we explored the strength of the contribution of these predictors by calculating standardized coefficients calculated from the multiple linear regression. This metric indicates that one standard deviation change in birth growth rate can explain 0.7 standard deviation of change in G1 time, whereas one standard deviation change in birth mass can explain only 0.4 standard deviations of change in G1 time.

Furthermore, we look at the relevance of the 3 possible models that emerge as a result of these two predictors: (1) model with both M_{birth} and GR_{birth}, (2) model with GR_{birth} only, or (3) model with M_{birth} only. Using the BIC as an approximation of the integrated likelihood [64], we calculate that model (2) with GR_{birth} is ~170,000 times is a more probable model for describing G1 time than model (1) with M_{birth}, and that the combined model (1) with both GR_{birth} and M_{birth} is the most likely model (~5000 times more likely than model (2)).

In conclusion, while we find both predictors to be significant contributors to describing the variation in G1 time, growth rate provides a closer proxy than mass for the mechanism that is underlying the regulation of G1 duration.

3.7 Tables

Table 1 Goodness-of-fit for a single-cell mass trajectory

Fit	BIC	Chi Sq
Linear	-1763	17.25e-4
Bilinear	-2528	2.87e-4
Exponential	-2587	4.16e-4
Exponential with offset	-2689	4.17e-4

Table 3-1: Evaluating the goodness-of-fit using Bayesian information criteria and Chi-sqaured values for model selection. The values above are calculated for data shown in Figure 3-7.

Table 2 Summary of Multiple Linear Regression on G1 time with respect to birth mass and birth growth rate

(A) Multiple Linear Regression

	Estimate	Std. Error	t-value	Pr(>|t|)	Std. Coeff. (b)
Intercept	115.8	11.1	10.4	1.0e-13	-
Initial GR	-8.9	1.1	-8.3	9.2e-11	-0.7
Initial M	-7.0	1.4	-5.0	-1.0e-5	-0.4

(B) Analysis of Variance (ANOVA)

Model		Sum of Squares	F-statistic	p-value	Significance
Adding GR to M	M	1738	61.5	4.4e-10	***
	GR	1945	68.9	9.2e-11	***
Adding M to GR	GR	2991	105.9	1.3e-13	***
	M	692	24.5	1.0e-5	***

(C) Model Selection

	Model 1 GR, M & intercept	Model 2 GR only	Model 3 M only	Model 4 intercept only
nVar	2	1	1	0
R2	0.74	0.60	0.35	0
BIC	-59	-42	-17	0
Posterior probability	1	0	0	0

Table 3-2: (A) Summary of multiple linear regression on G1 time with respect to birth mass and birth growth rate. (B) Summary of the analysis of variance of stepwise regression to examine the contribution of each of the independent variables. (C) BIC, R^2, and posterior probabilities (calculated BIC, see [64])

3.9 Contributions

Gulati, Amneet and Manalis, Scott designed and conceived experiments. Gulati, Amneet performed experiments and analyzed data. Cermak, Nathan assisted in data analysis. Manalis, Scott contributed materials, reagents and analysis tools.

4 Continuous and long-term volume measurements

4.1 Introduction

In this chapter we demonstrate a method to enhance the time resolution of a commercial Coulter counter and enable continuous and long-term cell size measurements for growth rate analyses essential to understanding basic cellular processes, such as cell size regulation and cell cycle progression. Our simple modifications to a commercial Coulter counter create controllable cell culture conditions within the sample compartment and combine temperature control with necessary adaptations to achieve measurement stability over several hours. We also wrote custom software, to analyze instrument data files collected by either this continuous method or standard, periodic sampling. We use the continuous method to measure the growth rate of yeast in G1 during a prolonged arrest and, in different samples, the dependency of growth rate on cell size and cell cycle position in arrested and proliferating cells. We also quantify with high time resolution the response of mouse lymphoblast cell culture to drug treatment. This method provides a technique for continuous measurement of cell size that is applicable to a large variety of cell types and greatly expands the set of analysis tools available for the Coulter counter.

4.2 Methods for cell-sizing

Cell size is a fundamental property of all organisms and tissues. Size is coupled to cell cycle progression and is affected by both internal and external cues, as well as characteristic of certain disease states. The measurement of cell size over time offers insight into the rate at which cells transduce energy derived from nutrients into cellular biomass, and this information can be applied to molecular-level knowledge to further understanding of cell size regulation and predict cell fate. Size measurements by single cell tracking provide the highest level of detail, but are low throughput and face technical challenges because cells move or drift and require a steady nutrient supply [12, 36, 65]. Population-scale measurements at

fixed time intervals evaluate a large number of cells, but are often collapsed into qualitative descriptions or a single data point, such as a change in population mode or average [14, 32]. Moreover, population-scale data frequently lack the time resolution necessary to quantify any fast kinetics during a culture's response. A large-scale continuous size measurement captures with high time resolution valuable statistics about the population's size heterogeneity, describes how the average cell of any given size behaves, and more precisely identifies the dynamic of response of a population distribution to environmental perturbations.

Continuous population-scale volume measurements have not been achieved, mainly due to the lack of appropriate instruments and analysis tools. In addition to the requirement that cells be kept in culture conditions for the entirety of the timecourse, this style measurement must be ultra-high throughput without sacrificing precision. Tools for measuring cell volume are mostly limited to image analysis, light scatter, and the resistive-pulse (Coulter) technique. Image analysis enables relatively high resolution in a focused horizontal plane, but non-spherical cells larger than the objective's depth of field necessitate z-stack imaging and a computationally slow reconstruction process [66, 67]. Image acquisition may be as fast as 30 cells per second if cells are imaged in parallel, but the necessary processing to calculate volume can be slow and constitute a major source of error. Forward scatter (FSC) measurements can achieve rates exceeding 10,000 cells per second, but FSC is more closely related to cross-sectional area than volume, and it assumes all cells are spherical and have identical optical properties [68, 69]. Deviations in cell shape and content introduce error to FSC measurements and this error has been reported as being instrument-dependent [70], which makes it difficult to compare results across studies.

The commercial Coulter counter is also high-speed (~2000 cells per second) but, in contrast to FSC, its output is directly proportional to cell volume. The Coulter principle states that a cell transiting an aperture decreases the aperture's electrical conductivity in proportion to the volume of the cell [71]. The commercial

instrument's aperture is on a test tube-like structure that is directly immersed in a sample beaker (Figure 4-1), and cells are driven via negative pressure from the beaker into the tube by way of the aperture. The commercial version is designed for "instantaneous" volume profiling of large cell populations at discrete time points; however, many biological studies require dynamic measurements over an extended timecourse with quantitative analysis of how cells change with time. To address this, we present modifications and analysis tools for a commercial Coulter counter to continuously acquire population data from active cell culture and quantitatively describe cell response as a function of both volume and time.

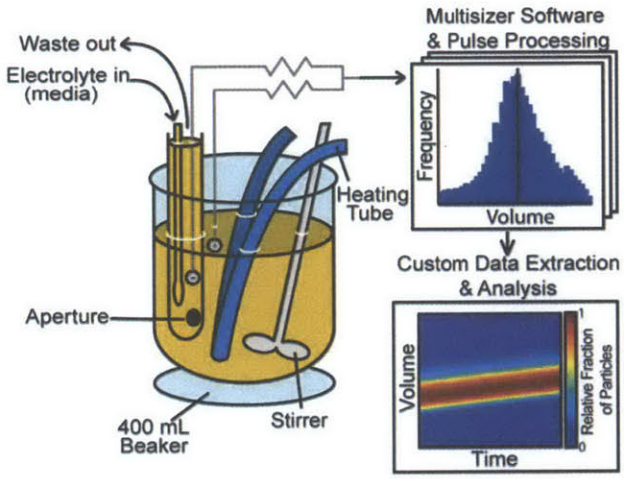

Figure 4-1: Schematic of setup within the sample compartment of a Beckman-Coulter Multisizer 4. The instrument electrolyte is exchanged for cell medium and 400 mL of cell culture is in a beaker on the sample platform. A heating tube and the Multisizer stirrer maintain culture temperature and a homogeneous suspension. The heating tube is connected to a temperature-controlled recirculating waterbath filled with deionized water, which minimizes electrical interference. Each 150 s file is stored by the Multisizer software and custom software reads the single-particle data from multiple files to plot volume for the timecourse.

4.3 Instrument modifications for measurement of culture volume response

The basic requirement for a large-scale continuous cell volume measurement is the ability to maintain cell cultures in temperature-controlled medium and homogeneous suspension during sampling. If the Coulter counter's sample beaker

is filled with cell medium and the electrolyte inside the aperture tube is commercial solution (Isoton II), there is a gradient of electrical conductivity through the aperture sensing zone that causes the initial volume measurements to be unreliable (Figure 4-2). We found volume measurements in medium are stable only when the instrument electrolyte closely matches that of the sample. Thus, we replaced the Isoton contents of the instrument with 0.2 μm filtered cell medium matched to each culture protocol (Figure 4-1). Additionally, we used the Multisizer 4 accessory stirrer to maintain a homogeneous cell suspension. In order to achieve temperature-controlled conditions within the commercial instrument, we passed into the sample compartment polyurethane tubing connected to a temperature-controlled recirculating bath (Figure 4-1). The recirculating bath must be filled with nonconductive liquid (*e.g.*, deionized water, oil) to shield the instrument from catastrophic electrical noise in the external environment. Even weak conductive paths between the environment and sample compartment interfere with the Coulter counter's electrical measurement. Although the ideal method for controlling culture temperature is a fluid-jacketed beaker and temperature feedback with a recirculating bath, we observed temperature stability to be within 1°C using our system (Figure 4-1). Temperature sensing methods should not electrically connect the external environment to the sample compartment, in the same way that fluid paths for temperature control must not interfere with the measurement. Temperature may be monitored either between file recordings with an external thermocouple or continuously by a thermocouple entirely contained within the sample compartment.

4.4 Commercial software set-up and description of custom data processing

In addition to establishing cell culture conditions, there are critical settings in the Multisizer software that allow for stable long-term measurements. One limitation of the commercial software is the 525 000 cell limit for each data file written. By recording a new data file every 150 s interspersed with aperture tube flushes,

millions of single-cell measurements for a culture may be collected over several hours. Regular flushing of the aperture tube reduces continuity (data are collected during ~75% of the measurement), but ultimately results in higher quality data. By this method, for instance a typical two-hour timecourse produces several million volume measurements distributed across ~40 raw Multisizer data files that are batch-processed by our custom software. Details for the extraction of time data from Multisizer files are provided in the Materials and Methods and MATLAB (Mathworks, Inc.) code is provided in the supplementary information. The fundamentals of the volume extraction are as follows:

(i) Cell diameter is calculated from each peak height, according to Beckman-Coulter, as:

$$diameter = Kd \sqrt[3]{\frac{height}{countspervolt.25.gain.current}}$$

where *Kd*, *gain*, and *current* are constants reported in the header of each file; *height* is the sum of a correction factor and the first of five hexadecimal-encoded values recorded for each cell measurement; and *countspervolt* is 838 870 V^{-1}.

(ii) Particle volume is calculated as:

$$volume = \frac{\pi}{6} diameter^3$$

The Coulter principle measures volume, but the traditional output parameter for the commercial instrument is the spherical equivalent diameter, or Heywood diameter, given by Equation 1. Errors in the volume measurement result from elongated particles that widen the size distribution as a result of the instrument's orientation-dependent measurement [72-74] and particles that travel near the outer edges of the aperture [75]. Since particle path is related to pulse width, or time the particle spends in the aperture, pulse width could be used to exclude many of these erroneous measurements. Multiple particles within the aperture are also a source of measurement error and increased pulse width.

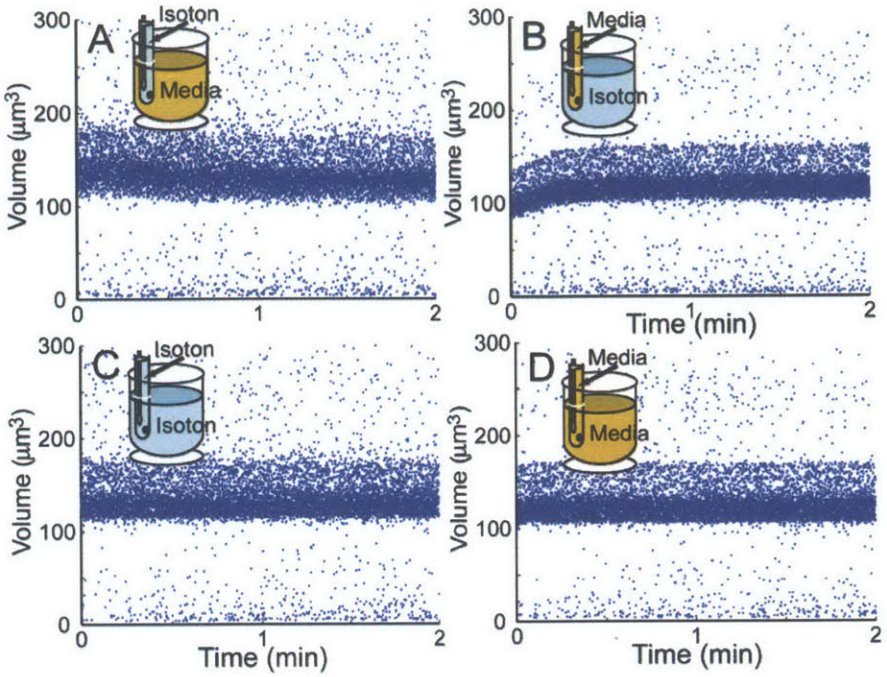

Figure 4-2: Volume measurements are unreliable (up to 20% error) for mismatched electrolyte and diluent conditions. (A, B) For a mismatched system electrolyte (inside aperture tube) and sample solution (beaker) there is a ~30s period required for the measurement to stabilize. During this period the sample solution fills the inside of the aperture tube and finally creates matched solution conditions across the aperture sensing zone. During a continuous measurement, thisdrift would be observed after every instrument flush, or between each recorded file (every 150s). (C,D) Volume measurements are stable through the entire measurement if the system electrolyte and sample solution are identical.

4.5 Assessment of error during long-term volume measurements

In order to investigate the stability of continuous and long-term data acquisition, we measured beads and G1-arrested yeast (*cdc28-4*) over a 2-hour timecourse (Figure 4-3AB). These data are represented by a colormap in which the number of cells located in a small area is designated by a color. Any deviation in the bead volume distribution is entirely due to measurement error. G1-arrested yeast data provide an example of a biological sample actively maintained and measured within the instrument. The G1 arrest is achieved by a temperature-sensitive allele of Cdc28, a protein kinase in yeast required for passage through Start [76]. At high temperature (>34ºC) the protein is inactivated and cells arrest in G1. Colormaps of volume timecourses are drawn directly from single-particle data rather than

exported histograms and may be constructed with any time and volume resolution dependent on the analysis parameters. Occasionally, debris partially occludes the aperture and introduces an error that is resolved by a flush or unblock of the aperture tube and subsequently the start of a new file (Figure 4-4). The commercial software does not save data if there is a flush or unblock before the end of the file and the number of automatic unblocks is limited by the commercial software to 9. Data skewed by debris were identified as those files in which a specific feature of the size distribution was greater than that of the two neighboring files (further details in Materials and Methods), and these were replaced by data interpolated from the neighboring files. This interpolation criterion removes short timescale fluctuations (~150s), which are not biologically relevant for the samples we measured. Faster events may require alternative constraints. Volume timecourse colormaps without interpolation are provided in Figure 4-5AB for comparison. As an alternative to data interpolation, spiking each cell sample with a large and small internal bead standard could be used to correct data during partial occlusions by imposing the constraint that bead volume distributions do not change during the experiment's timecourse. Ideally, a weak and rapid pressure reversal that does not interrupt data collection would eliminate the need for interpolation.

Continuous data collection enables growth rates to be reported with high frequency and nearly any averaging or smoothing window size. The calculated growth rates for beads (Figure 4-3C, blue) establish the method's growth rate resolution to be as low as 0.111 μm^3/min (three standard deviations, 60 minute averaging window) and significantly smaller than the growth rates observed for G1 arrested cells (Figure 4-3C, red). The arrested cell sample's growth rate remains elevated (Figure 4-3C), which is supported by previous results in which G1-arrested cells maintain growth over several hours [14]. As the averaging window sizes increases, the calculated rates converge to the average. For some samples, smaller averaging windows may reveal features that correlate with specific biological events.

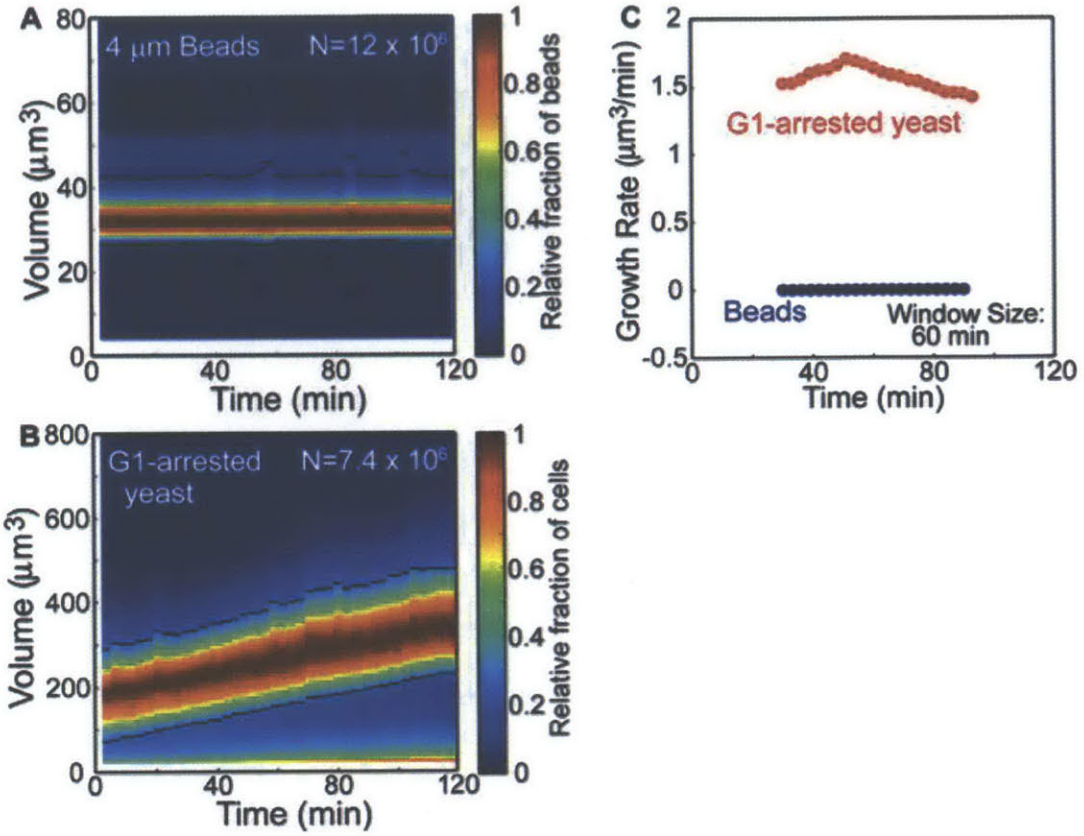

Figure 4-3: High resolution volume timecourse and growth rates of particles and cells. (A) 4.000 ± 0.033 μm diameter beads (Duke Scientific) and (B) *cdc28-4* G1-arrested yeast volume measurements over a 2 hour timecourse. Color designates the relative fraction of particles in each 150s measurement with the indicated volume (colorbar at right). Black lines designate the exclusion bounds used for growth rate calculations. (C) Growth rates for bead (blue, A) and yeast (red, B) data calculated by linear regression on a 60 min window shifted every 3 min. Bead data growth rates are 0.004 ± 0.037 μm^3/min (mean ± SD) and provide an estimate of measurement error. Additional error estimates were performed on 7.979 ± 0.075 μm diameter beads (Duke Scientific) (growth rates: 0.013 ± 0.169 μm^3/min) and formaldehyde-fixed cells (growth rates: -0.022 ± 0.118 μm^3/min). Continuous sampling and single particle data increases statistical significance for growth.

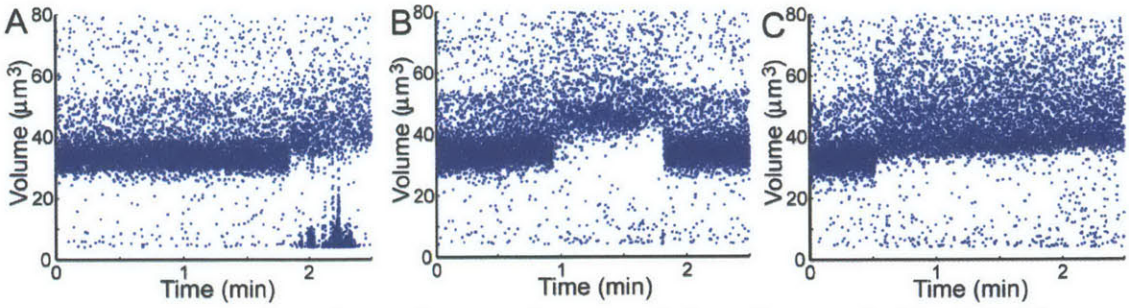

Figure 4-4: Examples of interference. In general, interference is identified by an instantaneous increase in the population's volume. A flush or unblock procedure at the end of the recorded file almost always resolves the problem. (A) "Small" and "large" particle count spontaneously increases. (B) "Large" particle count temporarily increases and then decreases, presumably when the aperture is cleared. (C) Same as B except erroneously measured volume steadily increases through the remainder of the measurement.

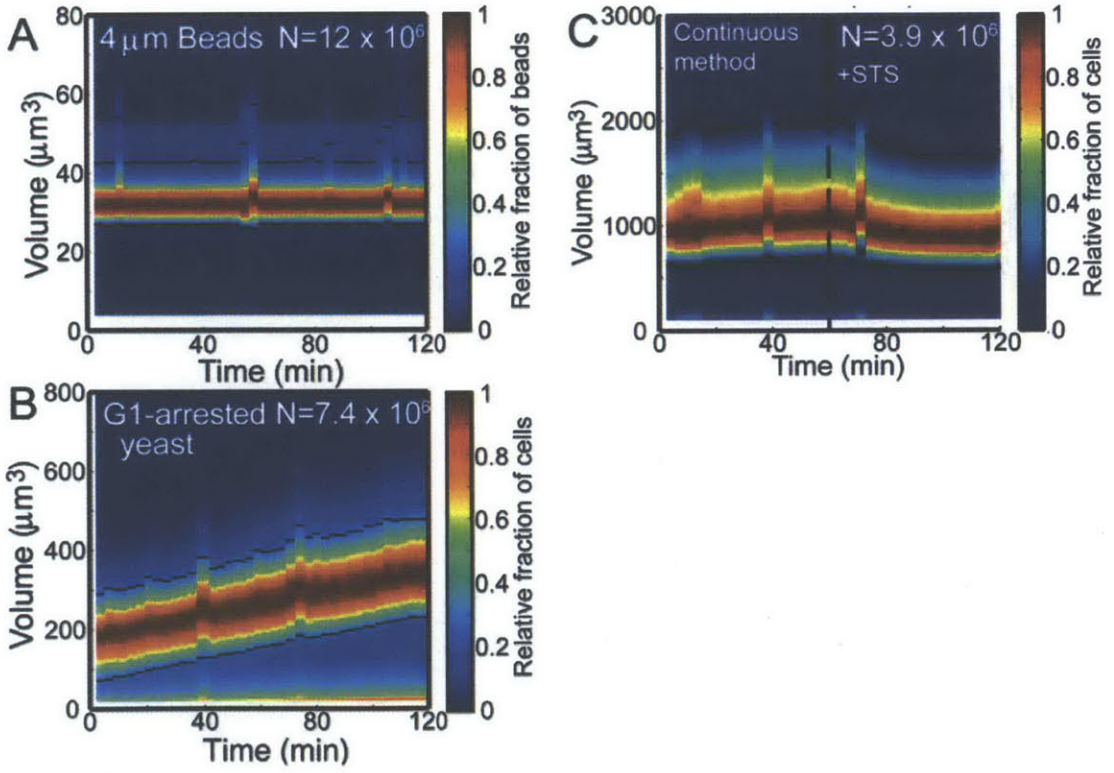

Figure 4-5: Volume timecourse colormaps before interpolation. (A) Figure 4-3A(B) Figure 4-3B (C) Figure 4-6B.

4.6 Rapid detection of growth rate perturbations in mammalian cell culture

In order to determine the time resolution at which cell response may be detected and demonstrate the method for mammalian cells, we continuously measured the volume of a mouse lymphoblast leukemia (L1210) cell line before and after treatment with staurosporine. Staurosporine is an inducer of the intrinsic apoptotic pathway, for which the first stage is apoptotic volume decrease (AVD) [77]. AVD is clearly detected within 30 minutes by standard protocols that track the mode of a volume distribution measured at fixed time intervals (Figure 4-6A), but a general and quantitative method for determining how early this change occurs could provide insight into the time required by certain pathways to induce changes to a cell's biophysical properties, such as size. During the initial stages of AVD, ion pumps that maintain homeostatic ion balance across the cell membrane shut down [77, 78], thus changes to cell size in response to staurosporine are similar to those during osmotic shock. The time for a change in cell size to occur consists of the time needed for the cells to respond and the system to detect the change. In order to determine this time, L1210 cells were measured for 1 hour, treated with 0.5 ☐M staurosporine, and measured for an additional hour (Figure 4-6B, upper panel).

These data were analyzed with a bilinear model (similar to [79]) in which the entire dataset is broken in two and a linear regression is performed on each part. The location of the separation is varied across the timecourse and the goodness of fit was measured by the sum of squared errors from both regressions. A decrease in the sum of squared errors indicates an improvement in the bilinear fit (Figure 4-6B, lower panel). A mock-treated sample (equal volume DMSO) demonstrates no improvement in the fit because its measured volume is constant and there is no optimal point for the separation. Cells treated with staurosporine show a dramatic fit improvement at ~9.7 min. This analysis highlights the continuous method's ability to precisely identify a population's response to changes in environmental conditions without prior knowledge of the timing or

timescale of this change. The brevity of this time indicates that the size changes must occur by fast-acting pathways, such as those reported in previous literature.

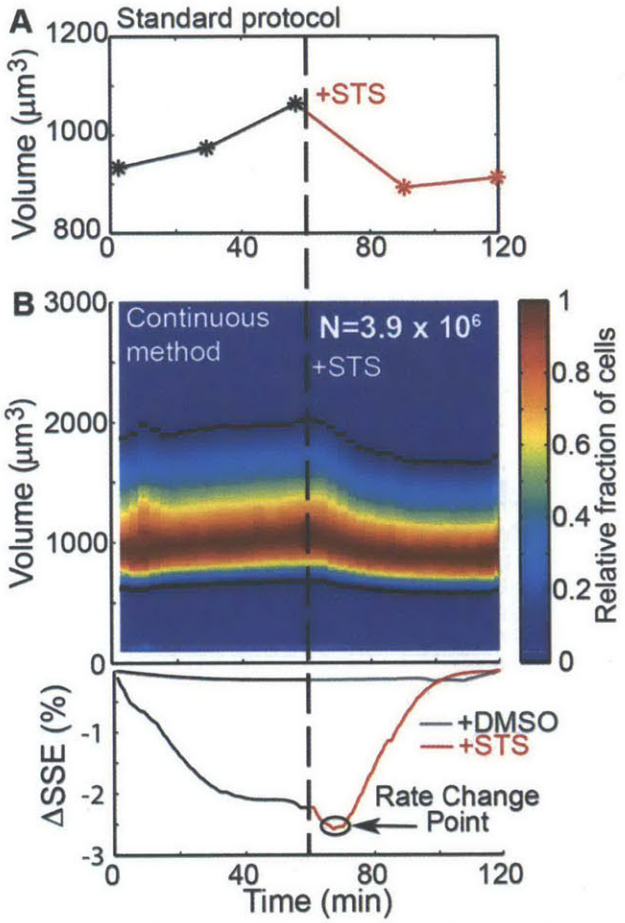

Figure 4-6: Timing of drug response by continuous volume data. After exposure to 0.5 M staurosporine (STS), mouse lymphoblast leukemia cells (L1210) exhibit an average volume decrease, likely associated with the early stages of apoptosis. (A) In a standard protocol, volume measurements are recorded and a histogram mode is reported (stars) every 30 minutes. With these data, the time at which cells respond to environmental perturbations can be determined with ~30 minute precision. (B) Continuous volume data for the same sample (colormap) provides a more complete description of the treatment's effect. For example, not only does a volume decrease occur following STS treatment, but there is a decrease in the population's variation. These data are then quantitatively analyzed to determine the time at which the measurement detects the culture response. Black lines designate the exclusion bounds (B, colormap black lines), or data removed from analysis. A linear regression is calculated for data before and after a breakpoint varied across the entire timecourse. For each of these points, the goodness of fit is measured by the sum of squared errors (SSE) and the minimum SSE indicates the time at which a change in volume growth rate is detected—the rate change point. L1210 cells treated with equal volume DMSO exhibit no significant rate change point, and a response in staurosporine-treated cells was detected at ~9.7 min after drug exposure.

4.7 Growth rate calculations for size-based subpopulations

We next used this method to track populations of cells other than those represented by the mode of a histogram. We first investigated yeast growing at room temperature and arrested by a kinase inhibitor (1-NM-PP1) that inactivates Cdc28 (*cdc28-as1*). For single-peaked histograms, which we observed for timecourses measured at room temperature, small and large cells may be separately tracked by specific histogram features, such as bound pairs. Bound pairs are defined as the volume for which the count is X% of the mode (Figure 4-7A) and consist of one bound on each side of the mode. Bound pairs ease the tracking of changes in histogram shape over large datasets (Figure 4-7B). Although the result is similar to the volume timecourse colormaps shown in Figure 4-3 and Figure 4-6, this information enables growth rate data to be calculated independently for subpopulations of the culture measured together. In arrested cells and other samples in which cells do not divide, these growth rates are correlated to cells of a specific size and cell cycle phase (Figure 4-7C). Yeast arrested in the cell cycle have a growth rate dependent on cell size, similar to observations in cycling populations [20], but within a given size class the growth of arrested cells is relatively constant throughout the timecourse. Thus, Cdc28-inactivated yeast appear to have a diminished capacity to accelerate growth even as cells increase in size.

For samples with emerging subpopulations, the modes of each can be identified as local peaks and tracked individually (Figure 4-7D). We observed multi-peaked distributions to occur in cells with Cdc28 inactivation and grown at the optimal temperature for yeast (30ºC). During the first hour of arrest the distribution is single-peaked and analysis is as described previously, but subpopulations later appear as a result of elevated growth rates (Figure 4-7EF). The G1-labeled population closely correlates with a population grown in parallel culture and maintained in an incubated shaker (30ºC, 300 RPM). Although Cdc28 inactivation by 1-NM-PP1 arrests most cells in G1, a significant fraction of the population arrests as large budded cells. This is in agreement with work by Bishop

et al. [80], which reports an arrest with both unbudded G1 cells and large budded G2/M cells at the same inhibitor concentration (5μm). The M-labeled population likely represents the metaphase-arrested cells we observed in parallel culture. These G1- and metaphase-arrested populations are also present in the cultures grown at room temperature, but their size distributions are indistinguishable. The SG-labeled population represents a population of slow-growing cells that are not present in a flask-grown culture and are not altered by sonication. This subpopulation may be sensitive to reduced aeration in the sample compartment and result from *cdc28-as1* cells' deficient growth [80]. The proportion of cells in each subpopulation is color-coded for reference (Figure 4-7E). The widening of the distribution (Figure 4-7BE, distance between bound pairs) is a result of the size-dependent growth rates and diverging subpopulations that likely reflect cell cycle position.

We next wanted to compare results for arrested cells to measurements for a population of synchronously proliferating cells. To accomplish this, we isolated G1-phase cells (Table 4-1) by centrifugal elutriation and resuspended the population in YEPD for synchronous cell cycle progression. The elutriated cells (Figure 4-8A) have a prolonged G1 due to their initial small size and overnight growth in raffinose, and these cells begin to bud, or enter S-phase, near 200 min (Fig 5B). Bud calculations were recorded from a parallel flask-grown culture, and the volume distributions' mode from these aliquots closely match those of the continuously measured population (Figure 4-9). The G1-phase growth of elutriated cells (Figure 4-8A) is better fit to an exponential rather than a linear function (Table 4-2), which is in contrast to the more linear growth pattern of G1-arrested cells (Figure 4-3B and Figure 4-7B). The growth rate continues to increase as cells progress through S-phase, and subpopulations emerge concurrently with the appearance of a second generation of cells in the parallel culture (Figure 4-8AB, 225 min). As expected, the population begins to lose synchrony over time and the calculated bounds diverge.

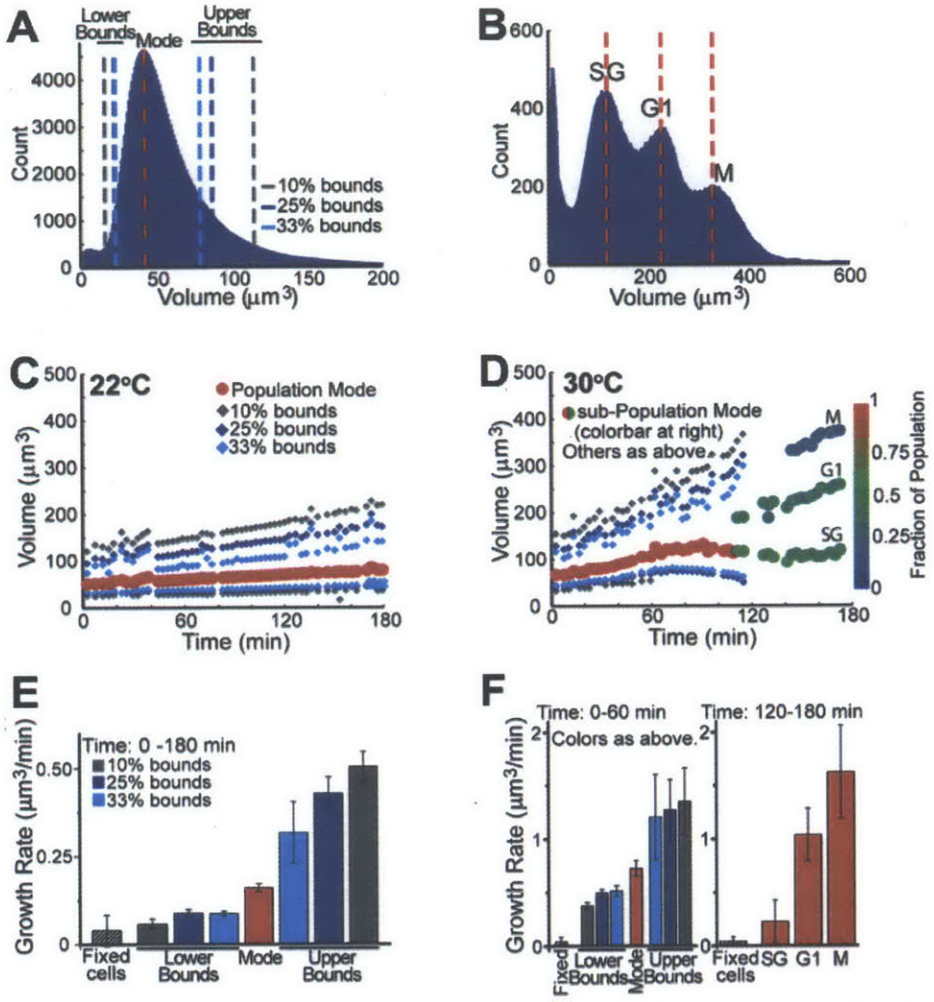

Figure 4-7: Subpopulation tracking by volume histograms. Continuous volume measurements of an arrest in *cdc28-as1* yeast over a 3-hour timecourse show cells arrested at various points in the cell cycle. (A) Histogram features, such as bounds, on single-mode volume distributions separately analyze large and small cells. (B) At room temperature (~22°C), cell volume steadily increases with a single population mode, and (C) the arrested cells' volume growth rates increase with cell size. Error bars on *cdc28-as1* data indicate the 95% confidence interval for the linear regression. The growth rate average (n=6) and measured standard deviation (error bar) for formaldehyde-fixed cells with a 60 min window are shown for comparison to measurement error. (D) Subpopulations emerge at the optimal temperature for yeast (~30°C) and a later timepoint (~120min), and the mode of each subpopulation is identified and tracked. These subpopulations likely represent slow-growing (SG), G1-arrested (G1), and metaphase-arrested (M) cells. (E) Histogram features are determined for each 150 s file, similar to those in B. The color of the solid circles indicates the fraction of cells in each subpopulation. Growth rates calculated with data in B and E are by linear regression on a 60 or 180 min window, as indicated. (F) Growth rates are separately calculated for a one hour window before and after the emergence of subpopulations. Fixed cell data is identical to that in C. As observed for room temperature measurements, growth rates are related to cell size and likely a result of the multi-phase arrest.

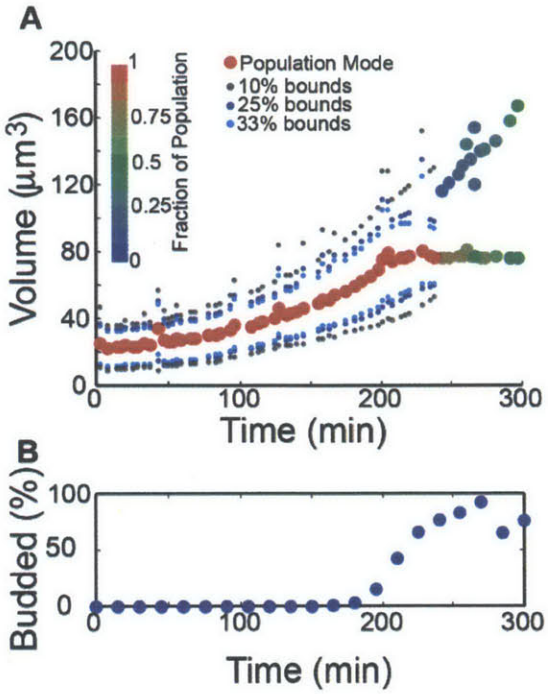

Figure 4-8: Continuous volume measurements of cells synchronized by elutriation (A) A population of G1-phase yeast were collected via centrifugal elutriation and volume was continuously measured as cells synchronously progressed through the cell cycle. Size classes are indicated by the calculated bound pairs and the rate of growth for all size classes increases throughout the timecourse, even with the prolonged G1-phase. As the timecourse progresses, the cells lose synchrony and a bimodal population emerges. After 240 min, the mode of each subpopulation is tracked and bound pairs are omitted. (B) Fraction of budded cells budded in the population measured in Fig 5A.

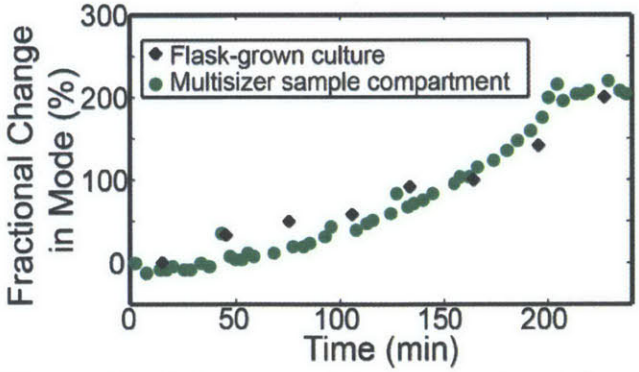

Figure 4-9: Culture condition comparison. The modes of volume distributions were recorded from live Multisizer chamber-grown and fixed aliquots of flask-grown parallel cultures used to produce Figure 4-8. In order to provide a more direct comparison between live and fixed cells, the percent change in volume from the timecourse's start is reported. In elutriated wild-type yeast, the culture conditions in a Multisizer sample compartment and a standard flask produce similar results.

4.8 Conclusion

Analysis of changes to cell size distribution provides fundamental insight into cell size regulation. Although there are well established cell size measurement tools, each have a fundamental tradeoff between throughput and time resolution. The method described here enhances the time resolution of a commercial Coulter counter's rapid, single-cell volume measurement by creating cell culture conditions within the sample compartment and improving long-term measurement stability. We also detail the requirements for extraction of volume and corresponding time data for timecourse analyses longer than a single file's measurement time, which is applicable to data collected by standard periodic sampling and the continuous method presented here. These methods for the extended analysis of cell size distributions are readily accessible to all users of a Beckman-Coulter Multisizer. We employ this method to describe cell growth as a function of size and cell cycle position in yeast and identify the response time for a mouse lymphoblast cell culture after drug treatment, but it may be applied to a variety of suspension cell systems and biological questions that could benefit from a dynamical cell size measurements.

4.9 Materials and Methods

4.9.1 Multisizer 4 measurements

The system electrolyte was replaced with medium closely matched to the cells' growth medium. A 400mL Multisizer beaker with pre-warmed growth medium was equilibrated to a sample-appropriate temperature by a polyurethane heating tube connected to a temperature-controlled recirculating bath (NESLAB RTE-111) and integrated stirrer (speed for yeast: 15, L1210: 5). Cells were added to the prepared beaker for a final concentration of ~7500 mL^{-1} (5-7% coincidence correction). Back-to-back 150 s measurements with a 100 μm aperture tube and intermediate flushes were recorded for the duration of the timecourse. Occasionally, debris remained on the aperture after a flush, and an unblock

operation was initiated by the user if a sharp increase in aperture resistance occurred during the first half of a measurement. For long timecourses, the sample beaker volume was replenished with pre-warmed (if necessary, pre-treated) growth medium to maintain sample temperature and sufficient volume for measurement. Alternatively, a basic pump system may be implemented to continuously exchange medium during the measurement.

4.9.2 Yeast strains, growth conditions and sample preparation

Cells were grown to OD_{600}<0.7 in YEP supplemented with 2% glucose (YEPD) at room temperature (~21ºC). For *cdc28-as1*, cells were arrested with 1-NM-PP1 (5 μM) at either room temperature or 30 ºC, and for *cdc28-4*, cells were arrested by temperature shift (34ºC). After 1h at arrest conditions, yeast were washed via vacuum filtration, resuspended in 0.2 μm filtered YEPD, sonicated, and transferred to a measurement beaker with identical arrest conditions (*cdc28-as1*: YEPD with 5 μM 1-NM-PP1 at 21ºC or 30ºC, *cdc28-4*: YEPD at 34ºC). The Multisizer system electrolyte was 0.2 μm-filtered YEP. Additional pre-warmed growth medium was added after 2h of measurement to better maintain sample temperature and increase sample volume. The first hour of arrest conditions was not measured because it mostly consists of the population collecting into the arrested phase and does not accurately portray an arrested population.

4.9.3 Elutriation

Cells were grown overnight in YEP + 2% raffinose at 30°C, synchronized by centrifugal elutriation [81], and resuspended in YEP + 2% glucose at 30°C. Aliquots from a parallel flask-grown culture were collected into 3.7% paraformaldehyde at indicated timepoints for quantifying the presence of buds. The Multisizer system was prepared and maintained as described above.

4.9.4 L1210 growth conditions and sample preparation

Cells were grown at 37 °C in L-15 medium (Gibco/Invitrogen, Carlsbad, CA) supplemented with 0.4% (w/v) glucose, 10% (v/v) fetal bovine serum, 100 I.U.

penicillin, and 100 μg/mL streptomycin. Cells were passaged every 2-3 days to maintain a cell concentration of ~100,000 mL^{-1}. For measurement, cells were transferred to the Multisizer beaker with pre-warmed medium identical to growth medium and allowed to equilibrate for 30 min before measurement. After ~1 hour of measurement, cells were treated with 0.5 μM staurosporine or an equal volume of dimethyl sulfoxide (DMSO; mock-treated control) and measured for an additional hour. The Multisizer system electrolyte was L-15 medium.

4.9.5 Data extraction, interpolation, and analysis

Raw Multisizer files were batch-processed with custom MATLAB software. This software is necessary for timecourses longer than a single file because combining files within the commercial software resets the start time of each file to zero and makes rate analysis for cell cycle progression or drug response impractical. Furthermore, data exported from the commercial software are limited to 5 010 pulses per file and files must be handled individually. The custom software batch-processes raw Multisizer data files to acquire time and volume data for all measurements and extend the time axis beyond that of a single file. The method for volume data extraction is described in the main text. The corresponding time data are provided in two sections of the raw Multisizer file. Every 200 ms the instrument records the time passed and the number of measurements that have occurred since the measurement began. Volume measurements are linearly distributed across each 200 ms time step such that each cell measurement has at least 200 ms time resolution.

For each file, the lowest 2% of data by volume were excluded from analysis as instrument noise. Bound pairs were determined for each file and data outside of a certain bound pair (exclusion bounds), typically the 10% bound pair, were excluded from rate analysis. Extreme size measurements skew the rate analysis and typically represent instrument noise and culture debris.

Large and instantaneous changes in the size distribution were interpreted as a partial occlusion of the instrument aperture or some other instrument error. The

files identified as "debris" files contained a 25% bound pair that was greater than 1.025 times the corresponding bound pair in either of the neighboring files. These files were replaced with data interpolated from the two neighboring files and linearly spaced across the entire 150s measurement. Interpolated data were written as a new Multisizer file and used for subsequent analysis.

4.10 Tables

Table 1 Yeast strains used in this study

Strain	Relevant genotype
A4370	*MATa, cdc28-as1 (w303)*
A17132	*MATa, cdc28-4 (w303)*
A702	*(WT) MATa/MATalpha, ade2-1/ade2-1, leu2-3/leu2-3, ura3/ura3, trp1-1/trp1-1, his3-11/his3-11,15, can1-100/can1-100 (w303)*

Table 4-1: Yeast strains used in this study

Table 2 Goodness of fit for exponential and linear growth patterns

	10% Bounds		25% Bounds		33% Bounds		Mode
	Lower	Upper	Lower	Upper	Lower	Upper	
R^2 of Linear Fit	0.938	0.896	0.943	0.896	0.943	0.903	0.932
R^2 of Exponential Fit	**0.994**	**0.950**	**0.995**	**0.949**	**0.992**	**0.932**	**0.972**

Table 4-2: Linear ($y=ax+b$) and exponential ($y=Ae^{bx}$) functions were fit to the bound and mode data of Figure 5A. Analysis was limited to data between 0 and 240 min, after which the population loses synchrony and is bimodal. The goodness of fit is determined by R^2, or the coefficient of determination, which measures scatter surrounding a fitted function. Higher R^2 values indicate a better fit and all populations from Figure 5A are better fit by the exponential function.

4.11 Contributions

Bryan, Andrea designed and conceived experiments. Gulati, Amneet and Engler, Alex performed experiments and analyzed data. Manalis, Scott contributed materials, reagents and analysis tools.

5 Final considerations

5.1 Technical advancements

Besides the technical advancements that have been elucidated in this thesis, there are additional innovations that could make the SMR platform a more robust, high-precision system for measuring multi-parametric data for yeast and other cells.

5.1.1 Fluorescent cell cycle reporters

To mark the cell-cycle transitions with even higher resolution that the bright-field microscopy (discussed in Section 2.4), we can study yeast strains that carry fluorescent reporters whose concentrations can be monitored using fluorescence microscopy. Instances of such reporters include the degradation of the cyclin dependent kinase inhibitior Sic1 indicating S-phase entry, degradation of Securin indicating entry into anaphase, and degradation of Clb cyclins indicating exit from mitosis.

5.1.2 Ultrasonic separation of cells

Another improvement that could be integrated into the SMR system is affixing a piezoelectric crystal to the underside of the chip that emits ultrasonic frequencies (~25kHz), analogous to sonication performed on the cell-culture to disperse cell aggregates prior to sample loading. This could aid in separating the mother and daughter cells while held in dynamic trap in the microfluidic chip, enabling multigenerational growth curves to be measured. In the same vein, following a cell division event one of the two cells is retained in dynamic trap as a result of a random choice by the trapping algorithm. However, we could in the future implement an automated routine that selectively captures only the mother cells (i.e. cells that are bigger in size than daughters) based on mass. This would enable us to study the effects aging and bud scars have on the growth rate and doubling time of the mother cells, which has been a topic of tremendous interest to me, and the scientific community at large.

5.1.3 Higher throughput measurement

The current SMR performs reliably with high-precision, however one of the major limitations of the system is its limited throughput as it can monitor only one cell at a time. This can be extremely time consuming if we want to study various nutrient conditions or mutational variants. There are ongoing efforts in our lab to increase throughput. One of the developments that hold promise is the SMR device with an extended buried channel with multiple trap-and-release structures that can hold and measure several cells at a time in serial. As such, one can measure not only the primary cell captured but also its progeny for several generations. Another effort in lab is to fabricate a chip with nearly 100 SMR devices that will be operated in parallel.

5.2 Biological studies

We have discovered in our studies that the processes of cell growth and cell division are correlated. However, the mechanism(s) underlying this correlation of nascent growth rate and nascent size are not understood. There are several studies that indicate that nutrient availability also alters growth rate. This growth rate in turn controls the set point of the critical cell size threshold by some unknown mechanism [24]. That is, in poorer nutrient sources, and hence at slower growth rates, yeast pass the critical size threshold at a smaller size. Previously, only indirect evidence has alluded to this nutrient-driven size-regulation mechanism on a population-level study. However, with the mass resolution of the SMR, and the time resolution of dynamic trapping, we should be able to directly observe the existence or lack thereof when and how coordination of growth and division is implemented at a single-cell level.

To study the implementation of this mechanism, one could measure the growth curves of various yeast cells and their descendants. If the size threshold were executed at Start, then we would expect to observe a convergence of the various growth curves of both mothers and daughters at a specific mass at the time of budding as will be monitored by integrated optical imaging.

5.2.1 Nutrient modulation of growth and critical cell size

It has been observed that in rich media cells take a much shorter time to pass Start and longer in poor media a much longer time. The 'Cln3 abundance' model rationalizes this observation by the claim that the synthesis of Cln3 must take a lot longer in dearth of nutrients and low ribosomal capacity. To test this hypothesis, in this experiment one can measure the inter-divisionary period, length of the G1-phase and critical size of cells growing wild-type yeast in a poorer carbon source, such as raffinose, and comparing it with the parameters obtained for cells cultured in glucose supplemented media, a rich carbon source.

5.2.2 Examine the dependence of growth rate on Cln3 expression

Similarly, the key to testing the 'Cln3 abundance' model would be to study the direct effects of Cln3 mutants on the growth of the cells. *Cln3*Δ mutant yeast can be studied using the SMR-based dynamic trapping. It is expected that if Cln3 is a major player in the G1-S transition, then the cells will have an extended G1 to accumulate the required Cln3 concentration to push forward into the S phase, and on the other hand, WHI-1 mutants that encode stabilized forms of Cln3 are found to have a shortened G1. These mutants will be obtained from the Amon laboratory.

5.2.3 Cell growth as a function of biosynthetic capacity

Biosynthetic capacity obviously drives an increase in cell size, and is in a way an integrator of past cell growth. This parameter can be interpreted as a rate of protein synthesis. It is possible that the rate of protein synthesis maybe a proxy for the upstream events, including nutrient status and growth factor signaling, thereby integrating many disparate signals into the size threshold. Protein synthesis rate is thought to be relayed to the cell cycle by unstable 'translational sizers', whose abundance reports translation rates and whose activity is rate-limiting for cell-cycle transitions [24, 33].

One experiment that could help separate the effect nutrient quality has on both the translational rate, and hence critical size threshold is by growing cells in sub-lethal concentrations of cycloheximide. Cycloheximide is a known inhibitor of

translational elongation. It would be interesting to note if the effects of cycloheximide on cells grown in a rich carbon source, would cause either a lengthening of the G1-phase, or decrease the critical size threshold for entering Start, or conceivably both. This would help us allude to the possibility of separate pathways for nutrient modulation and translational control of cell-cycle progress and critical size.

Ribosome biogenesis is a chief occupation of growing cells, accounting for about 60% of the total transcription in yeast cells [82, 83]. This rate of ribosome synthesis is dictated by the rate of transcription of the RNA and protein subunits of the ribosome. Therefore, another interesting study would involve cells that have a mutation that has impairs RNA Pol I activity.

RNA Pol I is responsible for the transcription of rRNA that constitutes the ribosomal complex. Of the groups of subunits of RNA Pol I, A14 is essential for the viability of the cell and the second group consisting of A49/A34.5/A12.2 contributes to the stability of the structure [84]. The depletion of one of these subunits will make the RNA Pol I less processive, but still a functional enzyme [85]. Thus, a yeast strain with a mutant *A49* gene will be studied to examine the dependence of the G1-S cell cycle transition on ribosomal concentration. If the hypothesis suggested by this model is correct, we would expect to see a longer delay to the S phase in this mutant strain, as compared to wild-type yeast growth.

5.2.4 Sfp1 and Sch9 – downstream effectors of TOR

Additionally, remarkable advances in genetic screening have identified Sfp1 (a zinc-finger transcription factor) and Sch9 (an Akt-like kinase) as effectors of nutrient modulation downstream of TOR. Significantly, Sfp1 and Sch9 have been found to activate the transcription of ribosomal protein and ribosome biogenesis genes in response to nutrient signals.

An interesting study could involve examining the effect the deletion of Sfp1 or Sch9 has on the size regulation. If one or both of these genes are involved upstream of the pathway that is responsible for nutritional modulation of critical

size, then cell size should lose dependence on nutrient dependence conditions in the sfp1Δ and/or sch9Δ deletion mutants. An SMR trapping measurement of cell buoyant mass in real-time could easily provide such data.

Additionally, one would expect that the effects seen in the experiment above would be similar to cells treated with known inhibitors of TOR complex, such as rapamycin and caffeine. Although, if different results are obtained, one has reason to suspect other parallel pathways such as that Ras/PKA may be responsible for nutritional regulation of size.

These and possibly more avenues can be explored with the SMR system that will give us more clues into the regulatory pathways that control feedback between cell growth, size homeostasis and cell division.

References

1. Jorgensen, P., and Tyers, M. (2004). How cells coordinate growth and division. Current biology : CB *14*, R1014-1027.

2. Conlon, I., and Raff, M. (1999). Size control in animal development. Cell *96*, 235-244.

3. Fantes, P.a. (1977). Control of cell size and cycle time in Schizosaccharomyces pombe. Journal of cell science *24*, 51-67.

4. Johnston, G.C., Pringle, J.R., and Hartwell, L.H. (1977). Coordination of Growth with Cell Division in the yeast Saccharomyces Cerevisiae. Experimental Cell Research *105*, 79-98.

5. Polymenis, M., and Schmidt, E.V. (1997). Coupling of cell division to cell growth by translational control of the G1 cyclin CLN3 in yeast. Genes & development *11*, 2522-2531.

6. Pfeuty, B., and Kaneko, K. (2007). Minimal requirements for robust cell size control in eukaryotic cells. Physical biology *4*, 194.

7. Hartwell, L.H., Culotti, J., Pringle, J.R., and Reid, B.J. (1973). Genetic Control of the Cell Division Cycle in Yeast. Proceedings of the National Academy of Sciences of the United States of America *66*, 352-359.

8. Rupeš, I. (2002). Checking cell size in yeast. TRENDS in Genetics *18*, 479-485.

9. Qu, Z., Weiss, J.N., and MacLellan, W.R. (2004). Coordination of cell growth and cell division: a mathematical modeling study. Journal of Cell Science *117*, 4199-4207.

10. Hartwell, L.H., and Unger, M.W. (1977). Unequal divison in Saccharomyces Cerevisiae and its implications for the control of cell divsion. The Journal of cell biology *75*, 422-435.

11. Mitchison, J.M. (1958). The growth of single cells. Experimental Cell Research *15*, 214-221.

12. Woldringh, C., Huls, P., and Vischer, N. (1993). Volume growth of daughter and parent cells during the cell cycle of Saccharomyces cerevisiae a/alpha as determined by image cytometry. Journal of bacteriology *175*, 3174-3181.

13. Cookson, N.a., Cookson, S.W., Tsimring, L.S., and Hasty, J. (2010). Cell cycle-dependent variations in protein concentration. Nucleic acids research *38*, 2676-2681.

14. Goranov, A.I., Cook, M., Ricicova, M., Ben-Ari, G., Gonzalez, C., Hansen, C., Tyers, M., and Amon, A. (2009). The rate of cell growth is governed by cell cycle stage. Genes & development *23*, 1408-1422.

15. Di Talia, S., Skotheim, J.M., Bean, J.M., Siggia, E.D., and Cross, F.R. (2007). The effects of molecular noise and size control on variability in the budding yeast cell cycle. Nature *448*, 947-951.

16. Davies, H., and Wilkins, M. (1952). Interference microscopy and mass determination. Nature *169*, 541.

17. Burg, T.P., Godin, M., Knudsen, S.M., Shen, W., Carlson, G., Foster, J.S., Babcock, K., and Manalis, S.R. (2007). Weighing of biomolecules, single cells and single nanoparticles in fluid. Nature *446*, 1066-1069.

18. Burg, T.P., and Manalis, S.R. (2003). Suspended microchannel resonators for biomolecular detection. Applied Physics Letters *83*, 2698-2700.

19. Lee, J., Bryan, A.K., and Manalis, S.R. (2011). High precision particle mass sensing using microchannel resonators in the second vibration mode. The Review of scientific instruments *82*, 023704.

20. Godin, M., Delgado, F.F., Son, S., Grover, W.H., Bryan, A.K., Tzur, A., Jorgensen, P., Payer, K., Grossman, A.D., Kirschner, M.W., et al. (2010). Using buoyant mass to measure the growth of single cells. Nature methods *7*, 387-390.

21. Utke, I., Friedli, V., Michler, J., Bret, T., Multone, X., and Hoffmann, P. (2006). Density determination of focused-electron-beam-induced deposits with simple cantilever-based method. Applied physics letters *88*, 031906-031906-031903.

22. Olcum, S., Cermak, N., Wasserman, S., Christine, K., Atsumi, H., Payer, K., Shen, W., Lee, J., Belcher, A., Bhatia, S., et al. (2014). Weighing nanoparticles in solution at the attogram scale. Proceedings of the National Academy of Sciences of the United States of America.

23. Dolznig, H., Grebien, F., Sauer, T., Beug, H., and Müllner, E.W. (2004). Evidence for a size-sensing mechanism in animal cells. Nature cell biology *6*, 899-905.

24. Jorgensen, P., Rupes, I., Sharom, J.R., Schneper, L., Broach, J.R., and Tyers, M. (2004). A dynamic transcriptional network communicates growth potential to ribosome synthesis and critical cell size. Genes & development *18*, 2491-2505.

25. Donnan, L., and John, P. (1983). Cell cycle control by timer and sizer in Chlamydomonas. Nature *304*, 630-633.

26. Lord, P.G., and Wheals, a.E. (1981). Variability in individual cell cycles of Saccharomyces Cerevisiae. Journal of cell science *50*, 361-376.

27. Wheals, A.E. (1982). Size Control Models of Saccharomyces cerevisiae Cell Proliferation. Molecular and cellular biology *2*, 361-368.

28. Son, S., Tzur, A., Weng, Y., Jorgensen, P., Kim, J., Kirschner, M.W., and Manalis, S.R. (2012). Direct observation of mammalian cell growth and size regulation. Nature methods *9*, 910-912.

29. Creanor, J., and Toyne, J. (1993). Preparation of synchronous cultures of the yeasts Saccharomyces cerevisiae and Schizosaccharomyces pombe. P. Fantes and R. Brooks, eds. (Oxford: IRL Press), pp. 25-44.

30. Polymenis, M., and Schmidt, E.V. (1999). Coordination of cell growth with cell division. Current opinion in genetics & development *9*, 76-80.

31. Brooks, R.F., and Shields, R. (1985). Cell growth, cell division and cell size homeostasis in Swiss 3T3 cells. Experimental cell research *156*, 1-6.

32. Conlon, I.J., Dunn, G.A., Mudge, A.W., and Raff, M.C. (2001). Extracellular control of cell size. Nature cell biology *3*, 918-921.

33. Elliott, S., and McLaughlin, C. (1978). Rate of macromolecular synthesis through the cell cycle of the yeast Saccharomyces cerevisiae. Proceedings of the National Academy of Sciences *75*, 4384-4388.

34. Throm, E., and Duntze, W. (1970). Mating-type-dependent inhibition of deoxyribonucleic acid synthesis in Saccharomyces cerevisiae. Journal of bacteriology *104*, 1388-1390.

35. Ferrezuelo, F., Colomina, N., Palmisano, A., Garí, E., Gallego, C., Csikász-Nagy, A., and Aldea, M. (2012). The critical size is set at a single-cell level by growth rate to attain homeostasis and adaptation. Nature communications *3*, 1012-1012.

36. Sun, J., Stowers, C.C., Boczko, E.M., and Li, D. (2010). Measurement of the volume growth rate of single budding yeast with the MOSFET-based microfluidic Coulter counter. Lab on a Chip *10*, 2986-2993.

37. Tzur, A., Kafri, R., LeBleu, V.S., Lahav, G., and Kirschner, M.W. (2009). Cell growth and size homeostasis in proliferating animal cells. Science *325*, 167-171.

38. Elliott, S.G. (1978). Rate of Macromolecular Synthesis through the Cell Cycle of the Yeast Saccharomyces cerevisiae. Proceedings of the National Academy of Sciences *75*, 4384-4388.

39. Di Talia, S., Skotheim, J.M., Bean, J.M., Siggia, E.D., and Cross, F.R. (2007). The effects of molecular noise and size control on variability in the budding yeast cell cycle. Nature Suppl. *448*, 947-951.

40. Turner, J.J., Ewald, J.C., and Skotheim, J.M. (2012). Cell size control in yeast. Current biology : CB *22*, R350-359.

41. Johnson, I. (2006). Practical considerations in the selection and application of fluorescent probes. 3rd Edition, J. Pawley, ed. (Springer), pp. 353-367.

42. Blagosklonny, M.V., and Pardee, A.B. (2002). The Restriction Point of the Cell Cycle. Cell Cycle *1*, 103-110.

43. Jagdish, M.N.C., L. A. (1977). Genetic Control of cell division in yeast cultured at different growth rates. Nature *269*, 145-147.

44. Nakashima, A., Maruki, Y., Imamura, Y., Kondo, C., Kawamata, T., Kawanishi, I., Takata, H., Matsuura, A., Lee, K.S., Kikkawa, U., et al. (2008). The Yeast Tor Signaling Pathway Is Involved in G2/M Transition via Polo-Kinase. Plos One *3*.

45. Bryan, A.K., Goranov, A., Amon, A., and Manalis, S.R. (2010). Measurement of mass, density, and volume during the cell cycle of yeast. Proceedings of the National Academy of Sciences of the United States of America *107*, 999-1004.

46. Tyers, M., Tokiwa, G., Nash, R., and Futcher, B. (1992). The Cln3-Cdc28 kinase complex of S. cerevisiae is regulated by proteolysis and phosphorylation. The EMBO journal *11*, 1773-1784.

47. Hoose, S.A., Rawlings, J.A., Kelly, M.M., Leitch, C.M., Ababneh, Q.O., Robles, J.P., Taylor, D., Hoover, E.M., Hailu, B., McEnery, K.A., et al. (2012). A systematic analysis of cell cycle regulators in yeast reveals that most factors act independently of cell size to control initiation of division. PLoS genetics *8*, e1002590-e1002590.

48. Moore, S.A. (1988). Kinetic Evidence for a Critical Rate of Protein Synthesis in the Saccharomyces cerevisiae yeast cell cycle. J Biol Chem *263*, 9674-9681.

49. Schneider, B.L., Zhang, J., Markwardt, J., Volpe, T., Honey, S., Futcher, B., and Tokiwa, G. (2004). Growth Rate and cell size modulate the synthesis of , and requirement for , G1 -phase cyclins at Start. Molecular and cellular biology *24*, 10802-10813.

50. Costanzo, M., Nishikawa, J.L., Tang, X., Millman, J.S., Schub, O., Breitkreuz, K., Dewar, D., Rupes, I., Andrews, B., and Tyers, M. (2004). CDK activity antagonizes Whi5, an inhibitor of G1/S transcription in yeast. Cell *117*, 899-913.

51. Cross, F.R., and Tinkelenberg, A.H. (1991). A potential positive feedback loop controlling CLN1 and CLN2 gene expression at the start of the yeast cell cycle. Cell *65*, 875-883.

52. Doncic, A., Falleur-Fettig, M., and Skotheim, J.M. (2011). Distinct interactions select and maintain a specific cell fate. Molecular cell *43*, 528-539.

53. Nasmyth, K., and Dirick, L. (1991). The role of SWI4 and SWI6 in the activity of G1 cyclins in yeast. Cell *66*, 995-1013.

54. Skotheim, J.M., Di Talia, S., Siggia, E.D., and Cross, F.R. (2008). Positive feedback of G1 cyclins ensures coherent cell cycle entry. Nature *454*, 291-296.

55. de Bruin, R.A.M., McDonald, W.H., Kalashnikova, T.I., Yates, J., and Wittenberg, C. (2004). Cln3 activates G1-specific transcription via phosphorylation of the SBF bound repressor Whi5. Cell *117*, 887-898.

56. Jorgensen, P., Nishikawa, J.L., Breitkreutz, B.-J., and Tyers, M. (2002). Systematic identification of pathways that couple cell growth and division in yeast. Science (New York, N.Y.) *297*, 395-400.

57. Fingerman, I., Nagaraj, V., Norris, D., and Vershon, A.K. (2003). Sfp1 plays a key role in yeast ribosome biogenesis. Eukaryotic cell *2*, 1061-1068.

58. Klein, C., and Struhl, K. (1994). Protein kinase A mediates growth-regulated expression of yeast ribosomal protein genes by modulating RAP1 transcriptional activity. Molecular and cellular biology *14*, 1920-1928.

59. Loewith, R., and Hall, M.N. (2011). Target of rapamycin (TOR) in nutrient signaling and growth control. Genetics *189*, 1177-1201.

60. Neuman-Silberberg, F.S., Bhattacharya, S., and Broach, J.R. (1995). Nutrient availability and the RAS/cyclic AMP pathway both induce expression of ribosomal protein genes in Saccharomyces cerevisiae but by different mechanisms. Molecular and cellular biology *15*, 3187-3196.

61. Fingar, D.C., Salama, S., Tsou, C., Harlow, E., and Blenis, J. (2002). Mammalian cell size is controlled by mTOR and its downstream targets S6K1 and 4EBP1/eIF4E. Genes & development *16*, 1472-1487.

62. Cohen, J., Cohen, P., West, S.G., and Aiken, L.S. (2003). Applied Multiple Regression/Correlation Analysis for the Behavioral Sciences 3rd Edition, (Lawrence Earlbaum Associates.).

63. Olkin, I., and Finn, J.D. (1995). Correlations redux. Psychological Bulletin *118*, 155.

64. Raftery, A.E. (1995). Bayesian model selection in social research. Sociological methodology *25*, 111-164.

65. Hua, S.Z., and Pennell, T. (2009). A microfluidic chip for real-time studies of the volume of single cells. Lab on a Chip *9*, 251-256.

66. Alexopoulos, L., Erickson, G., and Guilak, F. (2002). A method for quantifying cell size from differential interference contrast images: validation and application to osmotically stressed chondrocytes. Journal of microscopy *205*, 125-135.

67. Srinivasa, G., Fickus, M., Gonzalez-Rivero, M.N., Hsieh, S.Y., Guo, Y., Linstedt, A.D., and Kovacevic, J. (2008). Active mask segmentation for the cell-volume computation and Golgi-body segmentation of HeLa cell images. In Biomedical Imaging: From Nano to Macro, 2008. ISBI 2008. 5th IEEE International Symposium on. (IEEE), pp. 348-351.

68. Davey, H.M., and Kell, D.B. (1996). Flow cytometry and cell sorting of heterogeneous microbial populations: the importance of single-cell analyses. Microbiological reviews *60*, 641-696.

69. Givan, A.L. (2004). Flow cytometry: first principles, (John Wiley & Sons).

70. Tzur, A., Moore, J.K., Jorgensen, P., Shapiro, H.M., and Kirschner, M.W. (2011). Optimizing optical flow cytometry for cell volume-based sorting and analysis. Plos One *6*, e16053.

71. Coulter, W.H. (1956). High speed automatic blood cell counter and cell size analyzer. In Proc Natl Electron Conf, Volume 12. pp. 1034-1042.

72. Berge, L.I., Feder, J., and Jøssang, T. (1990). Single particle flow dynamics in small pores by the resistive pulse and the pressure reversal technique. Journal of colloid and interface science *138*, 480-488.

73. Boyd, C.M., and Johnson, G.W. (1995). Precision of size determination of resistive electronic particle counters. Journal of plankton research *17*, 41-58.

74. Hurley, J. (1970). Sizing particles with a Coulter counter. Biophysical journal *10*, 74-79.

75. Berge, L.I., Jossang, T., and Feder, J. (1990). Off-axis response for particles passing through long apertures in Coulter-type counters. Measurement Science and Technology *1*, 471.

76. Hartwell, L.H. (1973). Three additional genes required for deoxyribonucleic acid synthesis in Saccharomyces cerevisiae. Journal of bacteriology *115*, 966-974.

77. Bortner, C.D., and Cidlowski, J.A. (2004). The role of apoptotic volume decrease and ionic homeostasis in the activation and repression of apoptosis. Pflügers Archiv *448*, 313-318.

78. Maeno, E., Ishizaki, Y., Kanaseki, T., Hazama, A., and Okada, Y. (2000). Normotonic cell shrinkage because of disordered volume regulation is an early prerequisite to apoptosis. Proceedings of the National Academy of Sciences *97*, 9487-9492.

79. Baumgärtner, S., and Tolić-Nørrelykke, I.M. (2009). Growth pattern of single fission yeast cells is bilinear and depends on temperature and DNA synthesis. Biophysical journal *96*, 4336-4347.

80. Bishop, A.C., Ubersax, J.A., Petsch, D.T., Matheos, D.P., Gray, N.S., Blethrow, J., Shimizu, E., Tsien, J.Z., Schultz, P.G., and Rose, M.D. (2000). A chemical switch for inhibitor-sensitive alleles of any protein kinase. Nature *407*, 395-401.

81. Amon, A. (2002). Synchronization procedures. Methods in enzymology *351*, 457-467.

82. Moss, T., and Stefanovsky, V.Y. (2002). At the center of eukaryotic life. Cell *109*, 545-548.

83. Woolford Jr, J.L. (1991). The structure and biogenesis of yeast ribosomes. Adv. Genet *29*, 63-118.

84. Bischler, N., Brino, L., Carles, C., Riva, M., Tschochner, H., Mallouh, V., and Schultz, P. (2002). Localization of the yeast RNA polymerase I-specific subunits. The EMBO journal *21*, 4136-4144.

85. Jones, H.S., Kawauchi, J., Braglia, P., Alen, C.M., Kent, N.A., and Proudfoot, N.J. (2007). RNA polymerase I in yeast transcribes dynamic nucleosomal rDNA. Nature structural & molecular biology *14*, 123-130.

6 Appendix

Raw data

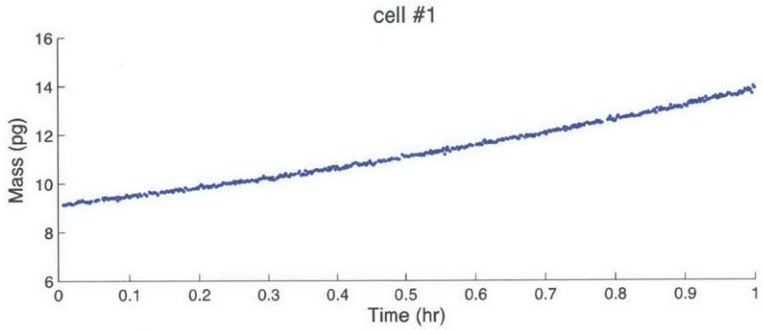

Residuals from 'simple exponential' model

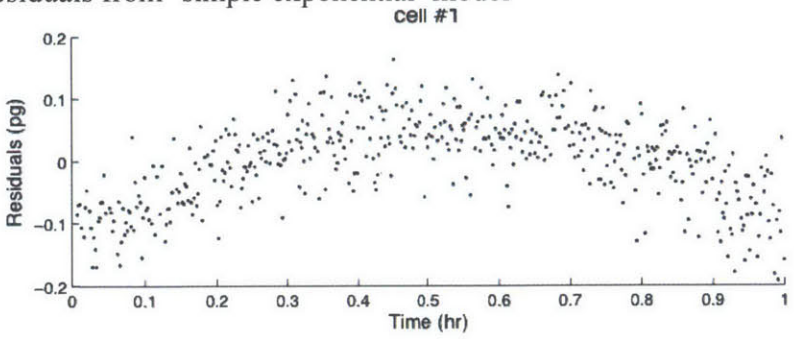

Residuals from 'bilinear' model

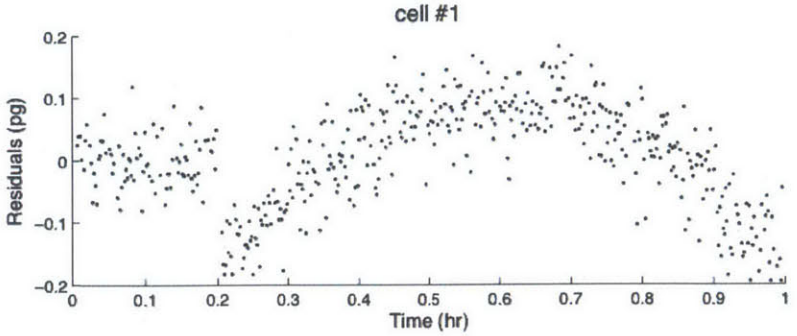

Residuals from 'exponential with an offset' model